Fabrication of Large Antenna Substrates of Monolithic Spatially Variable Ceramics and an Optimization Framework for Nano-Antennas

By

IŞIL BERKÜN

Submitted to the Graduate School of Engineering and Natural Sciences
in partial fulfillment of
the requirements for the degree of
Master of Science

SABANCI UNIVERSITY

SPRING 2009

Fabrication of Large Antenna Substrates of Monolithic Spatially Variable Ceramics and an Optimization Framework for Nano-Antennas

APPROVED BY:

Assist. Prof. Dr. GÜLLÜ KIZILTAŞ   ....
    (Thesis Advisor)

Assist. Prof. Dr. KÜRŞAT ŞENDUR   ....

Assist. Prof. Dr. MELİH PAPİLA   ....

Assoc. Prof. Dr. MEHMET ALİ GÜLGÜN   ....

Assist. Prof. Dr. ALİ KOŞAR   ....

DATE OF APPROVAL: ....

iii

Fabrication of Large Antenna Substrates of Monolithic Spatially Variable Ceramics and an Optimization Framework for Nano-Antennas

IŞIL BERKÜN

ME, M.Sc. Thesis, 2009

Thesis Supervisor: Assistant Prof. Dr. Güllü Kızıltaş

ABSTRACT

The aim of this thesis is driven by two main challenges in the antenna and propagation community: The possibility to manufacture exact replicas of spatially variable dielectric substrates for low frequency Radiofrequency (RF) applications and to achieve performance enhancements via formal optimization techniques for high frequency applications such as nano-antennas. In the RF and optics community, metamaterials have gained significant interest due to their extraordinary properties which are not accessible in nature. Textured composites with novel properties allow for the realization of state-of-the-art devices which are functionalized through spatially variable properties of dielectrics, magnetics and polymers. The possibility of spatially controlling permittivity and permeability at the preferred frequency and the capability of realizing multi-material volumetric variations is an ancient vision in the RF community. One such technique has been proposed and adopted to produce spatially variable ceramic substrates of small size (2" square) and assembled to construct a UHF SATCOM antenna substrate. In the first part of the thesis, the objective is to use earlier proposed Dry Powder Deposition (DPD) technique for producing large monolithic substrates with spatial variation of ceramic constituents that will allow for impressive performance enhancements as dictated by design results. Commercially available LTCC powders namely Calcium Magnesium Titanates (MCT) of dielectric permittivities 15, 20, 70 and loss tangent <

0.0015 are used as the ceramic constituents. Thermogravimetric analysis of each constituent powder is used to analyze efficient removal of 1-3 % binder content of spray dried MCT powders and achieve complete sintering of their textured composites. Also, a detailed analysis of the process parameters such as compaction pressure and cosintering temperature within the DPD method is carried out. As a result, smooth and large substrates with sizes up to 82mm x 82mm of monolithic dielectric textured composites were obtained by cosintering at optimal conditions. Cracks and unwanted defects such as porosities in textured composites were eliminated. Density measurements and SEM stressed that final substrates obtained were over %98 dense ceramic constituents. Microstructure characterizations of pellets made of sintered constituent material were carried out by SEM and dielectric permittivity measurements were performed.

In the second part of the thesis, the objective is to develop a basic framework to optimize a nano antenna's intensity enhancement and absorbed power according to variables such as length, thickness, width and wavelength using gradient and heuristic based methods (sequential quadratic programming and genetic algorithms). This framework will allow for more effective assessment of high-frequency antenna applications subject to multiple competing performance criteria and complex design variables in the future including the effect of material substrates, hence enable novel designs with superior performance for emerging plasmonic applications as was the case for the SATCOM antenna design in the first part of the thesis.

ÖZET

Bu tez temel olarak anten ve yayılım konuları ile ilgili iki temel mesele üzerine yürütülmüştür: Düşük frekanstaki radyo frekansı (RF) uygulamaları için uzaysal değişkenliğe sahip dielektrik tabakaların birebir kopyasını üretmek ve nano anten gibi yüksek frekans uygulamaları için formal optimizasyon teknikleri ile performans kazancı elde etmek. RF ve optik uygulamarında, doğada bulunmayan sıradışı özelliklere sahip metamalzemeler, önemli bir ilgi kazanmışlardır. Dielektrik, manyetik ve polimer birleşenlerin uzayda yerleşimleri ile meydana gelen heterojen malzeme yapıları doğada bulunmayan sıradışı özelliklere sahip modern cihazların elde edilmesine imkan verirler. İstenilen frekansta malzemenin uzaysal yerleşimi ile elektriksel geçirgenlik ve geçirimlilik gibi özelliklerin kontrolünü, çoklu-malzemelerin hacimsel varyasyonları ile elde etme isteği RF dünyasında uzun süredir varolan bir vizyondur. Bu vizyon ışığında küçük boyutlu (2") uzaysal değişkenliğe sahip seramik tabanlar üretime de adapte edilmiş ve UHF frekanslarında çalışan uydu anten tabanları tasarlanmıştır. Tezin ilk bölümündeki amaç, önceden önerilmiş olan kuru toz dökümü (DPD) tekniğini kullanarak, tasarım sonuçları ile de dikte edildiği gibi, etkili performans kazanımına imkan veren seramik bileşenlerin uzaysal varyasyonu ile büyük yekpare tabanlar üretmektir. Ticari olarak kullanılabilir olan LTCC tozları, dielektrik sabitleri 15,20,70 ve kayıp tanjantı < 0.0015 olan ve isim olarak Kalsiyum Magnezyum Titanat (MCT) diye bilinen seramik bileşenler kullanılmıştır. Sprey ile kurutulmuş MCT tozlarının 1-3% oranında bağlayıcı bileşeninin etkili uçuşunu ve dokunmuş kompozitlerin tam sinterlenmesininin elde edilişini analiz etmek için bileşendeki her tozun termogravimetrik analizi yapılmıştır. Ayrıca, sıkıştırma basıncı ve kosinterleme sıckaklığı gibi işlem değişkenleri detaylı olarak DPD metodunda ele alınmıştır. Sonuç olarak, boyutları 82mm x 82mm'ye varan düzgün ve büyük yekpare dielektrik dokunmuş kompozit tabanlar, optimal şartlarda kosinterleme yapılarak elde edilmiştir. Dokunmuş kompozitlerdeki çatlaklar ve gözenek gibi istenmeyen kusurlar bertaraf edilmiştir. Yoğunluk ölçümleri ve SEM, sonuçta gözlenen tabanların 98% den fazla yoğun olduğunu vurgulamaktadır. Sinterlenmiş bileşen malzemelerden oluşan pelletlerin mikroyapı karakterizasyonu SEM ve dielektrik geçirgenlik ölçümleri ile yapılmıştır.

Tezin ikinci kısmında amaç; uzunluk, kalınlık, genişlik ve dalgaboyu gibi değişkenlere göre nano antenlerin elektrik alan yoğunluğunun ve absorbe edilen gücü türevsel ve buluşsal temelli metotlar kullanarak (sırasal kuadratik programlama ve genetik algoritma) optimize

eden temel bir tasarım yöntemi geliştirmektir. Bu yöntem, birbiriyle çelişen çoklu performans kriterlerine ve gelecekteki dielektrik malzeme özelliğini de içeren kompleks tasarım değişkenlerine bağlı olan yüksek frekanslı anten uygulamalarının daha etkin değerlendirilmesine imkan vermesi, ve böylece ortaya çıkan plazmonik uygulamalar için ilk bölümdeki uydu anten tasarımında olduğu gibi üstün performanslı orjinal tasarımlara olanak tanıması beklenmektedir.

To my family

ACKNOWLEDGEMENTS

First, and foremost, I am deeply indebted to my supervisor Assist. Prof. Dr. Gullu Kiziltas whose help, stimulating suggestions, endless patience and encouragement helped me in all the time of research and writing of this thesis. I am grateful to her deep academic and personal perspective. She is and always will be a role model in my life.

I would like to express my gratitude to all those who gave me the possibility to complete this thesis. Among all the members of the Faculty of Engineering and Natural Science, I would gratefully acknowledge Assist. Prof. Dr. Kursat Sendur, Assist. Prof. Dr. Melih Papila and Assoc. Prof. Dr. Mehmet Ali Gulgun. Also I would like to state my gratefulness to the staff of the Faculty of Engineering and Natural Science, specially Mehmet Güler and Süleyman Tutkun for their endless help in fabrication process and Barış Tümer for his strong technical support on our workstations.

My colleagues, especially Lab 1100 residents from the Department of Mechatronics supported me in my research work. I want to thank them for all their help, hospitality, support, interest and valuable hints.

Especially, I would like to give my special thanks with all my heart to my dear family whose patient and love enabled me to complete this work. I love them more than what they can even imagine.

TABLE OF CONTENTS

TABLE OF FIGURES

LIST OF TABLES

TABLE OF ABBREVIATIONS

DPD : Dry Powder Deposition

SQP : Sequential Quadratic Programming

GA: Genetic Algorithm

SEM: Scanning Electron Microscopy

TGA: Thermogravimetric Analysis

K: Dielectric Constant

SATCOM: Satellite Communication

UHF: Ultra High Frequency

E: Electric Field Intensity

AP: Absorbed Power

L: Length

λ: Wavelength

FGM: Functionally Graded Materials

1   INTRODUCTION

1.1   Overview and Objective

The aim of this thesis is driven by two main challenges in the antenna and propagation community: The possibility to manufacture exact replicas of spatially variable dielectric substrates for low frequency RF applications and to achieve performance enhancements via formal optimization techniques for high frequency applications such as nano-antennas. Devices of this nature, with desired properties, are challenging to be designed from scratch and may not be fabricated with conventional fabrication techniques. Regarding the manufacturability, solid-void dielectrics are usually fabricated to realize artificial dielectrics or so called "meta" dielectrics. In the first part of the thesis we show that the control of relative permittivity with more than two shades in space is possible for large monolithic substrates using $CaTiO_3$-$MgTiO_3$- Mg_2TiO_4 as host dielectrics for UHF (*Ultra high frequency)* antennas.

In literature three types of porous structures are fabricated using $CaTiO_3$-$MgTiO_3$- Mg_2TiO_4 dielectrics [1] . One of these methods includes residuary sintering pores due to incomplete densification and will be taken into consideration as the primary fabrication method in this thesis. Other methods usually rely on sacrificial porogen and microfabrication by co-extrusion techniques. Recent design studies showed that the unique arrangement of dielectrics for preferred characteristics such as small size and large bandwidth can be determined from scratch using topology optimization [2, 3]. Dielectric designs via spatially variable dielectrics for impedance matching, have, in these cases led to important size decrease and higher bandwidth for low frequency antennas. However, both the design and fabrication focus so far has been generally on two constituent compositions such as high contrast ceramics and ceramic-polymers.

Examples of performing a factor of 2 or more decrease in ultrawideband antennas have been newly tried and shown to operate down to nearly 290 MHz [2]. Most important challenges in achieving the promised functionality, relate to the design process and the realization of proposed three dimensional (3D) artificial composites. The former is addressed by the proposed topology design optimization method known as the density method as in literature [2]. As a consequence, exact configuration of spatially variable multi-dielectric and magneto-dielectric composites are created with desired material properties not existing in nature. They call for single monolithic structures varying in their local compositions in three dimensions (3D). Concerning the fabrication challenge, methods capable of realizing designs for ceramic oxide metamaterials via spatially variable dielectric substrates [4], periodic band-gap structures, and simple magnetodielectric composites were investigated. Nevertheless, processing multi-phase materials as monolithic entities is a very demanding mission. Some novel fabrication methods require to be devised capable of achieving control of local composition and microstructure in two or three dimensions with sub-millimeter spatial resolution of multiple ceramics. A variety of processing techniques for functionally graded materials have been described [5]. But most of these methods are inefficient and not appropriate to build up ideal monolithic pieces with distinguished microstructural properties.

Dry powder deposition (DPD) method has been introduced by Wing and Halloran as a method capable of producing monolithic bodies with functional gradients [6]. Enabling the control of 3D location of spray dried ceramic materials and forming vertical variations through uniaxial compaction, it demonstrated 2D and assembled 3D functionally gradient ceramics as spatially variable dielectrics. The method is appropriate with broad range of dielectric materials that have compatible firing behavior and chemical stability. When compared to the traditional ceramic processing with high percentage of binder removal such as in thermoplastic methods, the most important advantage relates to easy removal of the low amount of binder content. Textured composites were produced by DPD method and delivered varying dielectric constants as a result of their spatially variable material distributions [7]. Though, optimization of DPD process parameters to attain large monolithic composite structures possibly with magneto-dielectric constituents has not been performed before. These are desired for enhanced multi-functionality.

MCTs used in this thesis are the constituents since they have commercially available grades and compositions of $CaTiO_3 - MgTiO_3 - Mg_2TiO_3$ allowing for a wide range of base

materials with desired permittivity values as suggested by the volumetric mixture rule [8]. Microspherical glassy carbon, commercial SIGRADUR® K, is included into the base MCT-20 ceramic material to decrease the dielectric permittivity to k=15 to match the desired three shade (k=15,20,70) computer-aided design result. The possibility to change the dielectric permittivity of the constituent MCT material allows the DPD to be extended to multimaterial dielectric material designs [9].

   Multimaterial ceramic processing is very prone to microstructural defects specifically as the substrate size increases. Binder burnout process should be efficiently performed on constituent spray-dried powders to eliminate warping and cracking of the green body [4, 10]. Also, the effect of porosity is known to increase dielectric loss [11], an undesired effect directly deteriorating the electromagnetic performance such as bandwidth and gain, so that the compaction of the green body and cosintering should be effectively optimized. Shrinkage mismatches of the constituent powders cause interface debinding due to incompatibility in cofiring behavior [12] although they show high dependence upon process parameters. Both dielectric and magnetic (Ni based ferrite) constituents' electromagnetic material properties such as dielectric permittivity and permeability show primary dependence on the processing parameters such as sintering temperature resulting in microstructural changes, density variations and defect formations [13-15]. Consequently, microstructural effects play a critical role and are investigated in this thesis in order to optimize process parameters and hence to improve the performance and the miniaturization of electromagnetic devices. This in turn, should increase the effectiveness of DPD method to produce technologically desired magneto-dielectric materials for various Radio Frequency and millimeter and microwave range devices.

   In this thesis, we present a detailed analysis of the process parameters of the DPD method. Repeatable filling, compaction and ejection of the texture were achieved and cold pressing and sintering conditions were optimized to produce smooth monolithic dielectric 3D composites. Optimization of DPD process parameters to get rid of porosity, cracks and thermal mismatch improved the microstructural control and enhanced the performance and applicability of this technique in the production of novel substrates for electromagnetic devices with enhanced performance.

With calcium magnesium titanates (MCT), the combination of the effective medium dielectrics with compositional gradients is being improved. MCT's are embedded into a SATCOM (MHz) antenna using the previously introduced smart dry powder deposition method.

In addition to the DPD fabrication challenges addressed for low frequency antenna applications, hence large monolithic substrates in this thesis, in the second part, the interaction of light with plasmonic nano-antennas is investigated via formal optimization techniques. It is noted that the design for the SATCOM antenna in the first part was developed earlier, hence the focus was on the fabrication part. To address the challenges of designing complex devices with possibly spatially varying substrates an application was selected from nano-optics. Nano-optical applications, such as scanning near-field optical microscopy [16] and data storage, require intense optical spots beyond the diffraction limit. Nano-antennas can get very small optical spots, but their capability to obtain optical spots beyond the diffraction limit is not adequate for practical applications [17]. In addition to a very small optical spot, a nanoantenna should provide high transmission efficiency for practical applications. The transmission efficiency of a nano-antenna determines the data transfer rate of storage devices and scan times of near-field optical microscopes. Therefore, the efficiency of nano-antennas should be optimized for potential utilization in practical applications. Optimization of nano-antennas is crucial for understanding their potential and limitations for emerging plasmonic applications [18].

The interaction of antennas with electromagnetic waves has been throughly investigated at microwave frequencies. Scaling and optimization rules do not apply at optical frequencies [19]. At visible and infrared frequencies the underlying physics of the interaction of light with metallic nano-antennas is complicated due to the behavior of metals as strongly coupled plasmas [20, 21]. Experimental studies have shown light localization using both dipole [22] and bow-tie [23] nanoantennas. A brute-force optimization study of these structures is not practical due to large number of parameters. There is a need for a systematic optimization of these structures not present in literature. . However, the effect of using spatially varying substrates is not known in literature. Furthermore, an optimization framework to address a more fundamental effect of size and shape on competing metrics such as electric field intensity and heat adsorbtion does not exist. With the goal addressing the more complex

material design problem via formal optimization techniques, an initial design framework is built in this thesis focusing the more fundamental problem of size optimization.

In this research, we build up a modeling-based automated design optimization framework to optimize nano-antennas. The modeling and simulation of these structures is done using 3-D finite element method based full-wave solutions of Maxwell's equations, Ansoft HFSS, which is integrated with heuristic optimization tools such as GA (Genetic Algorithms) and gradient based optimization tools such as SQP (Sequential Quadratic Programming). The modularity of the framework should allow in the future for an easy integration with a multiobjective optimization method called NBI and hence allow for locating non linear Pareto optimal points for a general nonlinear multicriteria optimization problem [24] for nano-antennas. So the objectives can be summarized as follows:

1) To produce large monolithic 3D structures of desired dimensions and dielectric and magneto-dielectric spatially variable constituents through the investigation of DPD process parameters. These parameters include mainly compaction pressure and the co-sintering scheme. Resulting 3D structures, if processed at the optimal conditions should allow for large monolithic substrates with more than two shades thermally compatible constituents and hence for dramatic performance enhancements.

2) To build up a modeling based automated design optimization framework to optimize size of nano-antennas.

1.2 Theoretical Background

1.2.1 UHF Antennas

Antennas are characterized by a number of parameters that explain their operation and performance. These parameters include: frequency/wavelength, polarization, gain, return loss (RL), and bandwidth (BW). Frequency and wavelength requirements depend on the application. Antenna size scales directly with the operational wavelength. Commercial UHF antennas that operate from 110-700 MHz can have dimensions approaching 1.34 m [25] (Fig 1).

5

Fig 1 Commercial UHF antenna (110-700 MHz) with a maximum dimension of 1.34 m

Satellite communication (SATCOM) antennas that operate in the 224-320 MHz range (free space λ= ~1.0 m) are typically 0.35 m in size (~λ/3) (Fig 2).
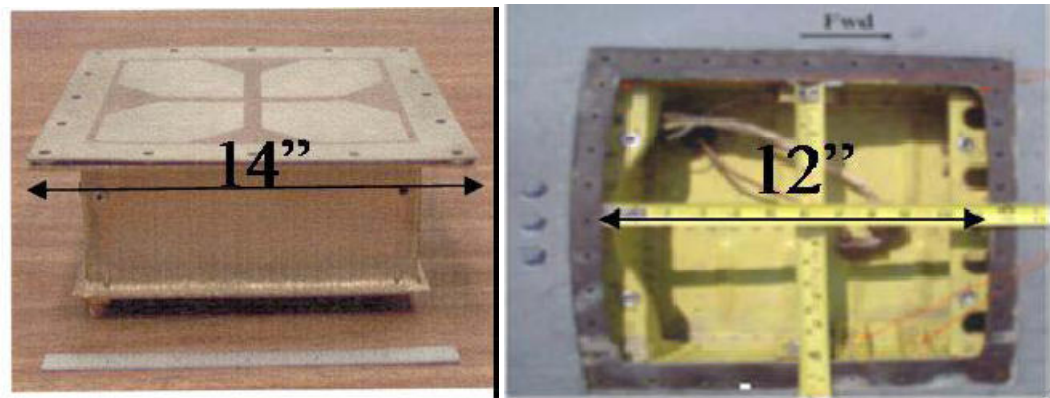
Fig 2 (Left) Typical SATCOM antenna (240-320 MHz). Size is ~0.35m (Right) SATCOM cavity for an F-14 (~ 0.30m)

The orientation of the electric field provides the polarization of an antenna. The two most common polarizations are linear and circular. Linear polarization describes an electric field that oscillates in a single direction normal to the direction of propagation. Circular polarization involves an electric field vector that rotates in a circular path normal to the direction of propagation [26].

A transmitting antenna's performance is quantified in terms of its radiation directivity and efficiency. The directivity of an antenna is expressed as gain and represents the amount of energy radiated in a given direction compared to an isotropic radiator. It is expressed in dB. The return loss (RL) of an antenna represents the ratio of power reflected by the antenna to

6

the power input [27]. It is expressed in dB and typically, a value of -10 dB is considered acceptable. A perfectly matched antenna would have the RL= -∞ and no power is reflected back towards the transmitter. The bandwidth of an antenna is defined as the range of usable frequency higher and lower than the center frequency that have RL<-10 dB.

In this thesis the fabrication challenges are addressed for a UHF SATCOM antenna. The design is required to address the existing need of replacing bulky and often inefficient antennas currently used for satellite communications at UHF frequencies (224-317MHz) with a particular emphasis on the higher 290-317 MHz band and a target antenna size no larger than 6 inches as specifies by design specifications [28]. The design challenge is to miniaturize the antenna and still retain its bandwidth with a satisfactory gain performance The resulting advanced design relies on the full exploration of dielectric loading in the form of substrates or superstrates. Moreover, monolithic materials are desirable to maintain device integrity, so it is preferable to achieve permittivity variations in a monolithic co-fired ceramic substrate.

1.3   Applied Dielectrics

Ceramics wit relatively high dielectric constants (higher than $\varepsilon_r \sim 10$), give a chance to the minimization of microwave devices (antennas, resonators, filters, capacitors etc). Besides the dielectric constant, loss and temperature coefficient are among priorities in overcoming the miniaturization challenge. When the dielectric constant (ε_r) increases, the performance of the devices have a tendency of deteriorating due to increased loss and narrowed bandwidths, hence there exists a tradeoff and therefore instead of naïve usage of high dielectric constant, a spatial variation of different low and high shades of dielectric material, i.e. grading or texturization is desired. Practical dielectric constants (ε_r) with satisfactory low loss generally range from 10-90. Loss inherently increases with ε_r and also depends on the operational frequency. Hence, selection of the material constituents even in the case of spatially variable texturized substrate is critical when driving for high dielectric components and must be considered together with other balancing dielectric properties for the desired application.

1.4   Antenna Miniaturization

The major benefit of using high ε_r materials is to slow the wave which is at the essence of miniaturizing electromagnetic devices. Miniaturization in turn is of plays a primal role in aerospace applications where satellite communication (SATCOM) antennas may operate at 200-600 MHz. The free space wavelength is on the order of 1 meter at these frequencies. Hence, the actual size of these antennas is fairly large. Smaller designs also include weight savings and portability. Dielectrics are being used in antenna fabrication for many years but the use of high ε_r materials while reducing antenna performance, at the same time decreases bandwidth and gain [29], hence have been considered with other design modification within the antenna in addition to its material focus, material texturization, i.e. the variation of material properties in 3-dimensional space. Hence, miniaturization is accomplished while managing performance [30].

1.5   Nano Optics

Existing and emerging nano-optics releated technologies include near-field scanning optical microscopy (NSOM), photoassisted scanning tunnelling microscopy, nanolithography, high resolution optical microscopy, and high-density optical data storage.

Propagating light may be focused to a spot with a minimum diameter of roughly half the wavelength of the light because of the diffraction limit (also known as the Rayleigh Criterion). Thus, even with diffraction-limited confocal microscopy, the maximum accessible resolution is on the range of a couple of hundred nanometers. The scientific and industrial communities are becoming more curious in the characterization of materials and phenomena on the scale of a few nanometers, so alternative techniques must be used. Scanning Probe Microscopy (SPM) makes use of a "probe", (usually either a tiny aperture or super-sharp tip), which either locally excites a sample or transmits local information from a sample to be collected and analyzed. The ability to fabricate devices in nanoscale that has been established recently fastened the improvements for this field of study [31].
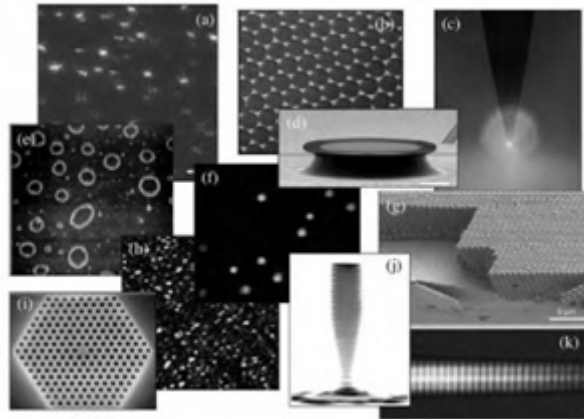
Fig 3 Examples of man-made nanophotonic structures

Some of the examples of man-made nanophotonic antennas [17] can be seen in Fig 3. Nano-antennas can attain tiny optical spots, but their ability to obtain optical spots beyond the diffraction limit is not adequate for practical applications [32]. In addition to a very small optical spot, a nanoantenna should supply high transmission efficiency for practical applications. The transmission efficiency of a nano-antenna terminates the data transfer rate of storage devices and scan times of near-field optical microscopes. For that reason, the efficiency of nano-antennas should be optimized for potential utilization in practical applications. Optimization of nano-antennas is critical for assessing their potential and limitations for emerging plasmonic applications.
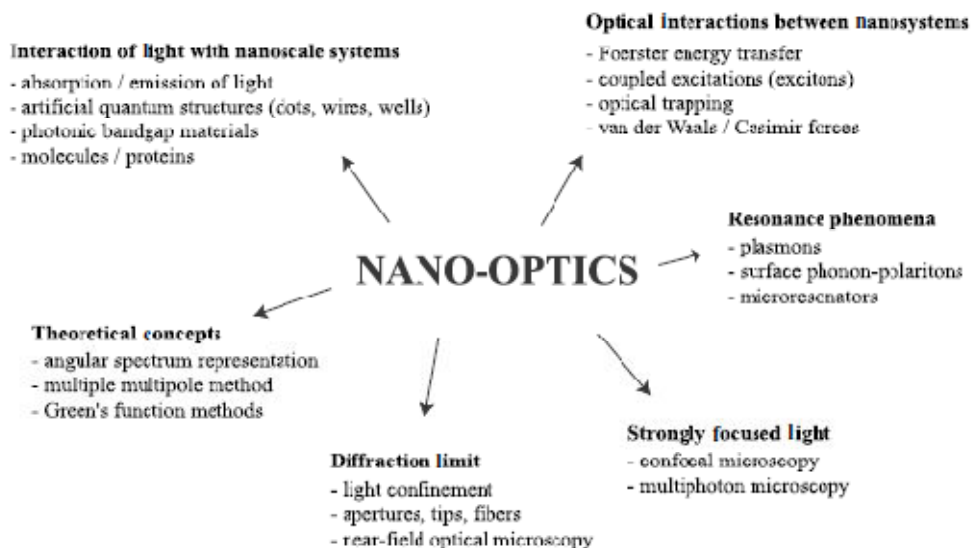
Fig 4 Constituents of the field of nano-optics

There are various constituents of the field of nano-optics as seen in Fig 4 [17]. An antenna among others contains metallic parts which constitutes the actual radiating component. For example, the dipole antenna shown in Fig 5 is composed of two metallic rods separated by a distance, G. Similarly, a frequently used bow-tie antenna shown in Fig 6 is composed of two triangular metallic pieces, which are also separated by a distance, G. In this thesis we will investigate the intensity enhancement ($\frac{|E^T(0,0,0)|^2}{|E^i(0,0,0)|^2}$) where E^T is the total field intensity and E^i is the incident field intensity and also the absorbed power (AP) of a dipole nano-antenna according to the variables such as length (L), thickness (T), width (W), distance (G) and wavelength (λ) but the framework's parametric encoding structure and its modularity should allow for the analysis and design of bow-tie antennas as well.
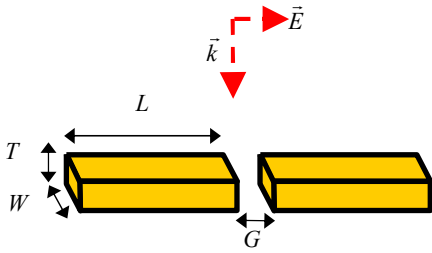
Fig 5 A schematic illustration of a dipole antenna   Fig 6 A schematic illustration of a bow-tie antenna
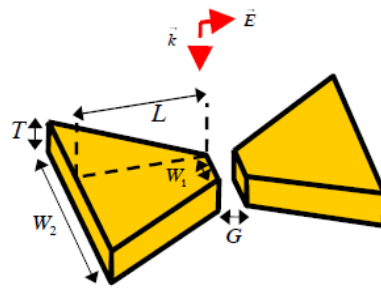
1.6   Design Optimization

Even though the innovation that new materials can bring is known, there are challenges and limitations when it comes to their design and practical insight. Optimization is the science of finding the best and it has found many applications by finding good solutions to real world problems. Nevertheless, several of these efforts presume that the objective function can be expressed algebraically and in explicit form. This means that when a new set of variables is introduced, the evaluation of the function is quick. In addition, it is often necessary to differentiate the function, which guides algorithms towards the local optimum. Though, most

of the time engineering designs are so complex that their performance can only be evaluated by running a computational model. Most of the time, this model is created by numerical methods for finding approximate solutions of partial differential equations (PDE) as well as integral equations such as a finite element model. As new design variables are introduced to the synthesis module which basically consists of an appropriate optimization algorithm, it is necessary to run the model at each iteration of the design cycle. Furthermore, if the optimizer is a local technique relying on gradients of the objective function, these are most of the time to be calculated using finite difference approximations. Therefore, the bottleneck of almost all real device design optimization efforts is the cost associated with running the computational model repetitive times. In this thesis we will integrate an FEM based commercial software, HFSS, with gradient and heuristic based design optimization tools such as Sequential Quadratic Programming (SQP) and Genetic Algoritms (GA) within a MATLAB computing environment to investigate the optimum conditions of intensity enhancement (E^2) and dissipated power (AP) for nano-antennas.

1.7   Contributions

The contributions of this thesis can be summarized as follows:

- Optimal processing conditions for MCT20, MCT70 (and Ni-based ferrite) were determined to obtain compatible shrinkage conditions where cracks, warpages and undesired porosities were mostly eliminated within a large monolithic substrate layer designed for a UHF SATCOM antenna design.

- It is also shown that dielectric permittivity and permeability can be tuned by mixing existing dielectric and magnetic shades of commercially available LTCC powders.

- The substrate layer of an earlier design UHF antenna was fabricated with the desired morphology.

- An automated design optimization framework using a script based framework relying on a full wave analysis simulator, HFSS, and optimization tools in MATLAB relying on SQP and GA was developed for the design of dipole nano-antennas.

11

2 FABRICATION OF SPATIALLY VARIABLE DIELECTRIC SUBSTRATES USING MCT CERAMIC POWDERS

2.1 Introduction

Engineered materials, such as new composites, electromagnetic bandgap and periodic structures have been of strong interest in recent years due to their extraordinary and unique electromagnetic behavior. These functionally graded materials also known as electromagnetic metamaterials have been demonstrated to promise new functionality, through otherwise physically unobtainable properties [1, 33, 34]. Their electromagnetic properties arise from a particular design, arranging conductors, dielectrics, and magnetic substances in space. Recent design studies showed that the unique arrangement of dielectrics for desired performances such as large bandwidth and small size can be determined from scratch using topology optimization [2, 3]. Dielectric designs via spatially variable dielectrics for impedance matching, have, in these cases led to significant size reduction and higher bandwidth for low frequency antennas. Nevertheless, the focus so far has been mostly on two constituent compositions such as high contrast ceramics and ceramic-polymer substrates.

Major challenges in achieving the promised functionality relate to the design process and the realization of proposed three dimensional (3D) artificial composite. The former is addressed via the proposed topology design optimization method known as the density method [2]. As a result, exact configuration of spatially variable multi-dielectric and possibly magneto-dielectric composites are created with desired off-the-shelf material properties not existing in nature. These designs present single monolithic structures varying in their local compositions in three dimensions (3D). Regarding the latter, fabrication methods capable of realizing designs for ceramic oxide metamaterials via spatially variable dielectric substrates [4], periodic band-gap structures, and simple magnetodielectric composites were investigated. However, processing multi-phase materials as monolithic entities is a very challenging task. Some new fabrication methods need to be devised capable of achieving control of local composition and microstructure in two or three dimensions with sub-millimeter spatial resolution of multiple ceramics. Various processing techniques for functionally graded

materials have been described [35]. But most of these methods are cumbersome and not suitable to build up perfect monolithic pieces with distinguished microstructural properties.

The goal of this study is to obtain perfectly sintered monolithic 3D structures of larger size up to 82 mm x 82 mm (as desired by the design) made of dielectric and magneto-dielectric spatially variable systems through the investigation of DPD process parameters such as compaction pressure and cosintering temperature. Resulting 3D structures should allow for performance enhancements. MCTs are used since they have commercially available grades and compositions of $CaTiO_3 - MgTiO_3 - Mg_2TiO_3$ allow for a wide range of base materials with desired permittivity values as suggested by the volumetric mixture rule [8]. Microspherical glassy carbon, commercial SIGRADUR® K, is incorporated into the base MCT-20 ceramic material to lower the dielectric permittivity to k=15 to match the desired three shade (k=15,20,70) computer-aided design result. In this study, an in-depth analysis of the process parameters of the DPD method is carried out. Repeatable filling, compaction and ejection of the texturized substrate is achieved. Also, cold pressing and sintering conditions are optimized to produce smooth monolithic large size dielectric 3D composite substrates. Optimization of DPD process parameters to get rid of porosity, cracks and thermal mismatch improves the microstructural control and enhances the performance and applicability of this method to be extended to multimaterial dielectric material designs [9]. These multi-material dielectric material designs are also known as FGM and will be discussed next.

2.2 Textured Dielectrics and Functionally Graded Materials (FGM)

Functionally graded materials (FGM) basically use engineered gradients in composition, structure, or properties [36]. Steels that have undergone surface treatments can be considered as a graded material. However, modern FGM's seek to establish gradients locally (as opposed to a whole surface) throughout the fabrication procedure. The objective is to incorporate the additional degrees of freedom into the actual design process to allow for optimization via "local composition control" or LCC [37]. Probable applications include thermal barrier coatings, tools, piezoelectric actuators, medicine, and electric devices. Functionally graded materials typically have been demonstrated with one dimensional gradients in a "layered" structure. Achieving two or fully three dimensional FGM's is partially limited by the lack of

designs and manufacturing difficulties, hence only a few examples exist in literature and are discussed next.

2.2.1 FGM Examples

Piezoelectric actuators are of attention in smart structures for controlling vibrations. On the other hand, their reliability can be limited due to stress concentrations at actuator interfaces with bonding layers. One approach to minimizing interfaces is to develop monolithic devices. Monolithic telescopic actuators demonstrated by Alexander, Brei, and Halloran has shown promise [38]. Also, functionally graded piezoelectrics have been developed to minimize the stress concentrations and create devices monolithically. PZT actuators with graded porosity have been demonstrated by Takagi and Taya that achieve low stress deflections [39]. Navarro and Alcock also created porosity gradients in PZT ceramic actuators [40]. Other approaches have utilized a functional compositional gradient within the PbNi1/3Nb2/3O3-PbZrO3-PbTiO3 (PNN-PZ-PT) system to create monolithic actuators [41-43]. Another area in which FGM's are of interest is in thermal barrier coatings (TBC) of turbines. Higher temperatures in combustion turbines yield higher efficiency. Ceramic barrier coatings are used to provide oxidation resistance and thermal insulation. However, mismatching thermo-elastic properties and temperature gradients between the metal substrate and TBC can lead to failures [44]. Gradients in porosity in the TBC are used to reduce thermal conductivity and reduce thermo-elastic gradients [45, 46]. In this thesis, the DPD process will be used to produce FGM materials for electromagnetic substrates used in antenna applications.

2.3 Miniaturization of a UHF Antenna via Spatially Variable Dielectric Texturization

2.3.1 Motivation

Antennas are devices that transmit and receive electromagnetic radiation. Their presence in modern technological devices is becoming gradually more extensive as the wireless boom continues. Antenna size scales with the size of the operational wavelength. The size of wireless devices is dependent on their antennas. The same is true for aircraft antennas. The uplink frequency for satellite communication in an F-14 aircraft is 270-320 MHz. At this

frequency range, the free space wavelength (λ) is ~ 1 meter. Most antennas are resonant devices, which operate efficiently over a relatively narrow frequency band. Typical resonant antenna sizes are based on λ/2 or λ/4 side length. For example, on an aircraft (used in defense applications), real estate on this length scale is substantial. Hence, there is a large motivation to reduce antenna size.

2.3.2   Antenna Design and Optimization

The design of the antenna begins with determining the material configuration and antenna geometry. A square spiral geometry was selected in the UHF antenna substrate to be fabricated due to its basic geometry and inherent broadband behavior given the antenna operational uplink frequency band of 290-320 MHz. The initial geometry is shown in Fig 7 and it consists of a 3 x 3 array configuration of spiral antennas. Each unit cell is 5.8 x 5.8 cm and 2.0 cm thick. The unit cell consists of 5 layers of **k**=36 and a bottom layer **k**=1 (layer 5). The actual spiral is located between layers 2 and 3. This initial configuration showed a narrowband resonance centered at 317 MHz (312-324 MHz) [11].
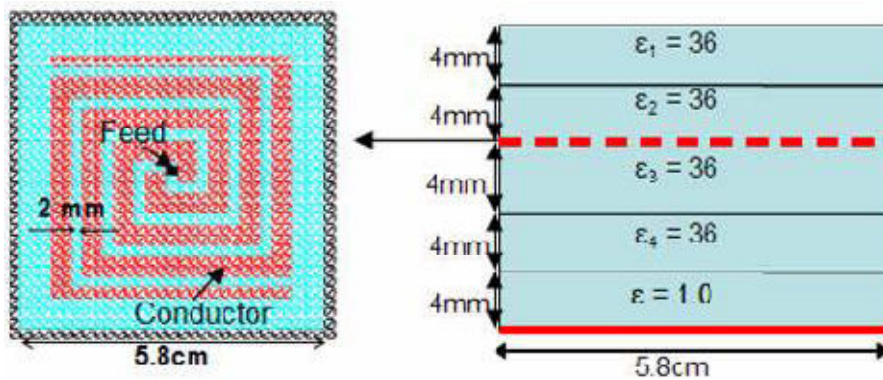
Fig 7 Initial design configuration of a single unit cell

The second step involves optimization of the return loss by changing the material distribution within layers 1-4. A topology optimization method called Solid Isotropic Material with Penalization (SIMP) is used [47]. SIMP assumes a relationship between a material's density (ρ) and a material property. In this case, the material property is the dielectric constant (**k**). The relationship between the relative density and **k** was demonstrated before. This is

advantageous because the discretization of the topology is limited only by the desired size of the finite element cells.

Optimization is performed by changing the property of each finite element cell's material property of each layer. The optimization process is subject to maximizing the return loss between the desired frequency bandwidth of 290-320 MHz. This process continues until the return loss maxima converges (19 iterations). Fig 7 shows the optimal layer-by-layer dielectric distribution. The expected return loss response for the "optimal case" shows a significant improvement in the bandwidth within 292-315 MHz.
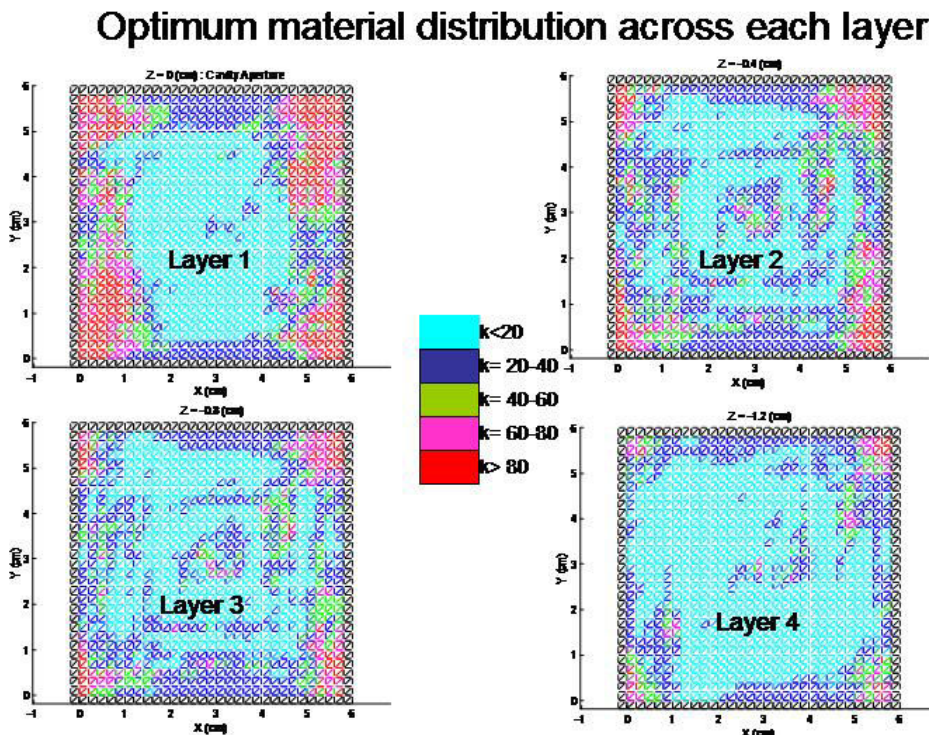
Fig 8 Optimized dielectric distribution of a unit cell * Designed by Gullu Kiziltas

It is clear from Fig 8 that the optimal material distribution [2] dictates a very challenging design in terms of manufacturing. It calls for 5 different values of **k** that are distributed between 4 layers, where each dielectric cell is 2 mm x 2mm (4mm tall) voxel (volumetric pixel). Thus, each layer is an array of 29 x 29 voxels (841 total) and each unit cell would contain 4 x 29 x 29 (3364 total) cells. To simplify the design, the optimal design was post processed by reducing the 5 shades of **k** down to 3 as seen in Fig 9. Other simplification included changing the 4th layer to a homogeneous one with **k**=15 and making layers 2 and 3 identical. This reduced the number of voxels to a much more manageable 2523 per unit cell.

16

The final three layer (simplified) distribution is shown in Fig 10 with the expected return loss response.
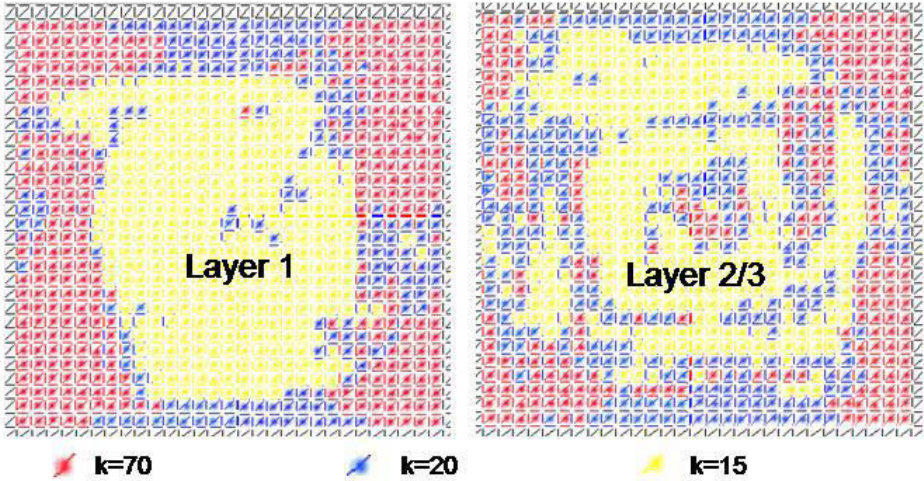
Fig 9 Simplified "optimal" material distribution
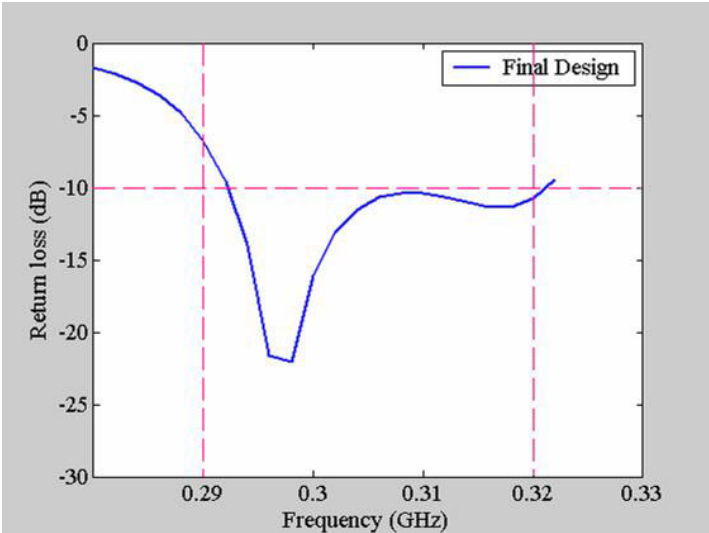
Fig 10 Simulated return loss for the simplified design

2.4   Materials, Fabrication and Performance

2.4.1   Material Selection

A set of calcium magnesium titanates were selected to satisfy the dielectric requirements for the textured substrate in Fig 9. This family of dielectrics possesses the chemical compatibility and similar thermo-elastic properties such that resulting compositions variations will co-fire. However, only the **k**=70 and **k**=20 materials are commercially available (Trans-Tech Inc., MCT 70 and MCT 20). Thus, the **k**=15 requirement will be satisfied via the effective medium route using a 25% porous MCT 20.

2.4.2   Dry Powder Deposition (DPD)

The deposition of dried powders in well-controlled patterns is not a new application. For example Sand Painting is an ancient ceremonial practice used by the Buddhist monks of Tibet and by Navajo Indians in the American southwest. The production of these artworks is a very important exercise in skill. There are some methods in literature involving powder flow and deposition via capillaries actuated using vibrations [48]. Coupling this process to computer controlled X-Y table has shown the ability of dry powder methods for small scale 2-D designs [49]. DPD method is capable of producing monolithic bodies with functional gradients such as large monolithic substrates with spatial variation of ceramic constituents that will allow for impressive performance enhancements. In this thesis the effect of DPD process parameters such as uniaxial pressure and sintering schemes on the shrinkage rate, dielectric performance, and microstructure are analyzed in detail. Based on the optimal process parameters, these are then used in the DPD process to produce monolithic large substrates of spatially variable MCT ceramic powders for the UHF antenna discussed in Section 2.3.2.

Spatially variable properties are desired for the next generation electromagnetic devices [2]. These devices (filters, antennas, etc) exploit all possible design degrees of freedom such as geometry, material and energy feeds to maximize their performance. Hence, non-intuitive design is usually achieved via optimization methods meeting design constraints and freedoms relying on computational methods rather than trial and error. Typically, the resulting complex optimal material distribution is fabricated with ceramic powders mixed with significant

18

amounts of polymer binder as required in standard ceramic processing which are then machined or formed using thermoplastic green machining methods [4]. However, these techniques are limited to single or two-phase constituents of small geometries due to binder removal problems at high polymer loadings. Long binder removal schedules become all-important and defects become casual for large thicknesses or substrate size. Dry powder methods such as DPD are favorable because their binder content is much smaller, which means larger geometries are feasible. Complex material variations are difficult to maintain using classic powder pressing due to the difficulty in controlling the location of the dry powder. In this study, we use a removable equipment, a fixture, to control the location of powder in a thick bed.

The purpose of this work is to present a method for producing large monolithic, spatially variable dielectrics in which regions of variations are discretized into square pixels. The process of Dry Powder Deposition can process multiple dielectrics with similar firing behavior and chemical stability. This new method controls the spatial location of loose powder prior to compaction, i.e. the location of loose powder prior to compaction is managed by the DPD method. The process is composed of 3 steps: powder deposition, fixture (removable equipment) extraction, and compaction. After all wells are filled, the fixture is extracted vertically. Finally, the piston is inserted and pressure is applied to compact the powder.

In Fig 11 the female part of the stainless steel die can be seen, the fixture is inserted in the die as shown in Fig 12.

Fig 11 Stainless steel die (female part)   Fig 12 Locating the SLA grid fixture into the die
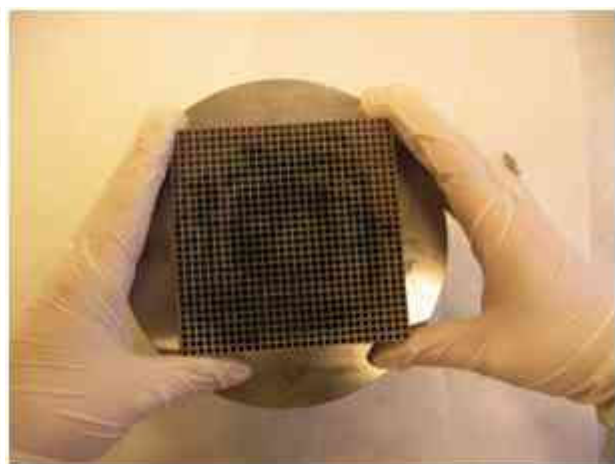
In Fig 13 the powder deposition process into the die is shown where a patterned transparency film machined with holes in desired material locations was placed on top of the grid fixture. Hence, during deposition, only desired grid holes are filled. After depositing each constituent, in this case three types of powders were deposited in to the die, the grid is pulled out vertically and the substrate is obtained in its loose powder form as shown in Fig 14.
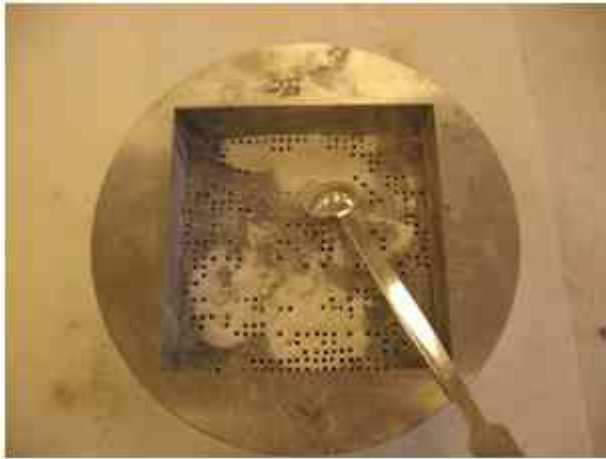
Fig 13 Powder deposition   Fig 14 Mold and powders after extracting the fixture
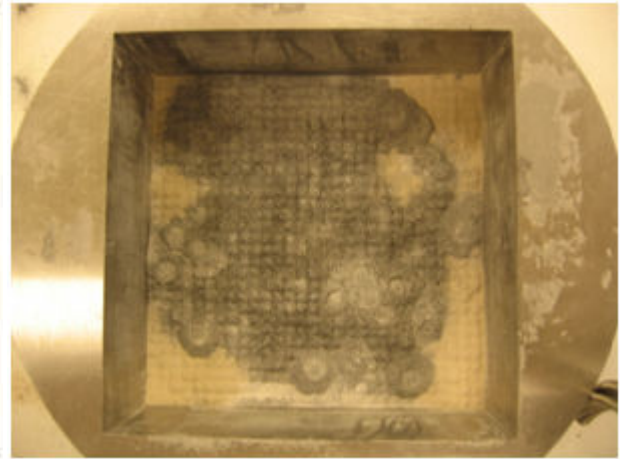
The male part of the mold is settled upon the resulting substrate which is then compressed under various pressures, such as the optimal pressure of 150 bar for about 2 minutes (Fig 15). At this stage, the substrate is just firm enough to be handled and transferred to a crucible after which sintering of the substrate in a high temperature furnace takes place and a dense substrate is obtained (Fig 16). This process is repeated for each layer with desired different material compositions. For each different layout, a different patterned film is produced and used.

Fig 15 Substrate after compaction

Fig 16 Substrate (layer 2) after sintering

The effect of the process parameters such as sintering temperature, sintering time and compression pressure to the substrate dimensions are analyzed before using these conditions for the manufacturing of the final substrate. Resulting substrates using the DPD process under various conditions are given in Fig 16 - Fig 24. The selected trial pressure and sintering temperatures were motivated by the extensive pellet analysis carried out using same material constituents as presented in Section 2.4.3.

The substrates obtained using 150 bar pressure and sintering temperatures of 1400 C and 1450C for 6h, respectively are shown in Fig 17 and Fig 18. No major difference was observed in terms of their dimensional accuracy and the formation of the lower left crack.

Fig 17 Substrate (layer 2) produced using compression pressure of :150Bar, Sintered at 1400C for 6h

Fig 18 Substrate (layer 2) produced using compression pressure of :150Bar, Sintered at 1450C for 6h

21

The substrates that were compressed under the same pressure of 150 bar and sintered at 1450C and 1400C for a shorter time of 4h, respectively are depicted in Fig 19 and Fig 20. It is observed that reduction of the sintering time less than 4h increases warpage and produces more cracks if the temperature is reduced down to 1400C.

Fig 19 Substrate (layer 2) produced using compression pressure of :150Bar, Sintered at 1450C for 4h

Fig 20 Substrate (layer2) produced using compression pressure of :150Bar, Sintered at 1400C for 4h

The substrates were then sintered at 1450C for 4h and produced using a lower pressure of 140 bar and 125 bar, respectively and the resulting layers are shown in Fig 21 and Fig 22. Despite no major change in crack formation when compared with higher pressures dimensional inaccuracies increased especially towards the center area of the substrate with reduced pressures of 125 bar.

Fig 21 Substrate (layer2) produced using compression pressure of :140Bar, Sintered at 1450C for 4h

Fig 22 Substrate (layer2) produced using compression pressure of :125Bar, Sintered at 1450C for 4h

To validate the effect of lower pressure, the layers were produced using a relatively low pressure of 90 and at the same time sintered at reduced temperatures of 1400 C for 4h and

similarly using a pressure of 100 bar pressure and sintering conditions of 1450C for 4h, respectively where resulting substrates are shown in Fig 23 and Fig 24. As expected, reduced compression pressure and sintering temperatures are lower, major cracks were observed. Overall, despite the occurrence of a single small crack near the lower left corner according to the dimensional accuracy of produced substrates, optimal processing conditions indicated a compression pressure of about 150 bar and a sintering temperature of around 1450C for at least 4 hours or 1400 C for at least 6 hours.

Fig 23 Substrate (layer2) produced using compression pressure of ≈ 90Bar, Sintered at 1400C for 4h
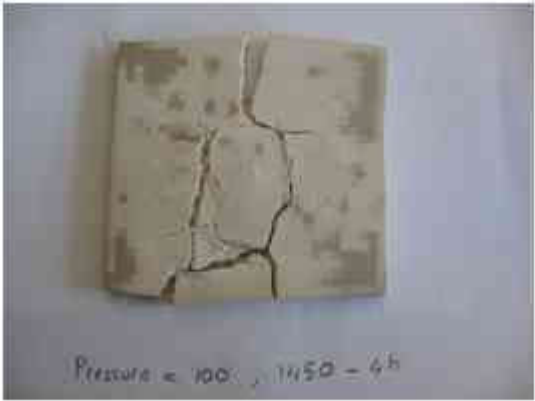
Fig 24 Substrate (layer2) produced using compression pressure of :100Bar, Sintered at 1450C for 4h

It is noted during the DPD trials that when Carbon is present used in the fabrication of the design to obtain the k15 dielectric material, crack formation potential is significantly high. This is attributed to the easy smearing and sticking characteristics of the conductive carbon to both the SLA fixture and the die. Hence, surface smearing arise during compression, removal of the fixture, and removal of the substrate from the die. This gives rise to material gradients at wall-to-wall contact areas and throughout the thickness of the substrate where smearing and sticking occurs. To validate this behavior, K15 material with the problematic carbon constituent is exchanged with the K20 material, and as expected resulting morphology of the materials and the dimensional accuracy is observed to improve significantly as can be seen in Fig 25 and Fig 26. More specifically Fig 25 shows the substrate produced for layer-1 and Fig 26 shows the substrate for layer-2 as required by the unit cell of the UHF antenna substrate (Fig 9).

Fig 25 Substrate (layer 1-without carbon) produced using compression pressure of :150Bar, Sintered at 1400C for 6h

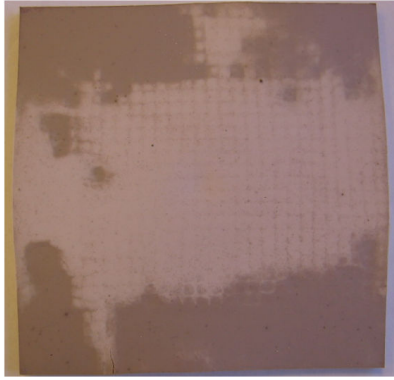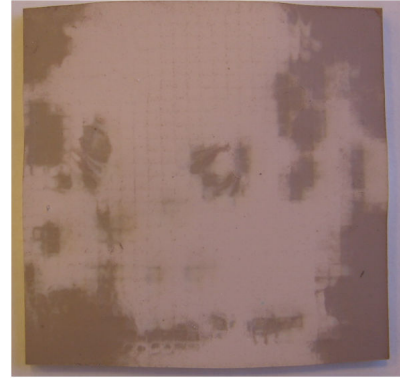Fig 26 Substrate (layer 2-without carbon) produced using compression pressure of :150Bar, Sintered at 1400C for 6h

As a result, compressing the substrate at 150 bar and sintering the substrate at 1400C for 6h without the carbon content resulted in the best morphology and dimensional accuracy because of the optimal shrinkage compatibility attained between the powders.

2.4.3 Experimental Procedure

A wide range of available dielectric constants for commercial Calcium Magnesium Titanates (CaTiO3-MgTiO3-Mg2TiO4 or MCT's) is available and thus was chosen as the main ceramic family for the fabrication study. Two powders in particular from the MCT family were chosen based on their dielectric properties (MCT 20 **k**=20 MCT 70 **k**=70) (Trans- Tech Inc) meeting the design requirements. Although magnetic powder was not used in the fabrication of the UHF SATCOM antenna substrate, it has been characterized for possible future use and compatibility with existing MCT constituents. The characterization studies for the optimal processing conditions of the DPD process starts with the spray dried ceramic powder constituents themselves. Hence, SEM images (FE-SEM Ultra High Resolution GEMINI Column w/EDS) and TGA analysis of the ceramic powders were carried out. The SEM images of MCT 15,20,70 ceramics can be seen in Fig 27-Fig 36. The K15 powder SEM image in Fig 31-Fig 33 clearly indicates the mixture composition of Carbon microspheres-Sigradur K and K20 MCT ceramics. Both powders have a mean particle size of 1-2μm and possess large spray dried agglomerates of 10-180 μm as apparent in their SEM pictures.
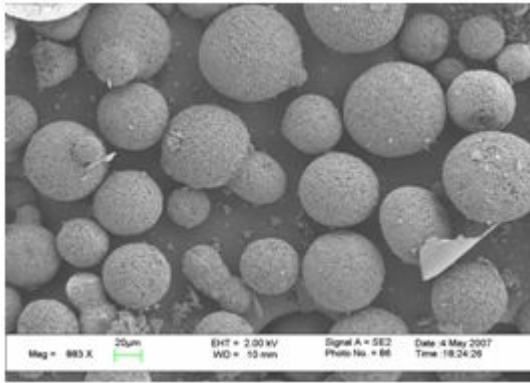
Fig 27 K20-Powder (Mag-883X) SEM
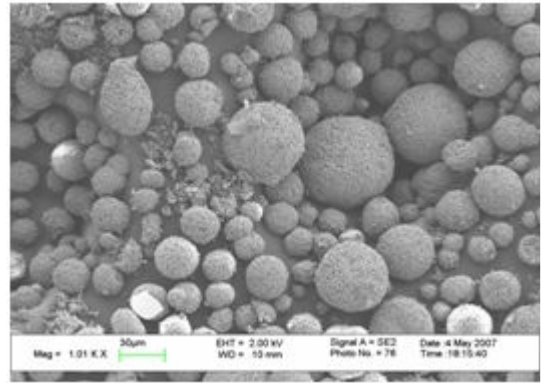
Fig 28 K70-Powder (Mag-1000X) SEM
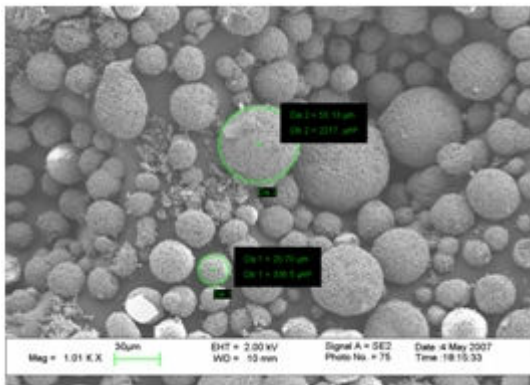
Fig 29 K70-Powder (Mag-1000X)
diameter=53.13 and 20.70μm
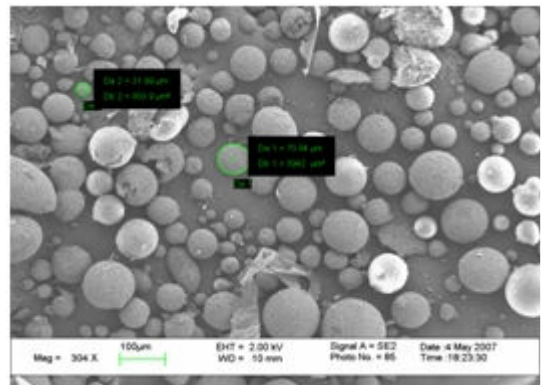
Fig 30 K70-Powder (Mag-304X) diameter=31.99 and
70.84μm
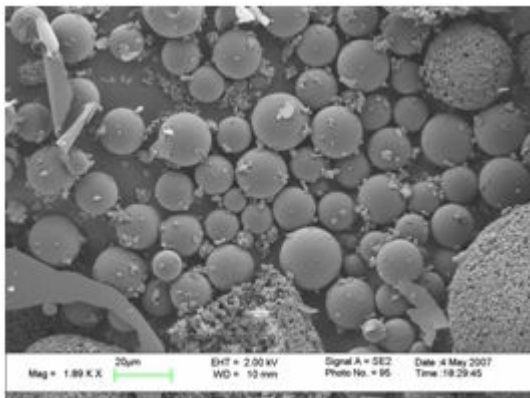
Fig 31 K15-Powder (Mag-1800X) SEM
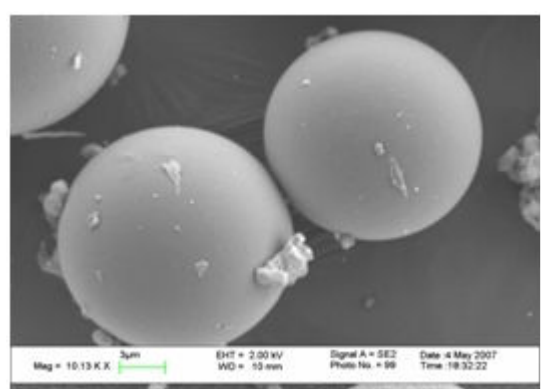
Fig 32 K15-Powder (Mag-10.000X) SEM
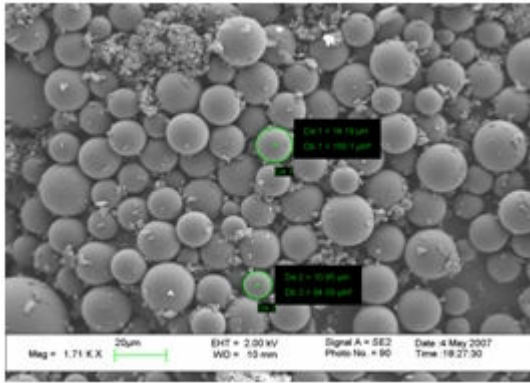
Fig 33 K15-Powder (Mag-1700X)
diameter=14.19 and 10.95µm
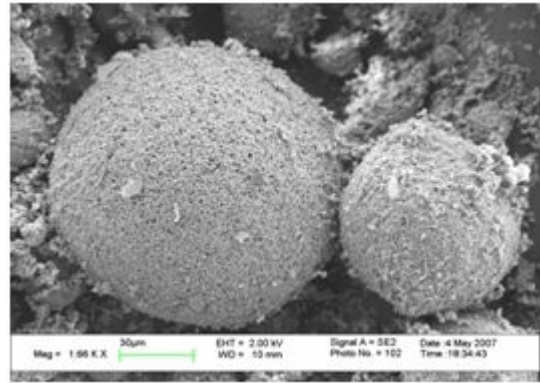
Fig 34 Magnetic-Powder (Mag-1600X) SEM
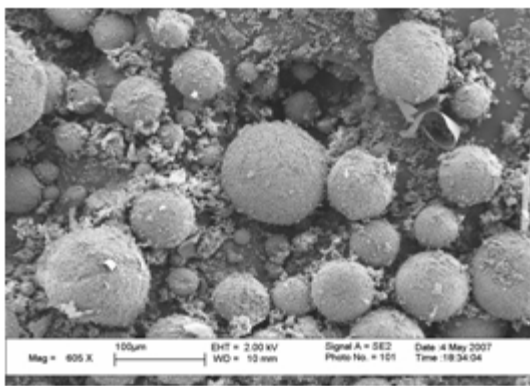
Fig 35 Magnetic-Powder (Mag-605X) SEM
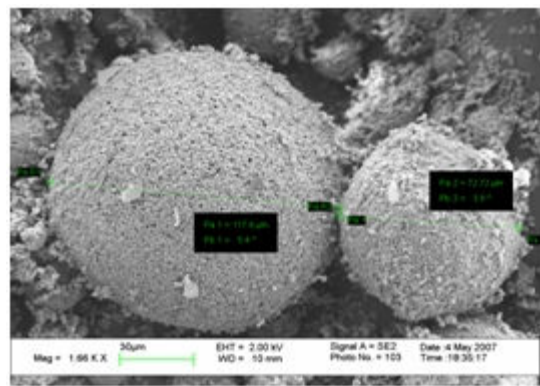
Fig 36 Magnetic-Powder (Mag-1600X)
diameter=117.8 and 72.72µm

According to the SEM pictures, Magnetic powders which are not directly used in the design possess the largest agglomerate size and K70, K20 and K15 design constituents possess smaller average agglomerate sizes which are relatively close to each other on the order of 50µm.

The DPD process relies on several key components such as a female-male assembly die machined to precise dimensions (Fig 39 and Fig 40), a fixture (Fig 37), and patterned transparency films or metal sheets (Fig 38) according to desired material layout of each powder constituent. The fixture to manage powder location was manufactured consisting of 3mm square pixels arranged in a 29x29 rectangular grid. Grid has a size of 101.7x101.7 mm. Fixture wall sizes are 0.6 mm thick and the fixture heights are 10 and 20 mm. The CAD file is used to create a stereo lithographic file which is exported to an Objet Eden rapid prototyping machine to produce a rigid plastic fixture (ABIGEM Teknopark [50]). Transparency films or

26

metal sheets were produced for each material constituent with holes drilled according to desired material distribution layout. These were then used for locating the powders in the designed optimal location. Several dies had to be manufactured for fabricating ceramic substrates using DPD as can be seen in Fig 39 and Fig 40. Similar for the process parameter characterization pellets were manufactured with dies shown in Fig 41 and Fig 42. It is noted that each die, specifically larger versions, did not have exact dimensional tolerances which presented itself as the major bottleneck for many problematic DPD trials. To prevent fabrication of new dies each time as the substrate size changes, a size adjustable version was also manufactured (Fig 43). The high temperature furnace (Protherm PLF 160/30) was used both for pellet and substrate sintering.
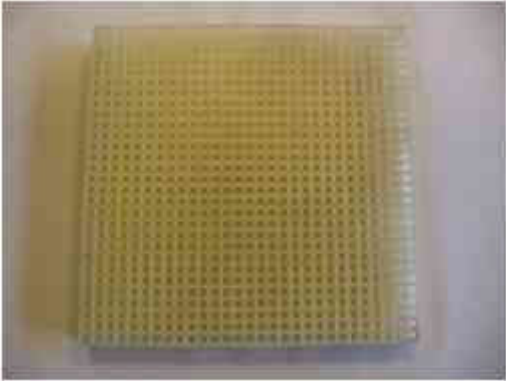
Fig 37 Fixture
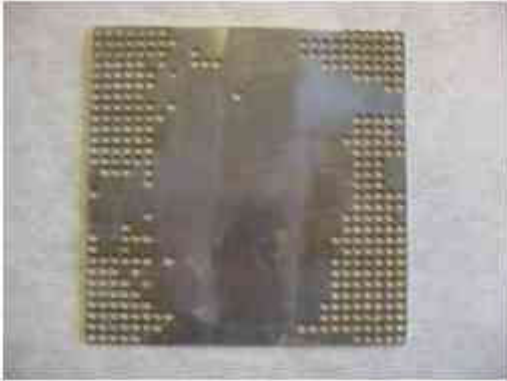
Fig 38 Patterned metal sheet

Fig 39 One of the previous dies (female part) manufactured for substrate fabrication

Fig 40 Last die (female part) for substrate fabrication

Fig 41 One of the previous dies manufactured for pellet fabrication

Fig 42 Last die used for pellet fabrication

Fig 43 A different version of the die which can be adjusted according to desired substrate size

All samples were uniaxially pressed inside a lubricated steel die (with stearic acid-alcohol mixture) at 100-150 bar for 2 minutes. Carbon removal is performed in air using a 10°C/min heating rate to 480°C and a 1°C/min heating rate to 625°C (1 hour dwell). Sintering is performed in air at 1350°C-1450°C (4-6 hours dwell) using a heating and cooling rate of 10°C/min.

Process parameters such as compaction pressure, pressing time, sintering temperature and sintering time were analyzed to optimize the process. For this extensive analysis, pellet substrates with 15mm diameter and 5mm thickness (before pressing) were produced using the MCT ceramic powder constituents. Resulting pellet substrates were characterized using SEM, TGA and dielectric measurements were made using Agilent 16451B Dielectric Test Fixture with Agilent 4294A Precision Impedance Analyzer [54]. Characterization results are given in the next section.

2.5 Results and Discussion

2.5.1 Dielectric Characterization

The material properties of MCT ceramics as cited by Trans Tech, Inc. can be seen in Table 1and Table 2. Dielectric constant measurements of pellets made of spray dried ceramic constituents of K15, K20, K50 and K70 sintered at various dwell time and temperatures and results are given in Fig 44-Fig 47 for dielectric constant and in Fig 48-Fig 51 for dielectric loss measurements, respectively. It is noted that an intermediate shade of K50 was used for characterization purposes although it is not asked for in the UHF SATCOM antenna design substrate. The goal was to characterize the compatibility of intermediate dielectric phases such as K50, which can be easily obtained using mixing existing base phases (of mass ratio %67 K70 and %33 K20) to allow for the use of more dielectric shade compositions in future designs.

COMPOSITION AND TYPE NUMBER	DIELECTRIC CONSTANT (ε')	DIELECTRIC LOSS TANGENT ($\varepsilon'/\varepsilon''$)
MCT-20	20.0 ± 5% @ 9.4 GHz	≤.0015
MCT-25	25.0 ± 5% @ 9.4 GHz	≤.0015
MCT-30	30.0 ± 5% @ 9.4 GHz	≤.0015
MCT-40	40.0 ± 5% @ 6.0 GHz	≤.0015
MCT-50	50.0 ± 5% @ 6.0 GHz	≤.0015
MCT-55	55.0 ± 5% @ 6.0 GHz	≤.0015
MCT-70	70.0 ± 5% @ 6.0 GHz	≤.0015
MCT-85	85.0 ± 5% @ 6.0 GHz	≤.0015
MCT-100	100.0 ± 5% @ 6.0 GHz	≤.0015
MCT-115	115.0 ± 5% @ 6.0 GHz	≤.0015
MCT-125	125.0 ± 5% @ 6.0 GHz	≤.0015
MCT-140	140.0 ± 10% @ 6.0 GHz	≤.0015

Table 1 Table of dielectric constant and loss values of MCT based ceramics

Parameter	Value
Landé g-Factor g-eff	2.11
Line Width δH oe @ -3dB	<=200
Dielectric Constant E'	12.5 ± 5%
Dielectric Loss Tangent Tan=E''/E'	<.0002
Curie Temperature T_c(ºC)	363
Spin Wave Line Width $δH_k$oe	6
Remanent Induction B_r (Gauss)	3800
Coercive Force H_c (oe)	1.5
Initial Permeability μo	317
Saturation Magnetization $4πM_s$	5000 ± 5%

Table 2 Material properties of MCT ceramics

The set of dielectric constant measurements of pellets made of K70, K50, K20 and K15 are given in a decreasing order in the respective figures of Fig 44, Fig 45, Fig 46,and Fig 47, respectively For both the pellets made of K70 and K20 there is a consistent trend of dielectric constant increase up to 1400 C sintering temperature and dwell times 6h and 4h, respectively with increasing temperature and then a decrease with increase in temperature with the exception of an outlier trend for the K70 material at a low temperature of 1300C and 4h, predicting a relatively high dielectric constant of about 60 for the K70 material. The dielectric constants seem to stay fairly constant with respect to temperature up to 65 MHz with a slight increase thereafter and display a dielectric constant range of 46-90 for the K70 and 16-25 for the K20 material, respectively. It is noted that the cited fully dense dielectric constants of 70 and 20 are exceeded during measurements pointing towards measurement errors as will be discussed in the next section. To confirm this behavior a second set of measurements for most pellets were carried out at Ohio State University with Agilent E4991A RF Impedance/Material Analyzer allowing for higher frequency range and direct dielectric constant measurements with overall less inherent equipment error [51]. The E4991A Impedance Analyzer uses an RF-IV technique, as opposed to the reflection measurement technique, for more accurate impedance measurement over wide impedance range. Basic impedance accuracy is +/-0.8%. High Q accuracy enables low-loss component analysis. The internal synthesizer sweeps frequency from 1 MHz to 3 GHz with 1 mHz resolution. The results of these measurements are given in the APPENDIX 1. The measurements carried out

at SU were done using Agilent 16451B Dielectric Test Fixture with Agilent 4294A Precision Impedance Analyzer, which relies on the less accurate contacting electrode method. The accuracy of the Agilent 4294A measurements are provided in its manual with an error prediction of 35% if the sample has a dielectric constant of 50 assuming the samples are ideally flat. The overall dependency of the error with respect to airgap, pellet thickness and dielectric constant is shown in Table 1. Indeed, OSU measurements confirmed the overall trend of the dielectric constant variation for both K20 and K70 pellets including the outlier trend of the K70 material at 1300C 4h. Also, as expected these measurements indicated an overall 25% reduced dielectric constant values with ranges of 13-19.5 for K20 pellets and 46-70 for K70 pellets, hence confirming overpredictions of earlier measurements. The general trend of the dielectric constant measurements and the outlier behavior is re-analyzed using SEM images of these pellets as will be discussed in Section 2.5.1.4, and show a direct dependency on pellet morphology and grain growth.

Fig 44 Dielectric constant versus frequency of K70 ceramics under various sintering conditions

The dielectric constant measurements of pellets made of the intermediate phase K50 material in Fig 45 indicate a different trend for the dielectric constant dependency on sintering temperature and dwell time than the K20 and K70 base materials. The dielectric constant has an overall increasing trend with respect to both sintering temperature and time with the maximum dielectric constant of an average of 80 attained at 1450C for 6h. Again, the lowest sintering temperature of 1300C with a 4h dwell time seem to produce an outlier behavior similar to the one observed for K70 material pellet. Again, when compared with measurements at OSU in APPENDIX 1, the dielectric constant measurements in Fig 45 seem

to be an overprediction with a more realistic maximum dielectric constant value attained around 46 in the case of OSU measurements, which is closer to the expected maximum value of the K50 based on the mixture rule [52]. Again, the outlier and general increasing trend with sintering temperature will be reinvestigated with SEM image comparisons of pellets at respective conditions in Section 2.5.1.4.

Fig 45 Dielectric constant versus frequency of K50 ceramics under various sintering conditions

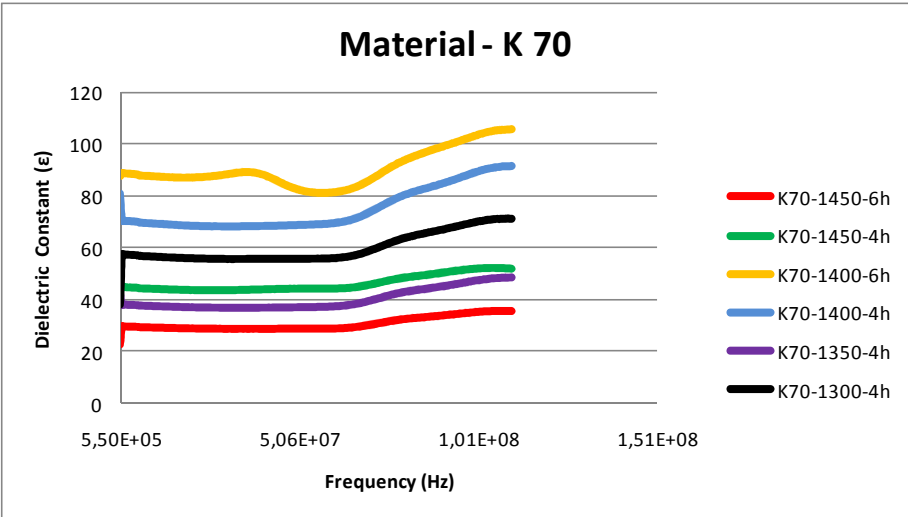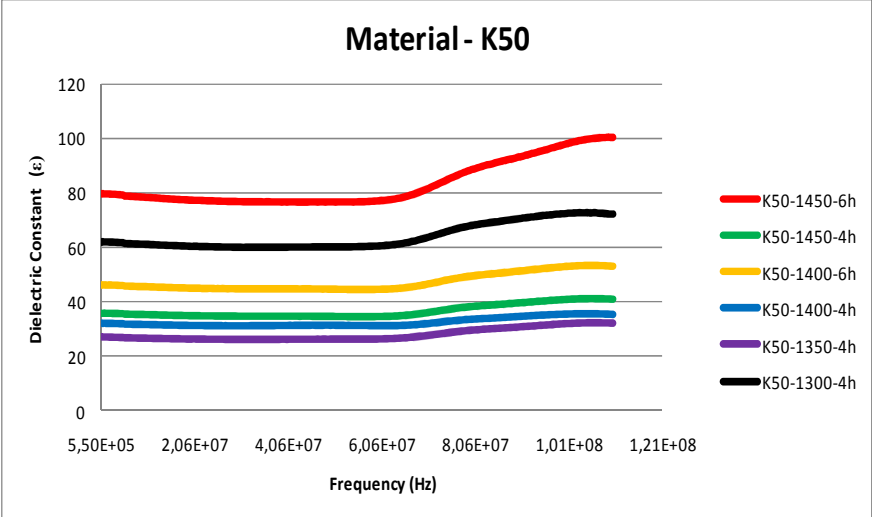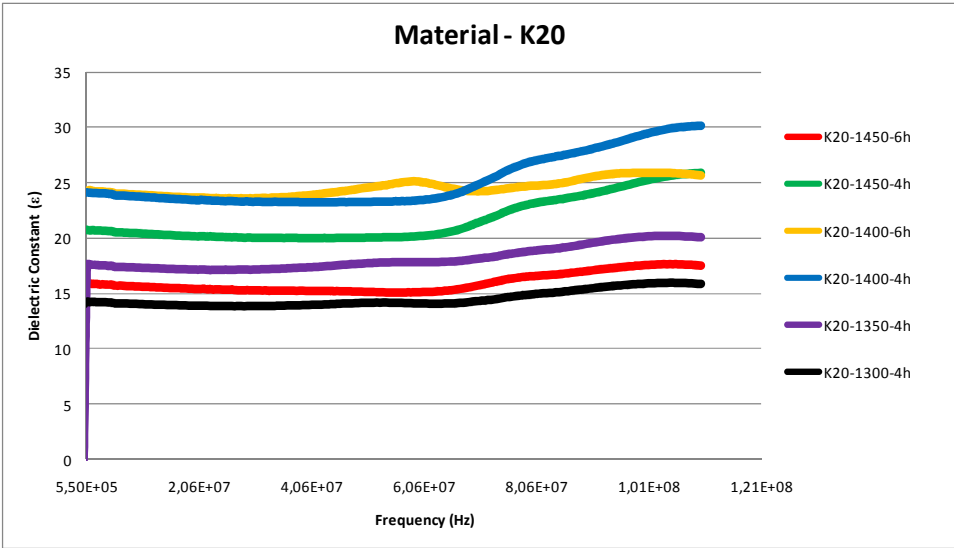

Fig 46 Dielectric constant versus frequency of K20 ceramics under various sintering conditions

Finally, the dielectric constants of K15 materials at several sintering temperature and dwell times are given in Fig 47. The K15 material shows a very similar trend to its base constituent

of K20 in the mixture with an overall increasing trend up to 1400C with dwell time of 6h and a decrease for higher sintering temperatures. The outlier behavior of the 1300C at 4h does also exist. This is an expected behavior as the K15 is basically a mixture of K20 and carbon SigradurK phases with the latter evaporizing at much lower temperatures during sintering. (TGA results to be presented in Section 2.5.1.3 this behavior). It is also noted that the overall resulting dielectric constant range is within 6-14. Due to the relatively large porosities in resulting K15 pellets, OSU measurements could not be performed in a reliable manner since most of the pellets were damaged upon arrival.
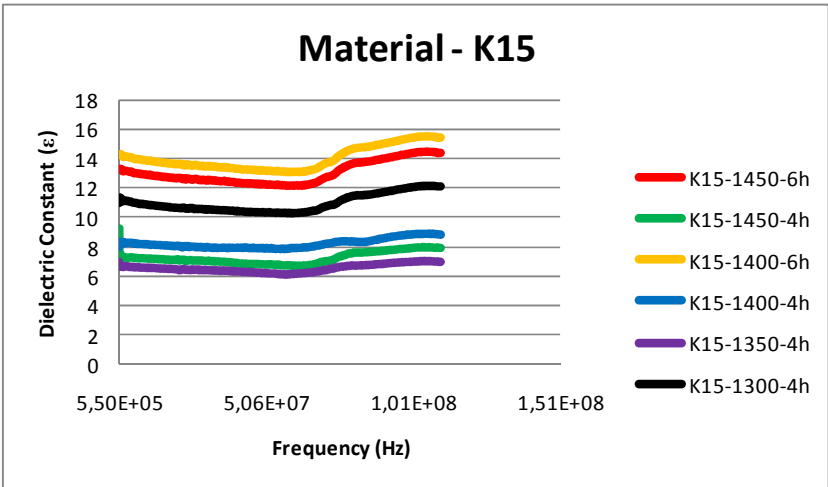
Fig 47 Dielectric constant versus frequency of K15 ceramics under various sintering conditions

Dielectric loss measurements belonging to each material constituent at same sintering conditions were carried out both at Sabanci University and OSU. The former are results are given in Fig 48, Fig 49, Fig 50, and Fig 51 for K70, K50, K20 and K15, respectively. OSU measurements are provided in APPENDIX 1. With an expected overall higher inherent measurement error and very close loss graphs for various sintering conditions for all materials, it doesn't seem very reliable to make a relative sintering condition comparison. However, it can be deduced that again for base materials of K20 and K70 in Fig 48 and Fig 49, respectively the naïve expectation of a higher dielectric constant accompanied by higher dielectric loss seems to be valid. For mixtures of K50 and K15, shown in Fig 50, and Fig 51, respectively, the overall trend predicts an almost opposite behavior in both set of measurements confirmed by OSU measurements in APPENDIX 1. Also, unlike the almost uniform behavior of dielectric constants, loss has an almost linearly increasing behavior with frequency for all materials and an unexpected relatively high loss level of 0.1 unlike the cited

values of around 0.001. Detailed information can be found on the Agilent Solutions for Measuring Permittivity and Permeability with LCR Meters and Impedance Analyzers manual [53]. Analyzing the corresponding OSU measurements with expected more reliable loss values, indeed confirms the erroneous values measured using the material dielectric kit. OSU measurements predict a more reasonable maximum loss tangent value of 0.002 for K20, and 0.003 for K50 and K70 materials with the highest loss attained by the K15 material of 0.005. These loss ranges are consistent with cited reference values.

Fig 48 Dielectric loss versus frequency of K70 ceramics under various sintering conditions

Fig 49 Dielectric loss versus frequency of K50 ceramics under various sintering conditions
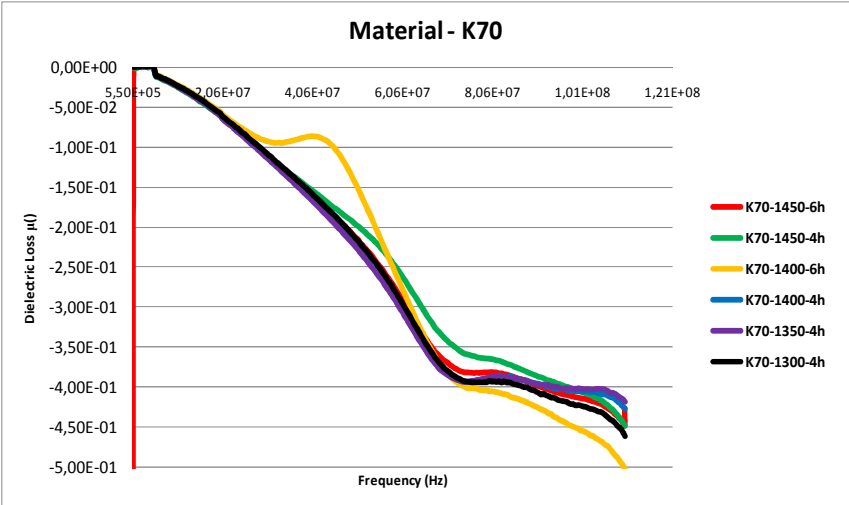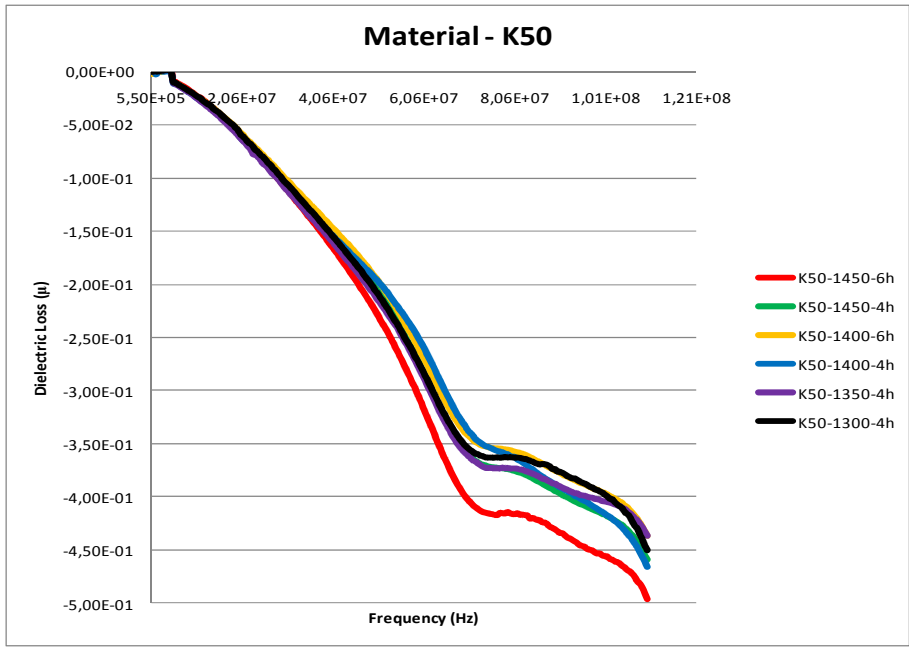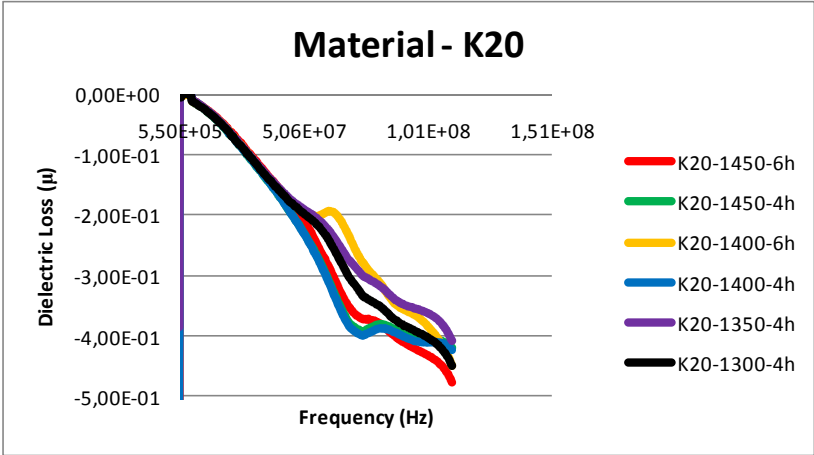

Fig 50 Dielectric loss versus frequency of K20 ceramics under various sintering conditions
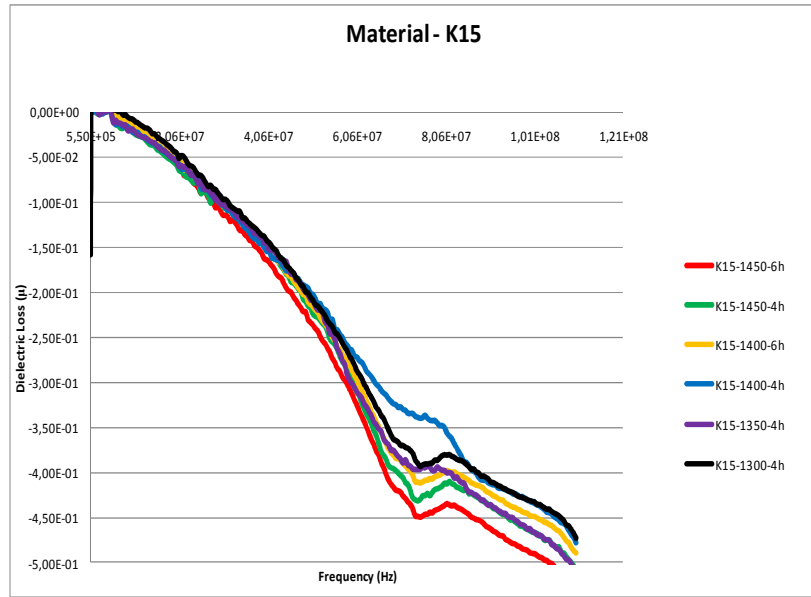
Fig 51 Dielectric loss versus frequency of K15 ceramics under various sintering conditions

It should be also noted that the measurements do suffer from inherent measurement errors for all the dielectric measurements arising from the measurement kit depending on the dielectric constant and geometry of the pellets as shown in Table 3. Here, ε_r' refers to the dielectric constant and t_a is average thickness of the airgap between the pellet and measurement kit electrode and t_m is the average thickness of the material under test.

t_a/t_m \ ε_r'	2	5	10	20	50	100
0.001	0.1%	0.4%	1%	2%	5%	9%
0.005	0.5%	2%	4%	9%	20%	33%
0.01	1%	4%	8%	16%	33%	50%
0.05	5%	16%	30%	48%	70%	83%
0.1	8%	27%	45%	63%	82%	90%

Table 3 Dielectric measurement error of depending on dielectric constant, airgap, and pellet thickness [54]

As evident from these error percentage values, the error increases with the dielectric constant of the material with a possible 90 percentage error for relatively high airgaps with respect to thickness of these pellets (non-smooth pellets or orientation) and a dielectric constant of 100.

36

It is also noted that the pellet preparation involved same exact sintering conditions as cited but a semi-automatic grinding process using Metkon Gripo 1v, hence giving rise to uncontrollable thickness and surface roughness variations. It is also added that a glue was used to that adds to surface uncertainties and possible loss variations of the pellets. Also, some pellet surfaces since too smooth due to overgrinding were annealed by Protherm PLF 160/30 to obtain clear microstructure images using SEM but could as well have damaged the morphology and hence added pellet surface variations affecting the dielectric measurements. In section 2.5.1.4, the SEM images will be analyzed and tried to link to the dielectric measurements by also considering the pellet preparation process variations that is likely to result in discrepancies.

2.5.1.1   Material Shrinkage vs. Sintering Temperature

Major factor that reduces thermal shrinkage mismatch of constituent materials is sintering temperature. In this section this effect is analyzed for base materials of K20 and K70, as well as the magnetic powder which is a Nickel based ferrite, and intermediate shades of K50 and K140 (highest possible MCT available). Results are shown in Fig 52-Fig 55 showing the percentage shrinkages in a promising range for all five constituents starting at 1400 C. Main reason for compatibility is that MCT20 showed considerable increase in volume shrinkage by increasing temperature although MCT70 and ferrite showed relatively similar densification behavior from 1300 C to 1450 C. The thermal compatibility suggests that we dual composites made of MCT70-ferrites could be produced at around 1300 C. Sintering time has low and non-linear effects at temperatures higher than 1300 C. MCT-50, MCT-140 and carbon mixed ferrite, Ferrite-C, showed thermal compatibility at lower temperatures such as 1360C. Their volume shrinkage showed linear dependence on sintering temperature but non-linear dependence on sintering time. For low temperatures such as 1300C, time effect has increasing effect on sintering but at elevated temperatures, the sintering temperature effect overcomes the effect of time.
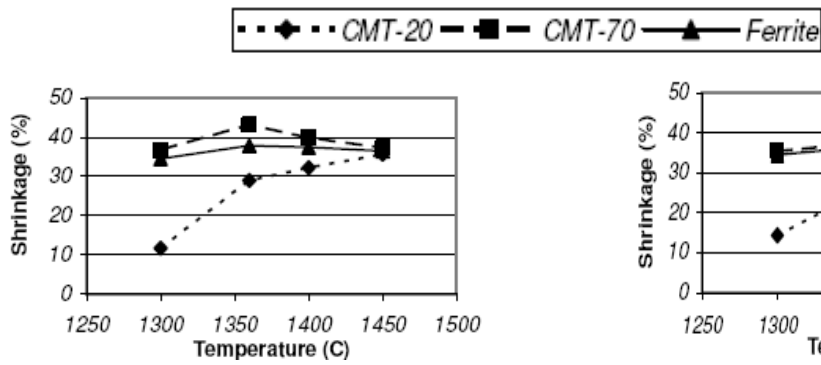
Fig 52 Material shrinkage vs. sintering temperature with 2 hours sintering
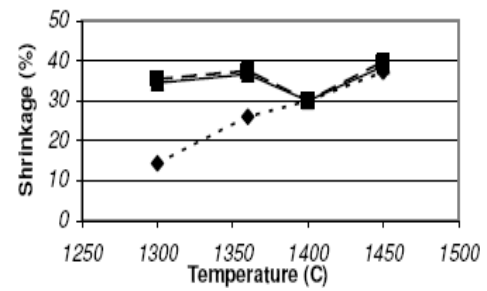
Fig 53 Material shrinkage vs. sintering temperature with 4 hours sintering
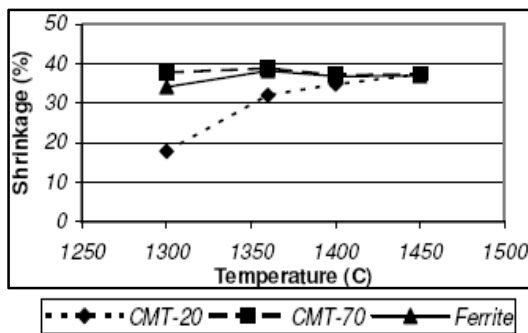
Fig 54 Material shrinkage vs. sintering temperature with 6 hours sintering
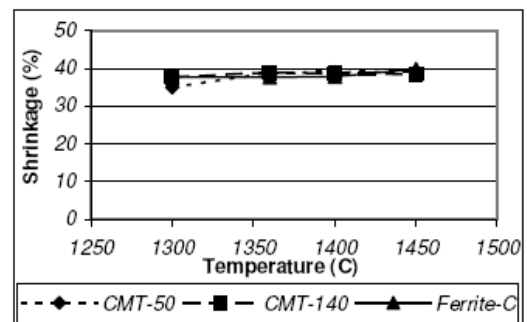
Fig 55 Material shrinkage vs. sintering temperature with 6 hours sintering

2.5.1.2 **Material Shrinkage vs. Pressure**

In Fig 56-Fig 58 the effect of the pressure on the material shrinkage is investigated. It is observed that at 100 bar, pressure has reverse effect on the increasing trend of volume shrinkage by applied external pressure. At 1300 and 1360 C, the effect of press pressure on the materials show similar behavior whereas the shrinkage of MCT20 is still too low (around 15% and 25% respectively) compared to MCT70 and ferrite that display volume shrinkages between 33% and 40 %, shown in Fig 56-Fig 57. Low pressures such as 30 bar were not preferred so as to produce powder compacts that could be handled. Handling becomes more difficult if carbon-mixture constituents are present in the powder compact making the green body looser and easily diffusable. Moreover, at 75 bar, powders showed inconsistent trends

38

from each other resulting in an increase in their thermal mismatch at different temperatures except for 1450C (Fig 56-Fig 58). Therefore, optimum processing pressure for all powders is 50 bar for substrates made of the pellet size. As was shown earlier in Section 2.4.2, the optimal pressure was 150 bar for large monolithic substrates of the UHF antenna.
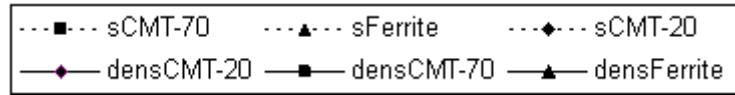
(Dashed lines shows shrinkage, and solid lines shows theoretical density)
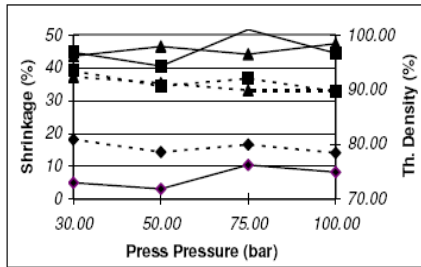
Fig 56 Material shrinkage vs. pressure with sintering at 1300C
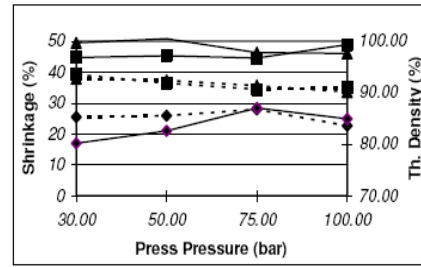
Fig 57 Material shrinkage vs. pressure with sintering at 1360C
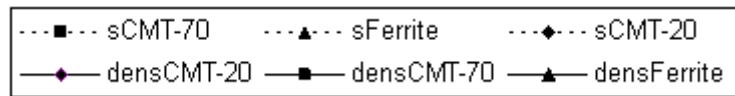
(Dashed lines shows shrinkage, and solid lines shows theoretical density)
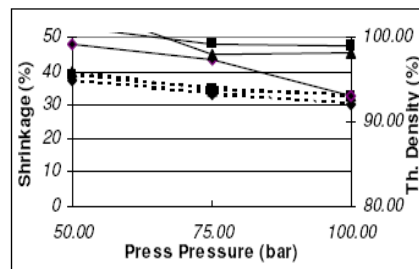
Fig 58 Material shrinkage vs. pressure with sintering at 1450C

2.5.1.3 TGA Results

TGA results of the base ceramic powders K70, K20, and K15 in addition to the Nickel based ferrite are investigated in this section. TGA graphs showed that MCT70 has ~ 3% (Fig 59) and MCT20 has ~ 2% (Fig 60) polymeric binder that was removed between 200 C and 600

C. As there is already low percentage of binder, once slow heating rates are used between 200 C and 600 C we should be able to get rid of defects, porosities and prevent crack formation traditionally present during binder removal process also known as the Binder Burnout Stage. It is also observed that Ni-based ferrite is less flowable than MCT20 and MCT70 due to lower binder content (~ 1%). Carbon microspheres are removed completely by firing between 480 and 625 C [4]. So, heating rates of 10 C/min up to 480 C and 1 C/min between 480 and 625 C respectively, for binder and carbon removal were used. When heating up at 1 C /min at lower temperatures such as 200 C started, it continued until 600 C, no changes (about 1% difference) in the shrinkage rate of samples were observed. So, slow heating rates up until the temperature range where carbon removal takes place could be avoided focusing more on the carbon removal process rather than binder burnout process due to its low content value. As a result, the complete removal of binder was achieved effectively and carbon microspheres pyrolized from the 2D/3D composites between 480 and 625 C.
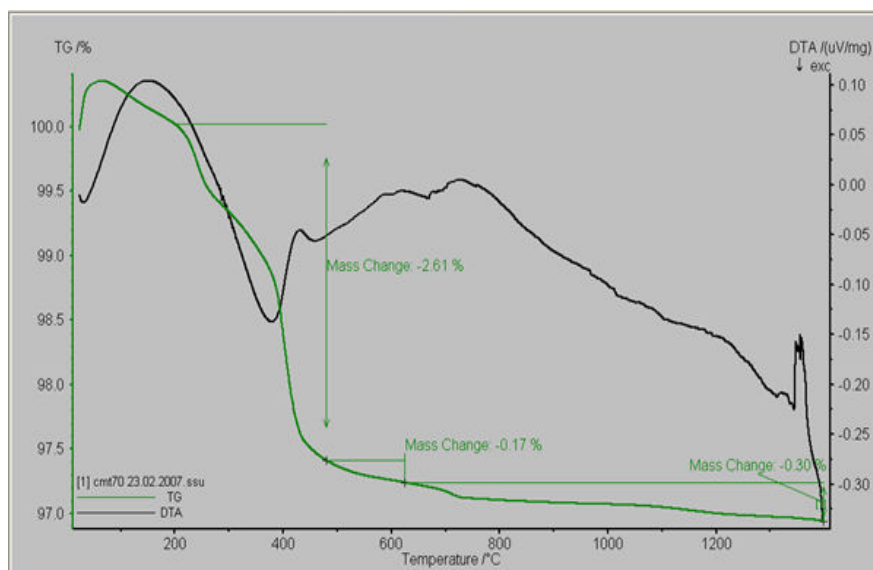
Fig 59 TGA result of a K70 ceramic
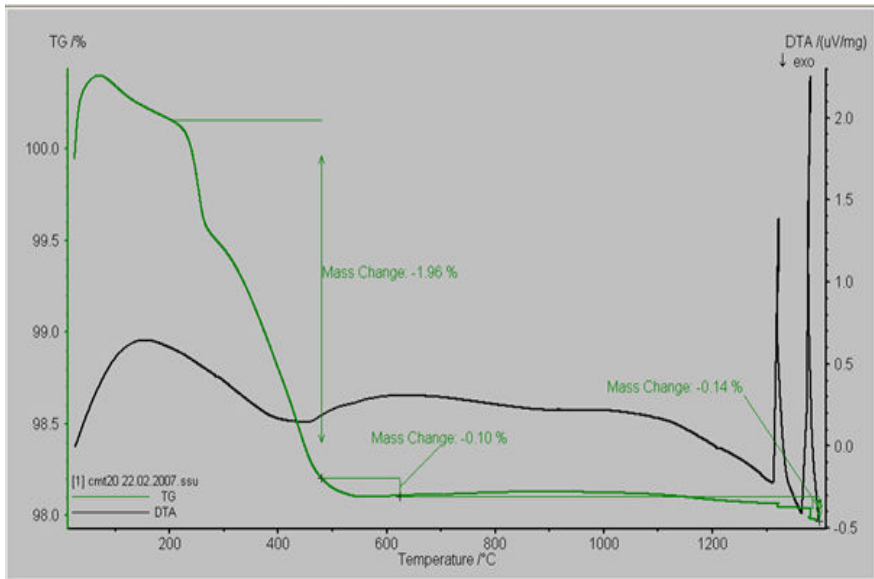
Fig 60 TGA result of a K20 ceramic
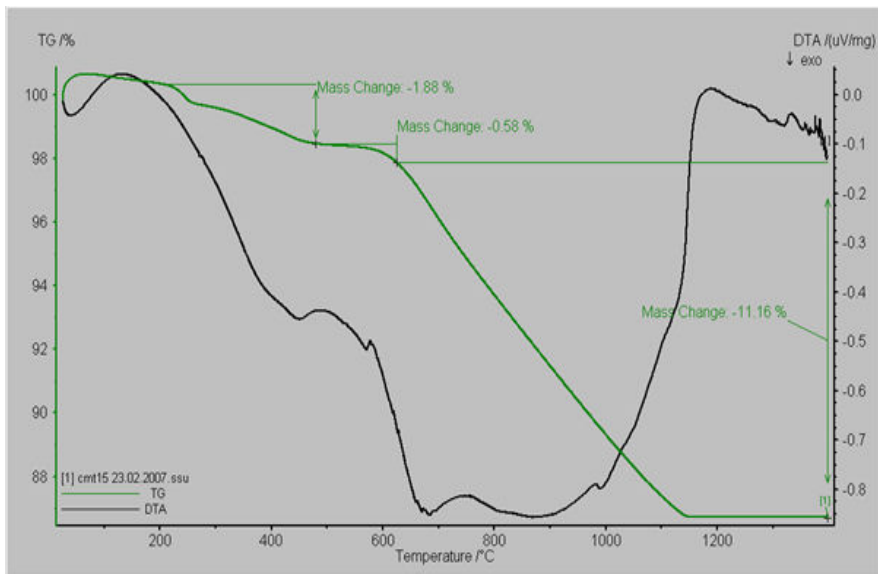
Fig 61 TGA result of a K15 ceramic
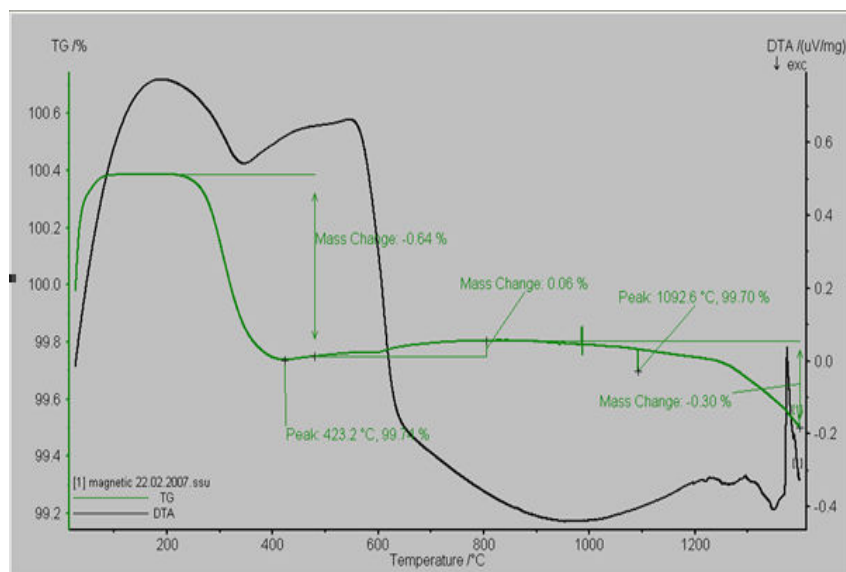
Fig 62 TGA result of a Ni based ferrite

Moderate heat up rate of 10 C/min after 625 C until reaching elevated sintering temperatures were used as no other remainder constituents were present to be removed and a rate of 5 C/min was used during cooling down to room temperature. It is noted that depending on the type of materials, dwell time for carbon removal at 625C is 1 hour and for sintering at temperatures ranging from 1300 and 1500 C is about 4 hours.

2.5.1.4   **SEM Images**

In Fig 63-Fig 87 SEM images of pellets made base material K70 and K50 and mixture phases of K50 and K15 are presented at various magnification ratios. Grain size and grain size distributions were observed and compared at various temperatures. MCT20 and MCT70 showed similar grain size between 5- 10 μm at 1450C and MCT20 had full densification at 1450 C.

Based on the SEM images of K70 at 1450C with 4h and 6h dwell time and 1400C, it is observed that is has a non-uniform large grain size at 1450 C, but rather uniform morphology at 1400C, respectively. Also the grain size is larger with increased temperature indicating that a lower dielectric constant is likely to be associated with larger grain size and uniform morphology might be a result of a higher dielectric constant. The uniform morphology at 1400h might also be associated with the annealing behavior.

42

Fig 63 K70-1400-6h (Mag-5000X) SEM

Fig 64 K70-1400-6h (Mag-10.000X) SEM
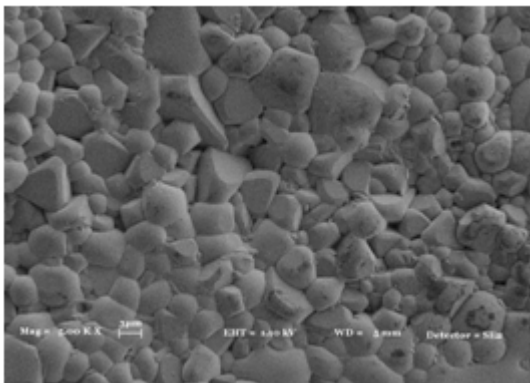
Fig 65 K70-1450-4h (Mag-5000X) SEM
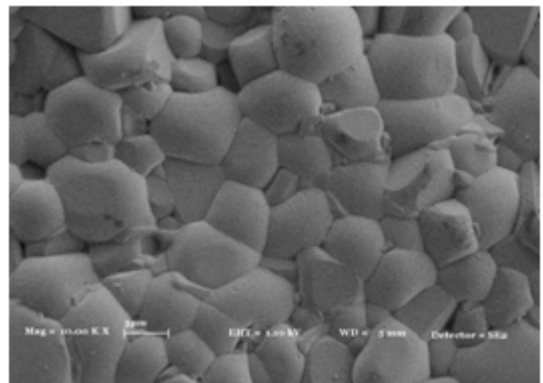
Fig 66 K70-1450-4h(Mag-10.000X) SEM
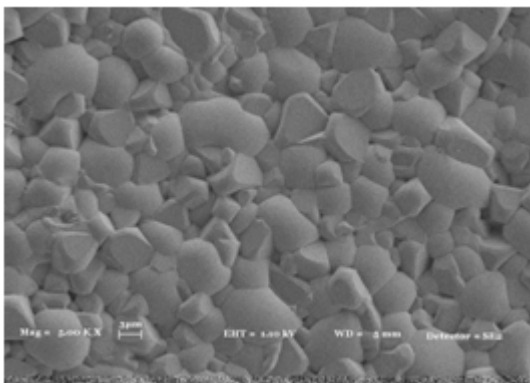
Fig 67 K70-1450-6h (Mag-5.000X) SEM
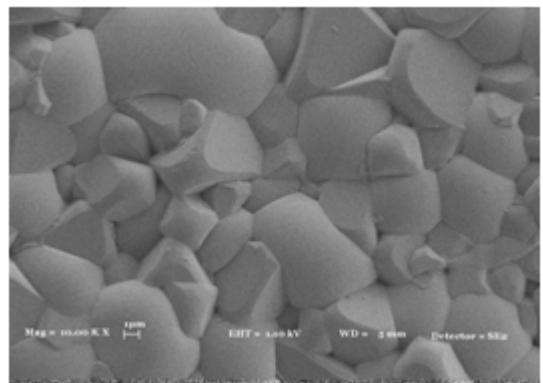
Fig 68K70-1450-6h (Mag-10.000X) SEM

A similar observation can be made for the K50 material in Fig 73 and Fig 74 with a uniform morphology being observed for 1450C 6h, which is the sintering condition that exhibited the highest dielectric constant and can be linked again to the annealing effect unlike grain boundary visible SEM images of unannealed samples. K50 material fully

43

densifies at 1300C for 4h (Fig 69-Fig 70), has larger grain size at 1400C, and uniform morphology at 1450C.
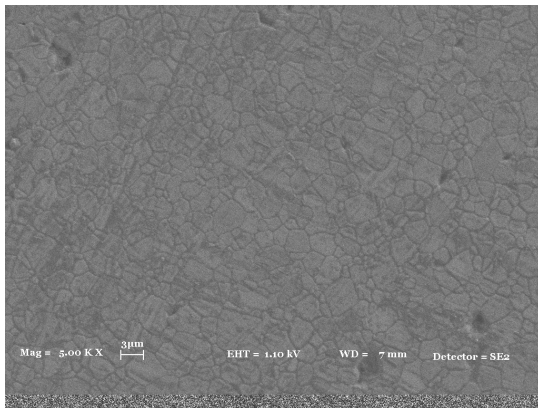
Fig 69 K50-1300-4h (Mag-5.000X) SEM
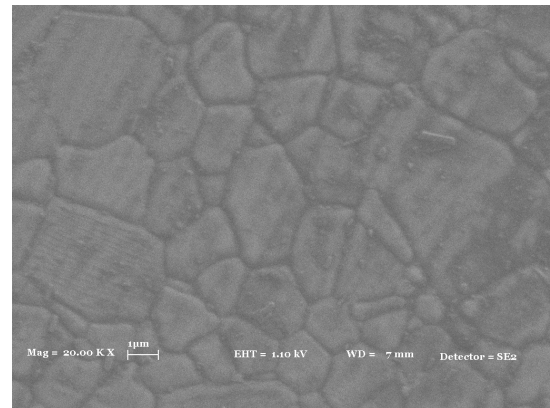
Fig 70 K50-1300-4h (Mag-20.000X) SEM
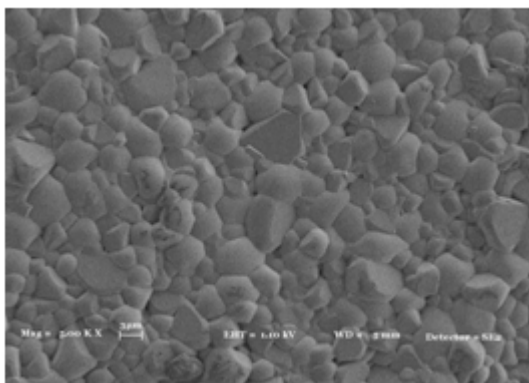
Fig 71 K50-1400-4h (Mag-5.000X) SEM
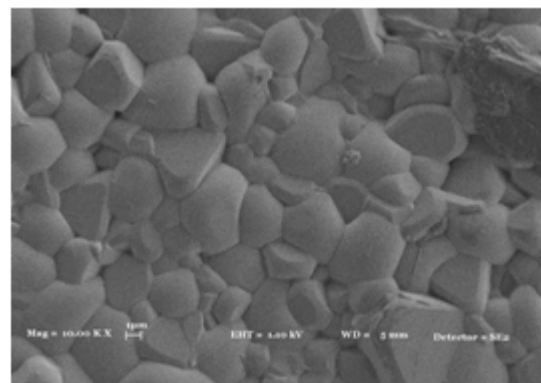
Fig 72 K50-1400-4h (Mag-10.000X) SEM
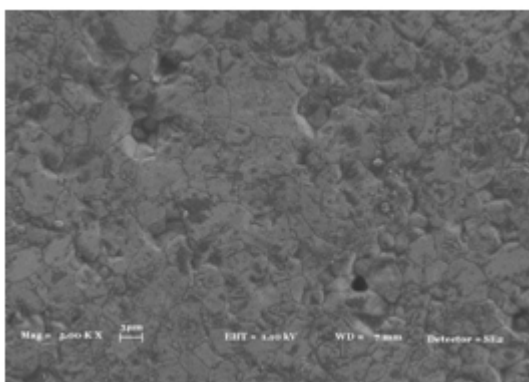
Fig 73 K50-1450-6h (Mag-5.000X) SEM
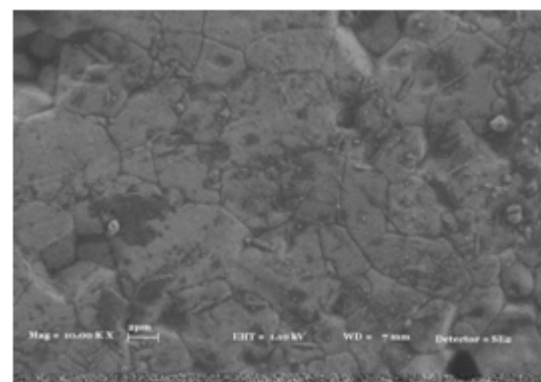
Fig 74 K50-1450-6h (Mag-10.000X) SEM

Based on the SEM images of the K20 materials, shows a consistent trend with non-uniform and larger grain size at 1450C 6h and an annealed surface morphology observed at 1400C 4h associated with annealing very similar to the microstructures of both the K70 and K50 materials. Hence the grain size and morphology effect is consistent with earlier conclusions based on the highest dielectric constant observed for 1400C 6h for K20 materials.
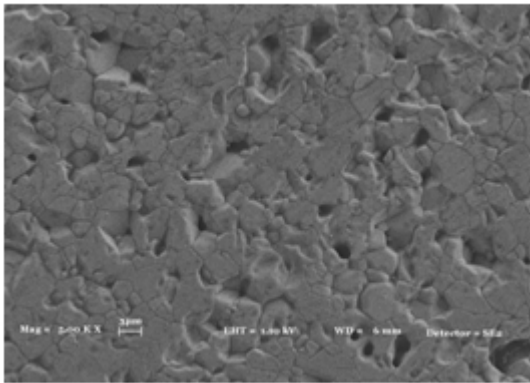
Fig 75 K20-1400-6h (Mag-5.000X) SEM
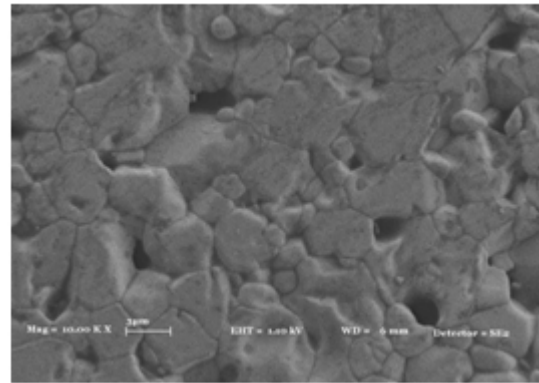
Fig 76 K20-1400-6h (Mag-10.000X) SEM
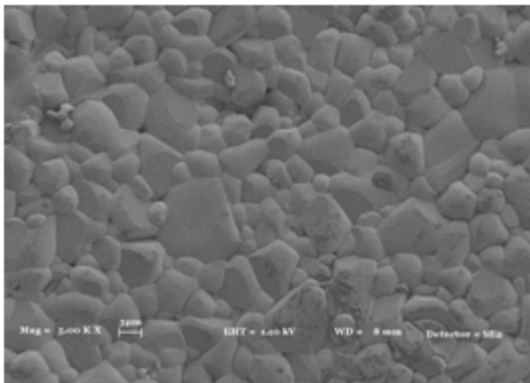
Fig 77 K20-1450-6h (Mag-5.000X) SEM
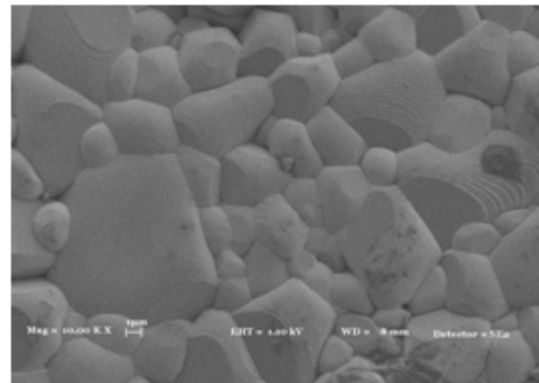
Fig 78 K20-1450-6h (Mag-10.000X) SEM

Based on the SEM images of the K15 intermediate phase made of Carbon and K20, it can be concluded that even at high temperatures of 1400C the K15 material did not fully densify unlike others. The grain sizes are strongly non-uniform especially at higher temperatures than 1400C possibly giving rise to the dielectric constant decrease. It is also observed that the porosity has a direct effect on the increasing loss of the dielectric with lower temperatures. Hence, there is a tradeoff between loss controlled by porosity and the dielectric constant mainly controlled by grain size and uniformity.
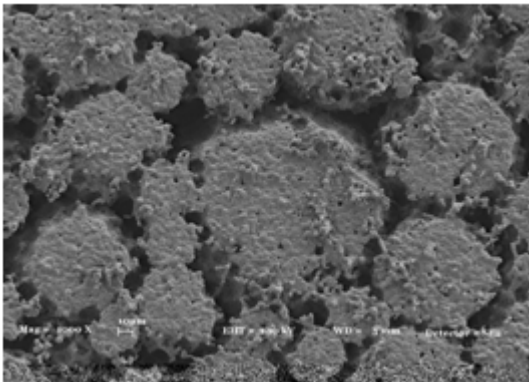
Fig 79 K15-1350-4h (Mag-1.000X) SEM
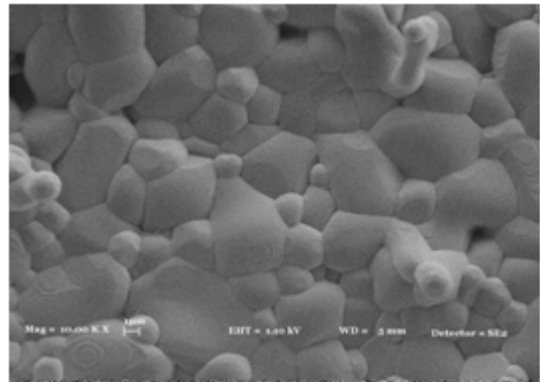
Fig 80 K15-1350-4h (Mag-10.000X) SEM
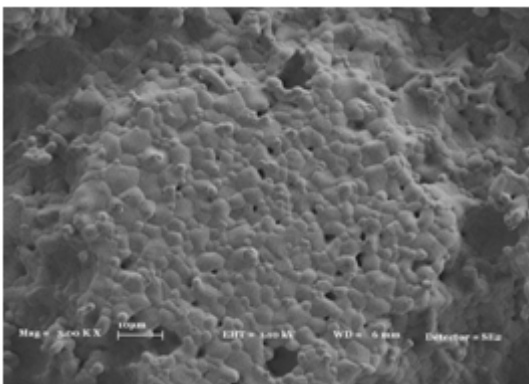
Fig 81 K15-1400-4h (Mag-3.000X) SEM
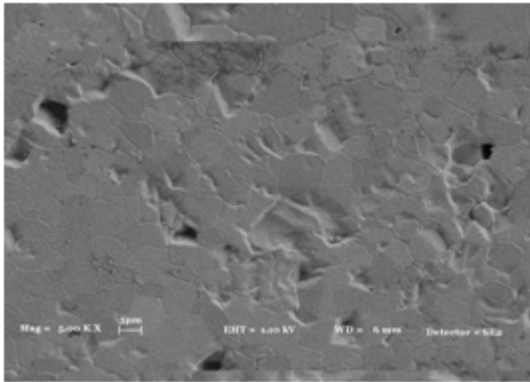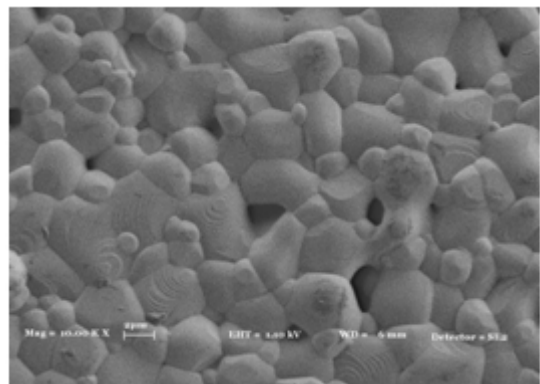

Fig 82 K15-1400-4h (Mag-10.000X) SEM
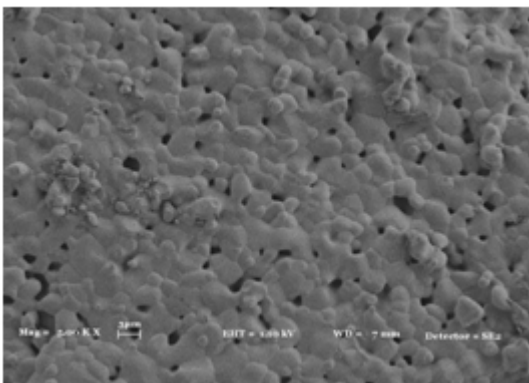
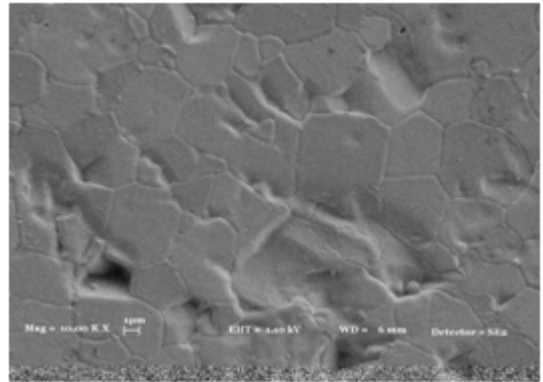Fig 83 K15-1400-6h (Mag-5.000X) SEM
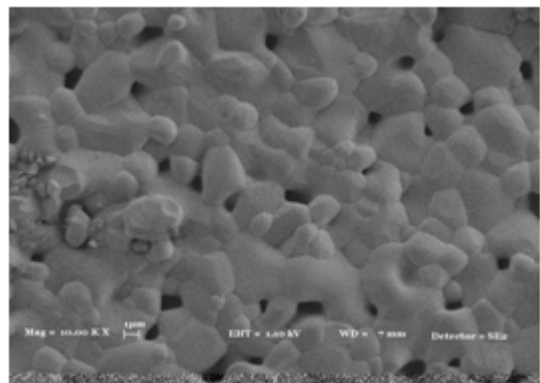
Fig 84 K15-1400-6h (Mag-10.000X) SEM
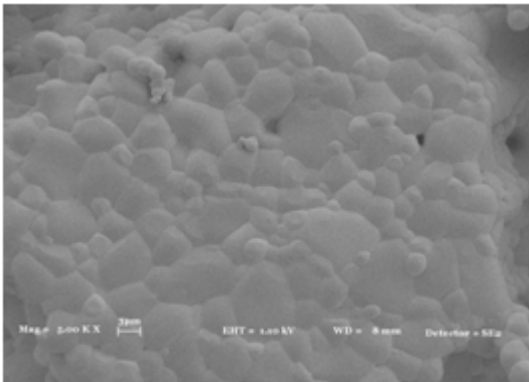
Fig 85 K15-1450-4h (Mag-10.000X) SEM
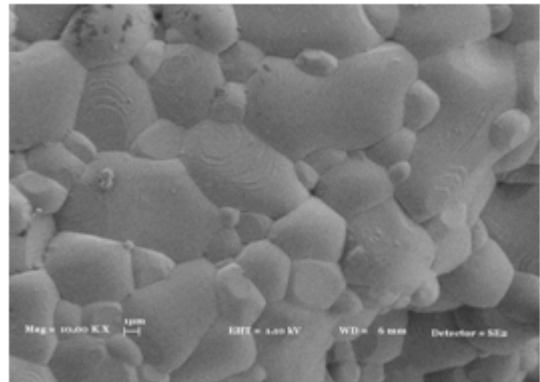
Fig 86 K15-1450-4h (Mag-10.000X) SEM
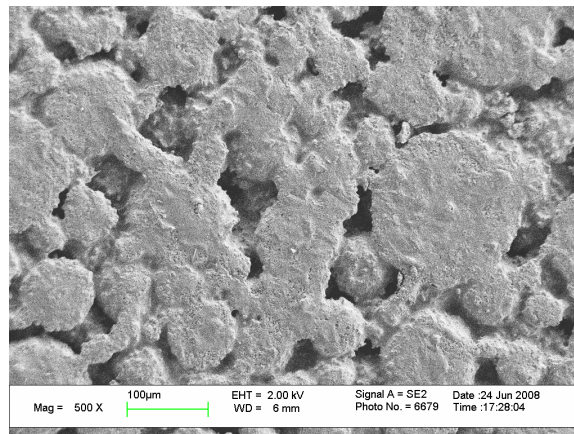
Fig 87 K15-1450-4h (Mag-500X) SEM

2.6   Conclusions

Process parameters of a simple manual -Dry Powder Compacting Method (DPD) - were optimized to demonstrate that DPD is capable of producing multi-layer multi-ceramic variations in 3D for large substrates (size up to ≈ 82x82mm). This technique was specifically devised to produce volumetric multi-material variations resulting from stringent performance specifications for antennas using off-the-shelf powders. Some conclusions regarding presented results are as follows:

47

TGA, SEM images and density calculations reinforced that full densification of MCT20, MCT70 and Ni-based ferrite pellets were obtained with compatible shrinkage and eliminated cracks, warpages and undesired porosities. Although shrinkage behavior of ferrite and MCT70 are compatible if sintered at 1300 C, shrinkage mismatch with MCT20 could be minimized only by increasing sintering temperatures up to 1400C. Broader particle size distribution may have effect on lower compaction of MCT-20 compared to MCT-70 and ferrite at the same temperature.

- Press pressure of 50 bars and layer thickness of 5 mm refer to optimum process conditions for the six constituent materials for small size pellets.
- Press pressure of 150 bars and sintering temperatures of 1450C for at least 4 hours or 1400 C for at least 6 hours with material constituents of K20- K70 (without Carbon content based K15) refer to optimum process conditions for large monolithic substrates of spatially variable ceramics.
- Both density measurements and SEM images proved that shrinkage behavior of ferrite and MCT70 are compatible at 1300 C and have the potential to perform as a monolithic magneto-dielectric composite.
- Porosity can be overcome in the expense of grain size with higher sintering temperature.
- Grain size and morphology controls permittivity of ceramics and needs further investigation
- Mixing of powders and porosity formers alters the sintering process and needs further investigation
- Dielectric measurements show that dielectric constants of base materials prompt for an optimal sintering temperature close to 1400C and 4-6 h dwell times, but this does not hold for the case of intermediate phases and carbon based mixture phases.
- Overall, MCT's show close values to desired dielectric constant and relatively low loss (≈ 0.001) at near to optimal processing conditions but a more detailed analysis with alternative measurement techniques need to be performed to arrive at more robust conclusions possibly avoiding process variations in the fabrication of test materials.

- Dielectric permittivity and permeability can be tuned by mixing existing dielectric and magnetic shades and allow for the realization of multi-layer multi-ceramic variations of design optimization studies for variety of RF devices with enhanced performance.

Despite its lengthy procedure, the main advantage of DPD over traditional assembly processes is that during dry powder pressing, the deformation is axial, so any transverse design can be preserved. Automation efforts could readily adapt DPD for conventional industrial practice, replacing the simple powder feed in an automated compaction machine with an appropriate feed mechanism for each composition. The automation of DPD is likely to result in a versatile and effective 3D fabrication technique that will allow for the practical fabrication of exact designs in feasible time spans. It is expected to evolve as an ideal practical technique to produce multi-material novel material compositions of future antennas. Additional aspects related to the extension of the method with various magnetic and conductor inclusions to produce a complete antenna structure will allow the design and realization of these materials to provide previously unobtainable figures of merit and new capability for a wide range of operating frequencies

3 DESIGN OPTIMIZATION FRAMEWORK FOR NANO ANTENNAS

In general design problems can be classified into topology, shape, and size optimization whether carried out intuitively or via optimization, where the design variables are topology, boundaries, and proportions, respectively. Optimization is the method of maximizing or minimizing a preferred objective function while satisfying a set of constraints. A design optimization cycle normally consists of a synthesis module and an analysis module. The synthesis module contains a precise optimization algorithm and the analysis module computes the objective function and its derivatives, if a sensitivity analysis is essential by the preferred optimizer. Nearly all optimization algorithms are iterative methods and have their own manner of searching towards the optimum solution. Specifically for antenna design optimization problems, the desired performance characteristics are described and formulated in terms of an objective function, such as bandwidth, antenna length, antenna width, beam angle (which is releated with length and width), frequency response, temperature, power, efficiency or similar. The analysis module most commonly consists of a finite element analysis code, since the antenna structure and boundaries are complex for deriving a closed-form solution satisfying Maxwell's equations otherwise.

Mathematically, an optimization problem can be defined as the following:

$$\text{Minimize: } f(x,p)$$
$$\text{Subject to: } g(x, p) \leq 0$$
$$h(x,p) = 0$$

Where $x \in x \subseteq R^n, f: R^n \to R, \ h: R^n$ and $g: R^n \to R^s$ $\in x \subseteq R^n, f: R^n \to R, h: R^n$ and $g: R^n \to R^s$. Here, x is the design variable vector in the design space x, the vector p contains certain parameters with values fixed during optimization, f(x,p) is the objective function, the g(x,p) vector is a set of inequality constraints and h(x, p) denotes the equality constraints. The set of x that satisfy all constraints is called the feasible region.

In the most general form, the above formulation is a constrained nonlinear programming (NLP) problem. Optimization problems can be classified in a number of ways such as constrained or unconstrained problems, integer or real-valued programming problems, and component or system design optimization problems, etc. Most familiar classification is to differentiate them whether or not they rely in the evaluation of gradients as gradient based/local or global/heuristic techniques and are discussed next.

3.1   Overview of Optimization Algorithms

3.1.1   Gradient Based Optimization Techniques

These techniques typically involve a smaller number of iterations when compared with global techniques and therefore are faster. These algorithms use first and generally the second derivative of the objective and constraint functions and apply this information to position the optimum. Their dependence on the starting point of the search is a drawback. At that juncture, the user is responsible of making a smart estimation and defining a high-quality starting point to hit upon the optimum point. Unless certain conditions such as convexity are not satisfied, their main difficulty is getting stuck at a local optimum. At each step of a gradient based optimization algorithm a new iterate x_{k+1} will be suggested based on the previous iterate x_k, a move step α_k and a search direction s_k as follows $X_{k+1} = X_k + \alpha_k s_k$.

The iteration continues until a specific convergence criterion is met such as the difference of successive iterates dropping below a small number ε . An additional common termination criteria is the Karush-Kuhn-Tucker norm [55] such as $\| \nabla f_k + \lambda_k^T \nabla h_k + \mu_k^T \nabla g_k \| \leq \varepsilon$.

Traditional gradient based methods for unconstrained non-linear programming problems consist of: Cauchy, conjugate gradient and quasi-Newton methods. The most popular one Sequential Quadratic Programming will stand out as a successful technique to effectively solve problems with nonlinear constraints and is employed in the design framework as the local optimization technique, details of which are discussed in the next section.

3.1.1.1 Sequential Quadratic Programming (SQP)

SQP is based on the scheme of reducing the complication of the problem by sequentially solving less complex quadratic sub-problems with gradient methods. As the complexity of the original problem is reduced, this method is predictable to be faster to solve the original non-linear problem. For a specified optimization problem:

$$\text{Minimize } \mathbf{f}(x)$$
$$\text{Subject to } h(x) = 0;$$
$$g(\mathbf{x}, \mathbf{p}) \leq 0$$

where f(x) is the objective function and h(x) is the vector of equality constraints.

Again the iteration stops when an optimum is reached in the standard gradient based optimization setting and follows below steps:

1) Initialize the system

2) Solve the problem

3) Minimize a merit function along s_k by performing a line search to determine the step length α_k

4) Set $x_{k+1} = x_k + \alpha_k s_k$

5) Check for termination, go to step 2 if not finished

In the proposed framework the SQP algorithm in MATLAB, namely the fmincon function has been used [56].

3.1.2 Heuristic Based Optimization Techniques

One disadvantage of gradient based techniques as explained above such as for SQP are that they are extremely probable to converge to a local optimum depending on the characteristics of the optimization problem and the preference of the initial design point. Conversely, heuristic methods do not rely on local information such as the gradient and therefore have the

ability to look for global optima. Essentially heuristic methods check on a larger design space with increased boundary, and in response rely generally on many more computations, for this reason bear usually from slow convergence and impractical design time period. This computational trouble is even more marked for design problems with high number of design variables such as topology design efforts of frequency based electromagnetic problems. Most common design optimization studies within the electromagnetic community have been limited to the use of heuristic methods such as the genetic algorithm and to parametric design studies. Fundamental principles of GA's will be discussed next. Applications of GA's exist in a wide variety of application portfolio ranging from the high speed integrated circuit to the simulations of the electromagnetic materials. Practical applications suggest that it is usually quite successful in dealing with complex design problems but there is no guarantee that it always converges. Genetic Algorithms are employed here to compare its performance with local based optimizers. As it will be discussed later, it turns out that the analysis module suffers from numerical instabilities and hence despite its long computational time requirements, heuristic based tools seem to be more suited for the design of nano-antennas.

3.1.2.1 Genetic Algorithm

The heuristic based method, Genetic Algorithm (GA) is a robust smart optimization algorithm that gives the global optima with no requirement for the derivative properties of the function with the usage of a system that imitates the behavior of the natural world's population's genetics and progress [56].

In a GA every species stand for a variable in the problem. The algorithm looks for the fittest of the individuals by combining the individuals from each species with each other randomly. The algorithm goes on to select the individuals to breed until it finds the fittest in the population. Once it places the fittest in one population it continues to breed the populations until it finds the fittest in the subsequent population. This process of mixing individuals is similar to the process of crossover in nature.

In a typical GA scenery, the user decides on certain parameters such as the size of the initial population, mutation ratio, and crossover ratio. The requirement formutation is to bring in variety and avoid the design candidates to be too much 'alike', i.e., distributed homogenously

within the population which reduces the quality of the search and hence the results of the algorithm. So, at some generations, the individuals are changed/renewed to prevent too similar design candidates. The fitness criterion is also defined by the user, which itself is a challenging task for any optimization model.

A new generation is started each time until a termination condition has been reached. Termination criteria consist of:

- A solution is found that satisfies minimum criteria
- Fixed number of generations reached
- Allocated budget (computation time) is reached
- The highest ranking solution's fitness is reaching or has reached a plateau such that successive iterations no longer produce better results
- Manual inspection
- Combinations of the above

In general, even if a GA is very capable of providing high-quality solutions to complicated problems, they offer no guarantee of global optimality in finite time. They are very sensitive to tuning parameters and they don`t eliminate risk of premature convergence but they are the common choice for problems where the calculation of derivative information is either impractical or unreliable

3.2   Analysis Tool: High Frequency Structure Simulator (HFSS)

HFSS is the industry-standard software and utilizes 3D full-wave Finite Element Method (FEM) to calculate the electrical performance of high-frequency and high-speed components. With HFSS, network parameters (such as S, Y, Z) can be extracted, 3D electromagnetic fields can be visualized, broadband SPICE models can be produced, and optimize design performance. The software is widely used for antennas, RF/microwave components, the design of on-chip embedded passives, PCB interconnects and high frequency IC packages. HFSS describes the electrical performance of components and estimates signal quality, including transmission path losses, reflection loss due to impedance mismatches, parasitic coupling, and radiation.

The graphical interface of HFSS allows designing for variety of geometric shapes in 3D from its drawing tools. It also gives the opportunity to create different kinds of analyses on the same model with no interaction with each other [57]. Also, HFSS software is a simple to use one, particularly the joint usage of it with the Matlab toolbox provides the users the ability to work on a diversity of fields. As it uses Microsoft Graphical User Interface for windows, the designer can view his exact design in three dimensions. It also gives the freedom to compute performance metrics for a broad range of frequencies which makes it appropriate mainly for antenna designs and high speed integrated circuits. Furthermore, adaptive meshing is probable for complex geometries which make it suitable for iterative based design studies. These features and the convenient script recording feature are among reasons HFSS has been chosen as the major analysis model for the proposed design optimization framework. It is used for the design of plasmonic nano-antennas in this thesis.

The most important feature of HFSS scripting is based on the capability of recording design steps into a script file and that the script file can be transformed into a Matlab file. That provides the user the ability to work on Matlab, call HFSS from Matlab and do the design steps automatically. In the script the user can assign variable names to some critical settings like the frequency, antenna geometry, permeability of a user designed material and that makes it quite easy to call the necessary files and each time evaluate the antenna for a different design setting. Furthermore, the results can be exported to an external environment such as a text file and these can be read by Matlab to be fed into desired optimization module which will be discussed next.

3.3   Proposed Design Optimization Framework

The main structure of the proposed design framework is summarized in this section. In Fig 88 the modular structure of a standard design framework for material based design efforts is shown. The analysis tool within the framework is the commercial Ansoft HFSS package. Since design optimization requires successively changing design variables at every iteration, an API library is used to integrate HFSS with the framework. Afterwards, the optimization module such as GA/SQP and the analysis module HFSS are linked to each other which forms the design optimization cycle.
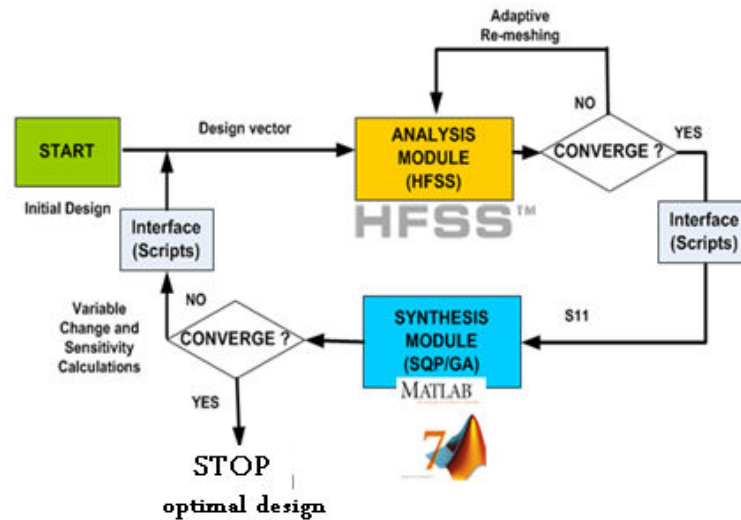
Fig 88 Matlab based design optimization framework

3.4   Design Example

3.4.1   Optimization of a Nano-Plasmonic Antenna

In this study, the proposed design framework is used to optimize nano-antennas. Nano-optical applications, for instance data storage [20] and scanning near-field optical microscopy [16] require intense optical spots beyond the diffraction limit. Nano-antennas can achieve very little optical spots, but their capability to achieve optical spots beyond the diffraction limit is not satisfactory for practical applications. As well as a very small optical spot, a nano-antenna should supply high transmission efficiency for practical applications. The transmission efficiency of a nano-antenna determines the data transfer rate of storage devices and scan times of near-field optical microscopes. As a result, the efficiency of nano-antennas should be optimized for possible utilization in convenient applications. Optimization of nano-antennas is critical for understanding their potential and limitations for emerging plasmonic applications. A brute-force optimization study of these structures is not practical due to large number of parameters. There is a need for a systematic optimization of these structures.

56

To investigate the design space of a dipole nano-antenna shown in Fig 5 , first some brute force simulations are carried out. The incident wavelength is varied from 400 nm to 2000 nm by intervals of 50 nm. At each wavelength, antenna length L is changed from 10 nm to 300 nm. The intensity at the center of the gap, $|E(x=0,\ y=0,\ z=0)|^2$, is calculated for each wavelength and antenna length. By recording the intensity over the rectangular grid, the surface graphs are formed. A constant power value of 1 mW is chosen.

The surface plasmon resonances of nano-antennas depend on parameters related to the shape and composition of the nano-antennas. Inclusive understanding of surface plasmon resonances of nano-optical systems involves an in depth understanding of possibly many more design parameters, geometries, and material properties. The large number of parameters involved in studying functional plasmonic devices with a brute force numerical parameter simulation is not practicable. To design novel nano-optical transducers a modeling based automated design optimization framework is required. In this thesis such a basic framework is developed.

The design framework is formed by integrating a commercial electromagnetic analysis tool Ansoft HFSS with MATLAB's optimization toolbox. Specifically, two different optimization tools are integrated on a MATLAB based scripting interface to iteratively search for optimum geometric parameters of a dipole antenna: Sequential Quadratic Programming (SQP) and Genetic Algorithm (GA). The optimization model consists of maximizing the center field intensity $|E(x=0,\ y=0,\ z=0)|^2$ subject to bound constraints of [10, 300] and [400, 2000] for geometric length and wavelength, respectively.

3.4.1.1 Nano-Antenna Response Obtained via Brute Force Simulations

Prior to the nano-antenna design using the formal optimization framework, to validate the analysis model and investigate the performance of the optimization algorithms, three different brute force analyses were carried out . In the first case, the center field intensity $|E(x=0,\ y=0,\ z=0)|$ is calculated while incident power is assumed to be 1V/m, the nano-antenna wavelength is held constant at 850 nm but the nano-antenna length is varied between 0-215nm and results

57

for this case are plotted in Fig 89. The maximum point of intensity occurs between for dipole lengths of 100-110 nm. For the same exact model to nail the maximum point of intensity and search for a possible second peak, simulations with finer frequency discretizations were carried out with length ranges of 102-111nm and 136-145nm and results are shown in Fig 90 and Fig 91, respectively. The maximum peak in the first case is observed at a length value of 108-109nm with no higher point of field intensity occurring in the second range. However, depending on length discretizations, the intensity value is observed to oscillate rather than experiencing a monotonic increase or decrease pointing towards non-smooth performance response and possible numerical instabilities.

   The second type of brute force simulations were carried out to calculate the center field intensity square $|E(x=0, y=0, z=0)|^2$ via HFSS with an incident power of 1mW where this time both dipole length and wavelength were varied within [10, 300] nm with a step size of 10nm and [400, 2000] nm wavelength with a step size of 50nm, respectively. Results of the square of intensity field vs. wavelength and dipole length are shown in Fig 92. Maximum points are determined as and noted on the figure. These simulation results will serve as benchmark numbers to be compared with the optimal points using SQP and GA in the following sections. The last brute force study was carried out to investigate the behavior of the absorbed power ratio (absorbed power/input power) of the nano-antenna as shown in Fig 93 in addition to the field intensity ratio (output E/ input E) and results are shown in Fig 94. These results belong to simulation with the same ranges of [10, 300] nm and a step size of 10nm for dipole length; and a range of [400, 2000] nm and a step size of 50nm for wavelenth, respectively.   In some sense, a tradeoff design objective space by using brute force simulations is created. Alternatively, Pareto optimal points for a general nonlinear multicriteria optimization problem could be found via Das and Dennis' method known as Normal Boundary Intersection [24], aimed at capturing the tradeoff among the a variety of conflicting objectives. This method is totally independent of their relative scales of the functions and is quite successful in producing an evenly distributed set of points in the Pareto set given an evenly distributed set of 'weights', a property which the popular method of linear combinations lacks. Additionally, this process can be simply extended in case of more than two objectives while retaining the computational efficiency of continuation-type algorithms, which is an improvement over homotopy techniques for tracing the tradeoff curve [58] and presents the major future work.

The intensity at the center of the gap |E(x=0, y=0, z=0)| is plotted for various L at λ=850 nm
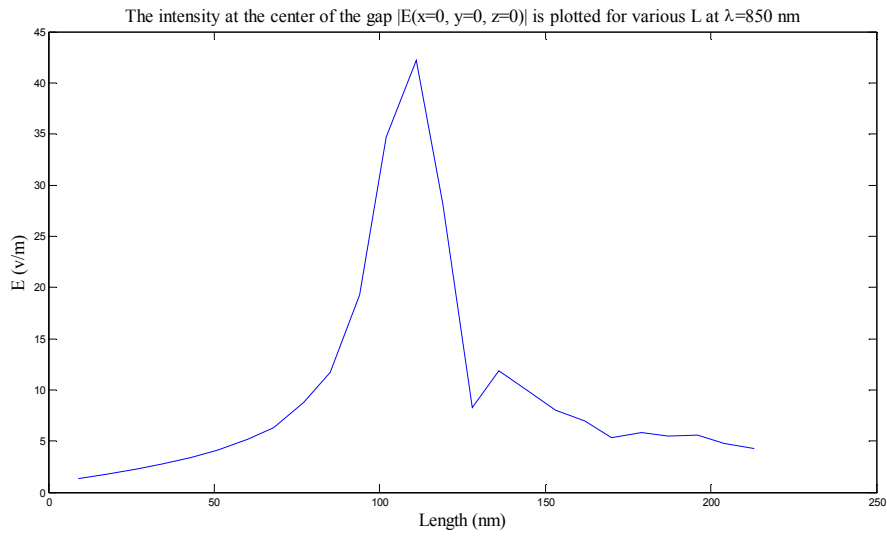
Fig 89 Field intensity at the center of the gap |E(x=0, y=0, z=0)| is plotted for various L(0-215nm) at λ=850 nm

The intensity at the center of the gap |E(x=0, y=0, z=0)| is plotted for various L at λ=850nm
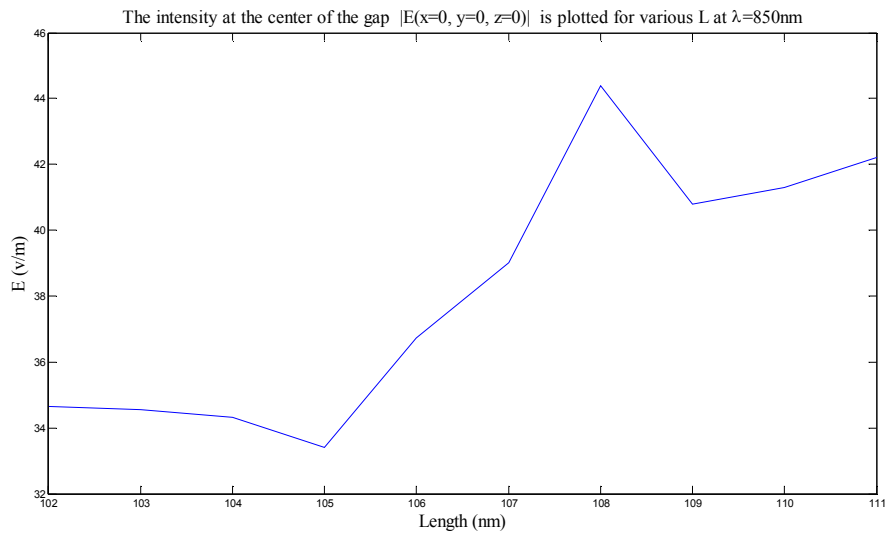
Fig 90 Field intensity at the center of the gap |E(x=0, y=0, z=0)| is plotted for various L(102-111nm) at λ=850nm
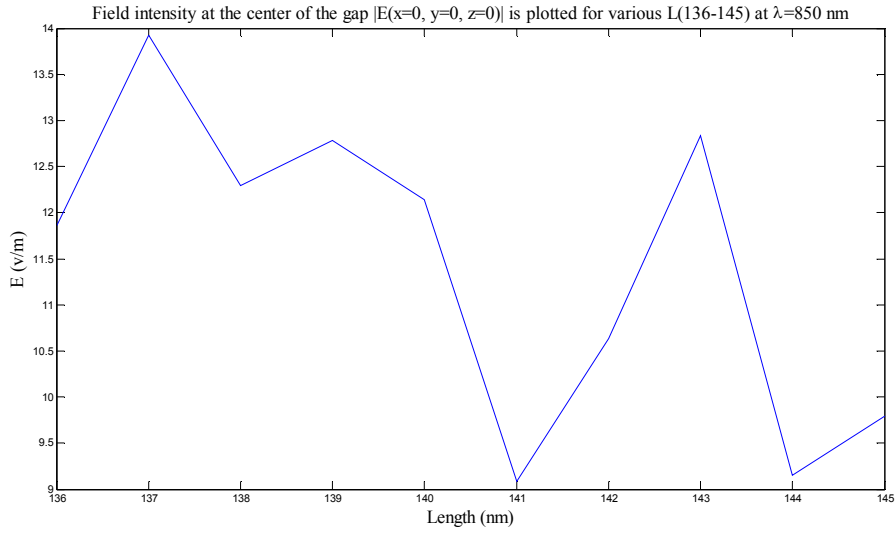
Field intensity at the center of the gap |E(x=0, y=0, z=0)| is plotted for various L(136-145) at λ=850 nm

Fig 91 Field intensity at the center of the gap |E(x=0, y=0, z=0)| is plotted for various L(136-145) at λ=850 nm

Square of the field intensity at the center of the gap

Fig 92 Field intensity square at the center of the gap |E(x=0, y=0, z=0)| is plotted for various L(10-300) and λ (400-2000)

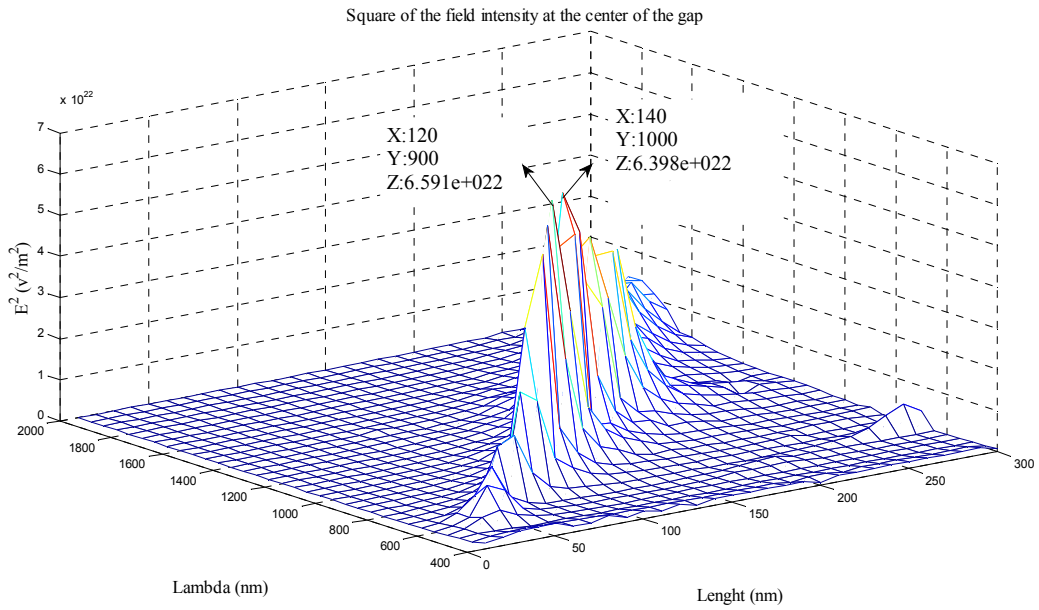According to Fig 93, power absorbtion ratio has an overall increasing trend with higher dipole lengths and smaller wavelengths. Again a non-smooth behavior and possibly numerical instabilities are observed depending on discretization of both quantities.

Power absorbtion ratio (absorbed power / input power)
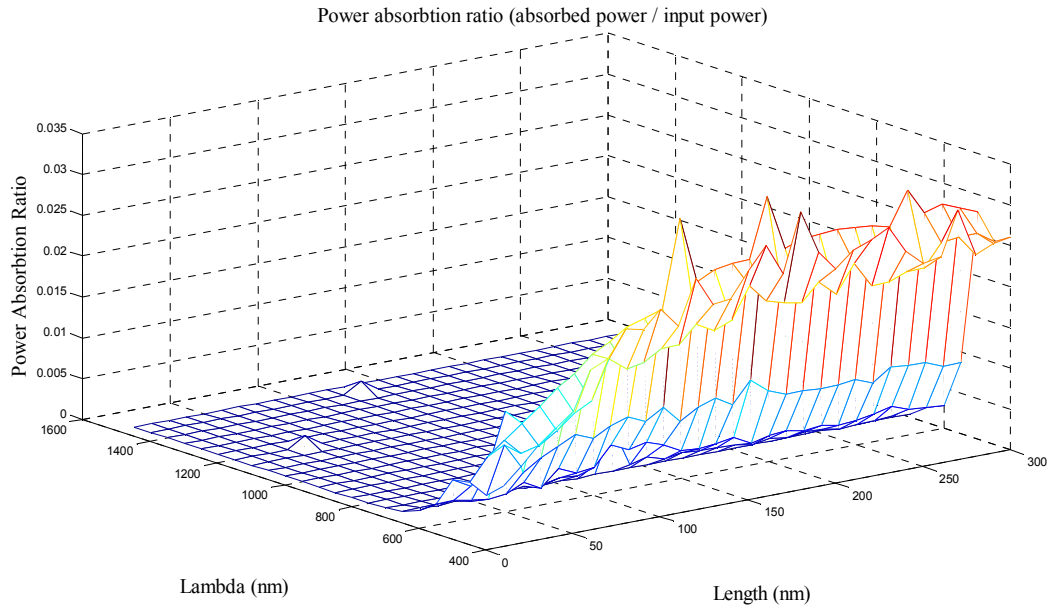
Fig 93 Power absorbtion ratio (absorbed power/input power) at the center of the gap is plotted for various L(10-300) and λ (400-2000)

According to results in Fig 94, the maximum field intensity ratio of 1.291 occurs at a wavelength of 800nm and a length of 120nm. When compared with earlier (second) brute force simulation results indicating two peak candidates with length of 120nm and wavelength of-900nm wavelength, and length of 140nm and wavelength of 1000nm in Fig 92 these results seem not to agree. It is noted that brute force simulations have several differences including input power, type of the incident wave and one measure being the square of intensity of the other in addition to the discretization and instability issues noted earlier. More specifically, incident power is 1V/m, incident wave is a plane wave and output is the square of the field intensity in brute force simulations of Fig 92 whereas incident power is 1mW, incident wave is a focused incident wave and output is the ratio of the field intensity in Fig 94.

Field intensity ratio (output E/input E)
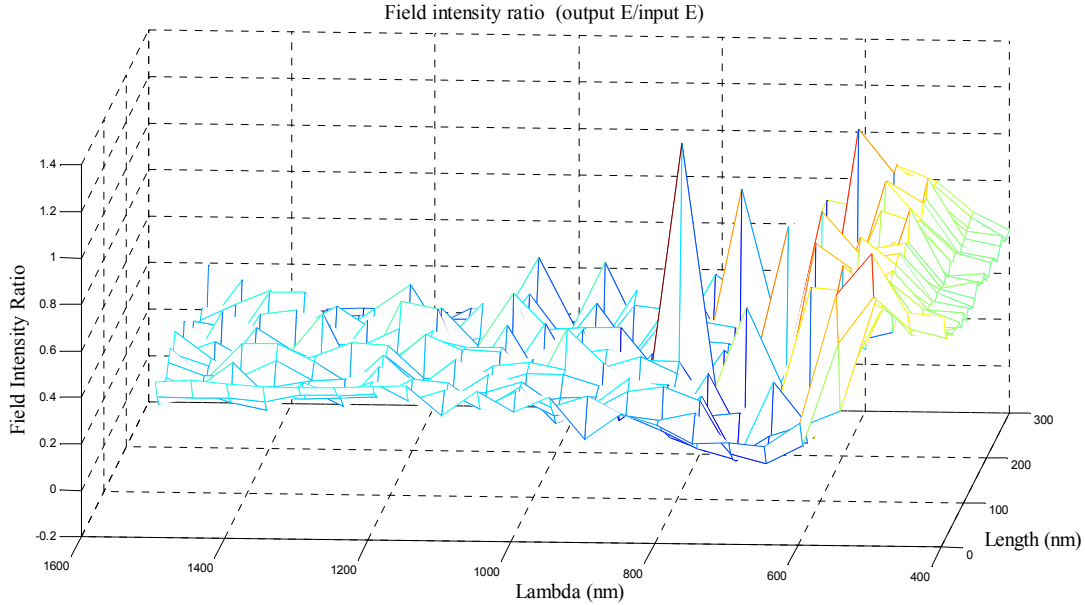
Fig 94 Field intensity ratio at the center of the gap is plotted for various L(10-300) and λ (400-2000)

3.4.1.2 **Gradient Based Method Results via SQP***:*

In this section results using the SQP based gradient optimization method are presented and compared to previous brute force simulations shown in Fig 92. Optimization results are plotted on the brute force simulation results for easier comparison as shown in Fig 95- Fig 106. It is noted that the SQP simulations are carried out using MATLAB's optimization toolbox and the function fmincon. The algorithms were integrated to the HFSS analysis tool using a script based programming environment in Visual Basic. Also, the optimization algorithm options were tuned for the problems considered in this section as the following: termination tolerance on the function value (TolFun) is 1E-10, termination tolerance on variable X (TolX) is 1E-6, minimum change in variables (DiffMinChange) is 5, maximum change (DiffMaxchange) is 1 and maximum iterations (Maxiter) is set to 100, respectively.

After validating the integrated script-based optimization framework and optimized option settings, the first optimization attempt results are obtained as shown in Fig 95. Black dots are the field intensities the SQP optimization tool traced during its convergence history with an initial value for the length variable of 50nm and a fixed wavelength parameter at λ=850nm. For a better comparison, the zoomed version of the graph is depicted in Fig 96. Although

close to the region containing the maximum point, the optimization algorithm did not converge to the expected brute force result. The converged results are given in Table 4:

Initial L	Initial λ	Converged L	Converged λ	Converged E^2	Iteration
50	850	88	779	7,74E+22	22
100	850	108	846	8,84E+22	12
150	850	104	833	8,97E+22	13
50	1000	147	1015	6,89E+22	16
100	1000	139	994	7,00E+22	18
150	1000	143	996	7,06E+22	13

Table 4 The convergence history obtained from SQP results (L=length, λ=wavelength, E^2 = field intensity square)

Fig 95 SQP result with the initial value of L=50nm, λ=850nm – entire graph

Fig 96 SQP result with the initial value of L=50nm, λ=850nm – zoomed area

In a second attempt with a different initial length value of 100nm and a wavelength of λ=850nm, the results plotted in Fig 97 are obtained. Here, black dots are the field intensities traced by the SQP optimization tool during the design cycle. The scaled-up version of the same graph is shown in Fig 98. It can be seen that the performance is better than the first trial in Fig 95 in nailing down a closer shot towards the peak region of the brute force simulations since the initial value of 100nm is closer to the expected maximum point and the local optimizers are known for their initial point dependencies. However, the converged intensity result of 8,84E+22 v^2/m^2 at L= 108nm and λ=846nm is different than the expected brute force results of 6,591E+22 v^2/m^2 at L=120nm λ=900nm and 6,398E+22 at L=140nm and λ=1000nm due to numerical instabilities and discretization dependencies.
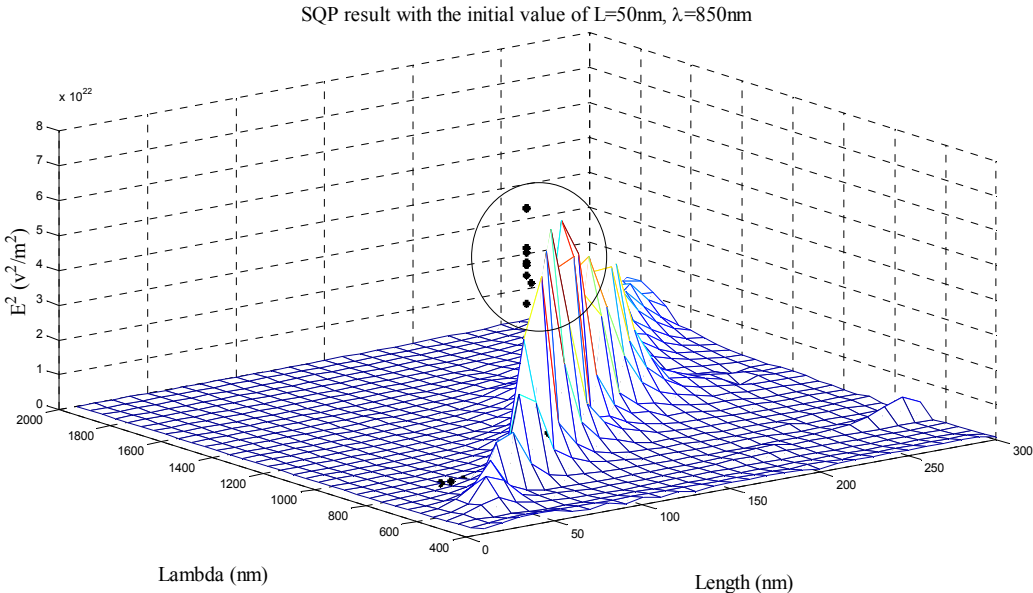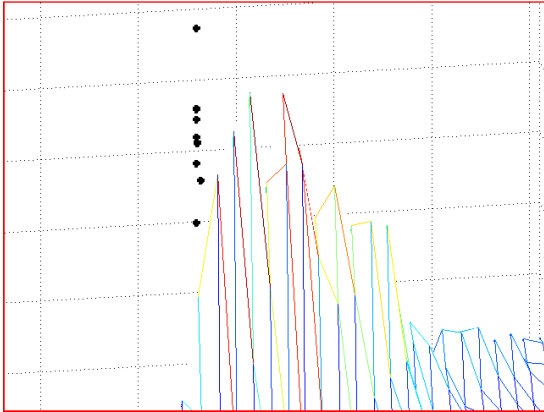

Fig 97 SQP result with the initial value of L=100nm, λ=850nm – entire graph
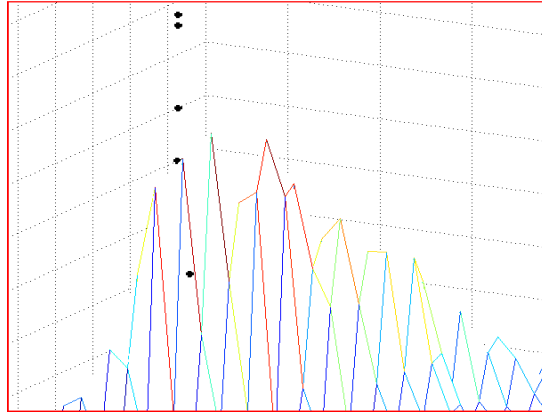
Fig 98 SQP result with the initial value of L=100nm, λ=850nm – zoomed area

The third attempt with initial value of 150nm, a length value that is larger than the expected peak value with wavelength at λ=850nm yield a performance shown in Fig 99. Dots refer to field intensities of the SQP optimizer traced during the convergence history while the scaled-up version is shown in Fig 100 predicting an overall similar performance as with an initial value of 100nm since the initial value of 150nm is still closely located from the expected optimal value range with a relatively better performance when compared with the initial design point of 100nm. The converged intensity result of the design with initial 150nm length is 8,97E+22 at L= 104nm and λ=833nm.
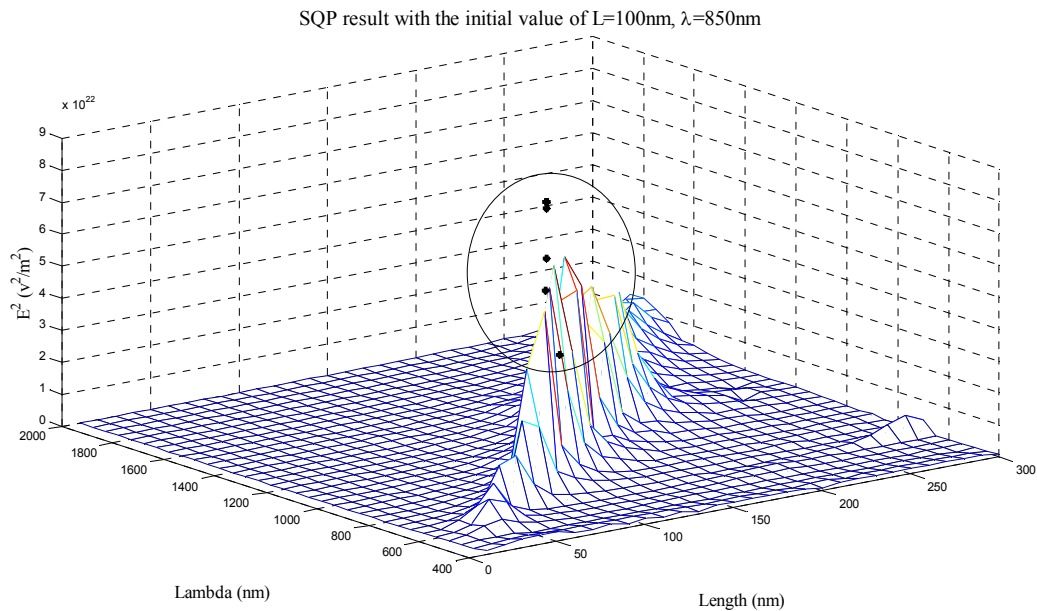

Fig 99 SQP result with the initial value of L=150nm, Lambda=850nm – entire graph

65
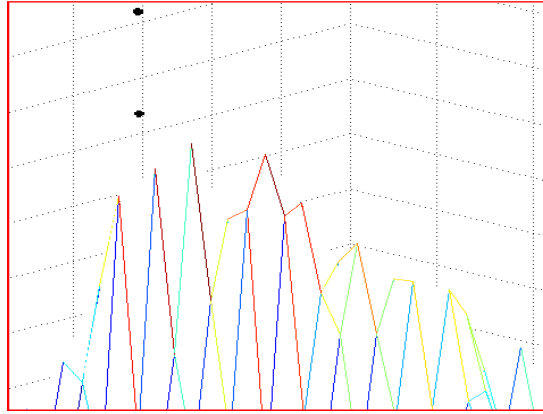
Fig 100 SQP result with the initial value of L=150nm, λ=850nm – zoomed area

To test the performance with a far located initial variable value such as 50nm, the optimizer traced a convergence history indicated with dots shown in Fig 101 where for this case the wavelength is held constant at λ=1000nm. When the scaled up version is taken into consideration (Fig 102), it can be seen that the performance is not as efficient with an optimal predicted value of 6,89E+22 but still close to the potential region despite the far located initial value and non-smooth behavior of the simulation performance.

Fig 101 SQP result with the initial value of L=50nm, Lambda=1000nm – entire graph
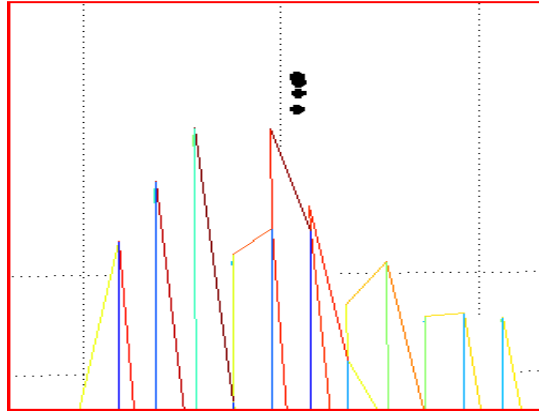
Fig 102 SQP result with the initial value of L=50nm, λ=850nm – zoomed area

Final two cases focused on various initial length values of 100nm and 150nm as earlier where the wavelength was held constant at 850nm for the case where it did not change at a values of λ=1000nm. Fig 103 refers to the performance of the SQP optimization tool for the former with an upscaled version in Fig 104 and Fig 103 refers to field intensities found from the SQP optimization tool with a scaled up version shown in Fig 106 for the latter with initial length value of 150nm, respectively. When compared with earlier runs, the peak locations were closely approached despite the non-smooth performance behavior with exact converged values depending on the discretization of the optimizer (i.e. move step) and closeness of the selected initial value variable.

SQP result with the initial value of L=100nm, λ=1000nm
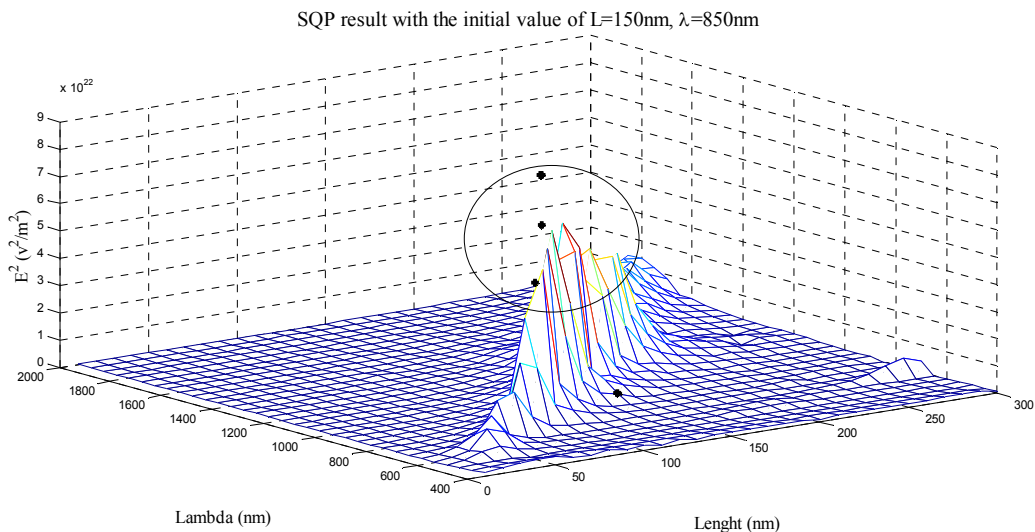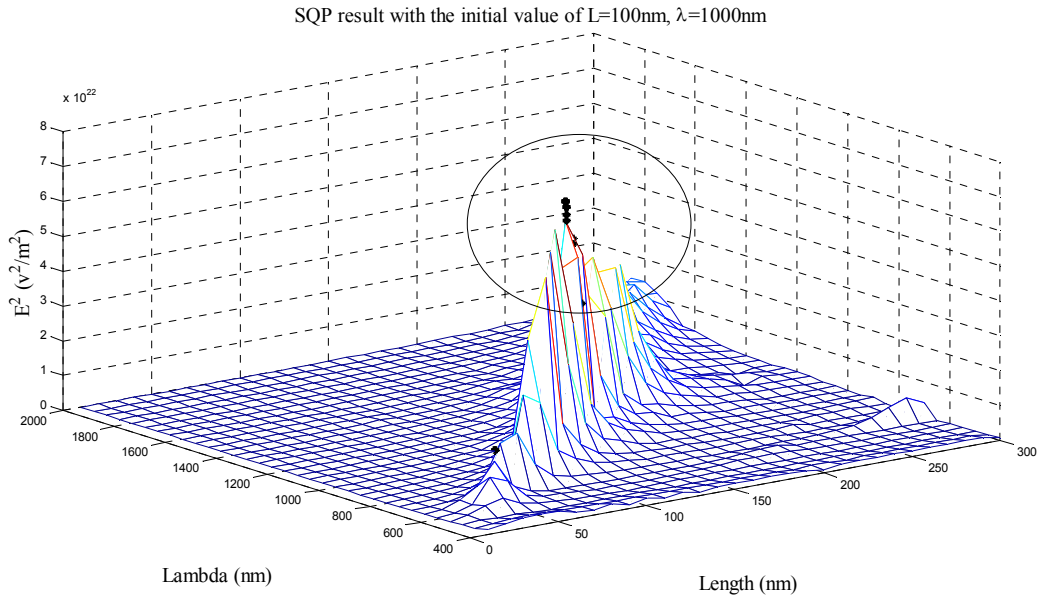

Fig 103 SQP result with the initial value of L=100nm, Lambda=1000nm – entire graph
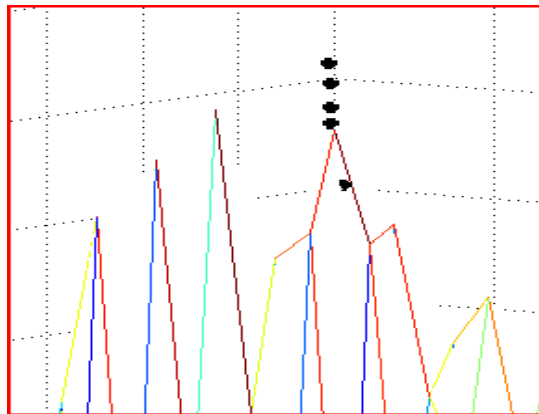
Fig 104 SQP result with the initial value of L=100nm, λ=850nm – zoomed area

SQP result with the initial value of L=150nm, λ=1000nm
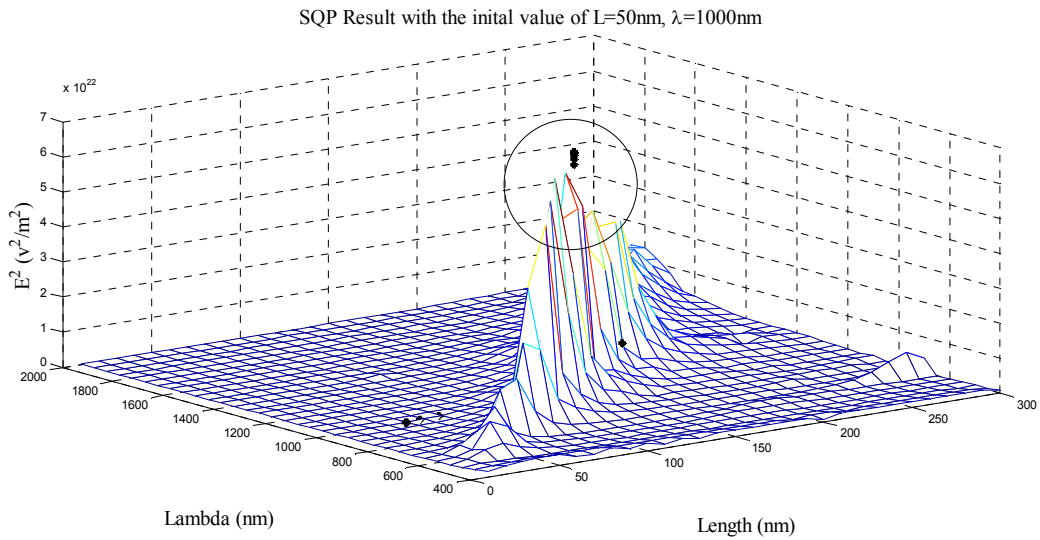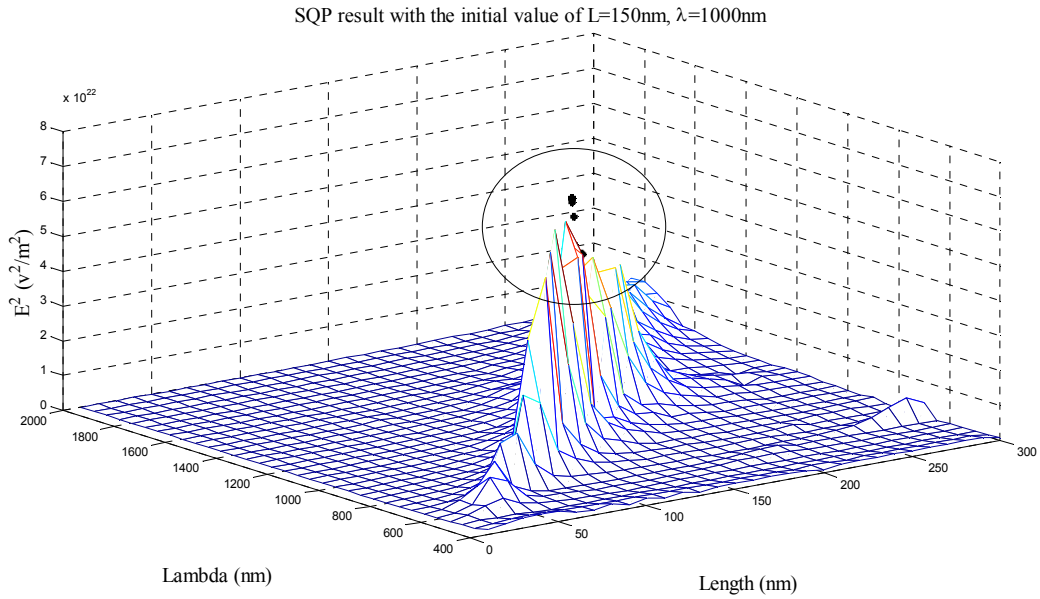

Fig 105 SQP result with the initial value of L=150nm, λ=1000nm – entire graph
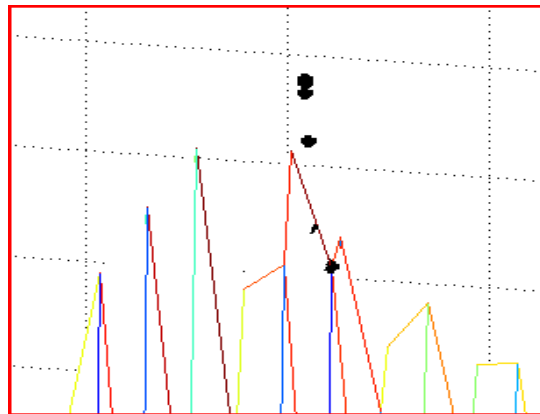
Fig 106 SQP result with the initial value of L=150nm, λ=850nm – zoomed area

3.4.1.2 Time and Accuracy Comparison According to Pass Number and Vacuum Box Size:

With the aim of analyzing the accuracy of the analysis tool and investigating its unstable/oscillatory performance possibly pointing for simulation time reduction strategies, key components affecting the accuracy and computational time are varied and results are shown inTable 5 and Table 6.

In Table 5, intensity field square is simulated for various values of pass number and the vacuum box size of the simulation model.

Pass Number	Size of Vacuum Box	Lambda (nm)	Length (nm)	Esqr (v^2/m^2)
12	1x	933.2542	129.0366	8.08E+22
12	1.5x	933.2542	129.0366	5.45E+22
12	2x	933.2542	129.0366	5.65E+22
20	1.5x	933.2542	129.0366	5.56E+22
20	2x	933.2542	129.0366	5.33E+22

Table 5 Esqr (Electric field intensity) accuracy comparison according to pass number and vacuum box size

In Table 6, intensity field square and computational time is calculated for various vacuum box sizes while keeping the pass number as 12, for which the electric field intensity value seems to attain a converged value of 5.45e22 V^2/m^2.

Pass Number	Size of Vacuum Box	Lambda (nm)	Length (nm)	Esqr (v^2/m^2)	Time
12	1x	933.2542	129.0366	8.08E+22	00:59:22
12	1.25x	933.2542	129.0366	7.70E+22	01:05:14
12	1.3x	933.2542	129.0366	7.77E+22	01:10:07
12	1.4x	933.2542	129.0366	5.46E+22	01:10:07
12	1.5x	933.2542	129.0366	5.45E+22	01:26:20

Table 6 Time and accuracy comparison according to pass number and vacuum box size

Using the information in Table 5 and Table 6, the optimal analysis model for the design optimization process is selected as the first one with pass No:12, Vacuum Box= 1x considering pratical time limitations and satisfactory relative accuracy. However, it is noted that the model settings have a direct impact on the numerical accuracy of the electric field calculations, hence the design results are only reliable given the accepted accuracy settings of the simulation model and hence final designs need to re-simulated for further accuracy improvements with higher accuracy settings at the end. Also, numerical instability issues inherent in the HFSS analysis module give rise to unexpected sharp oscillations within brute force studies as shown earlier and need to be investigated further since small changes on the order of nano-scale in dimensions is not expected to results in large changes of the field intensity.

3.4.1.3 **Heuristic Based Method Results via GA***:*

In this section, the optimizer is changed to the Genetic Algorithm.   Prior to conducting the optimization via GA, again a tuning of its option settings took place and at the end were selected to maintain diversity throughout the cycle. These GA options set to obtain results in this section are as follows: nvars (Number of variables)=2, lb (lower bounds)= [10,400], ub (upper bounds) = [300,2000], MutationFcn= @mutationadaptfeasible (mutation function randomly generates directions that are adaptive with respect to the last successful or unsuccessful generation. A step length is chosen along each direction so that linear constraints and bounds are satisfied), Display= 'iter' (displays information at each iteration of the algorithm) and the other options are left as their default vales in the Matlab's gads toolbox.

The result in Fig 107 shows the individuals within about 550 iterations of the GA search with field intensity square values found from the GA optimization tool (dots) plotted on the brute force simulation results. Again for easier comparison, a scaled-up version of the same graph near the expected maxima is plotted as shown in Fig 108.. The GA algorithm converged to a value of 6.6E+22 m^2/v^2 at 129nm length and 933nm wavelength. As evident from the overlap of the last generation individuals (dots) being condensed much closer to the expected peak range of the brute force simulations when compared with earlier SQP runs, the performance of locating a closer value (almost exact with discrepancies due to unovoidable numerical instabilities) is in favor of the GA. However, the number of generations point towards inferior timespans, hence speed-up techniques are absolutely necessary especially when more complicated design problems will be tackled in the future.
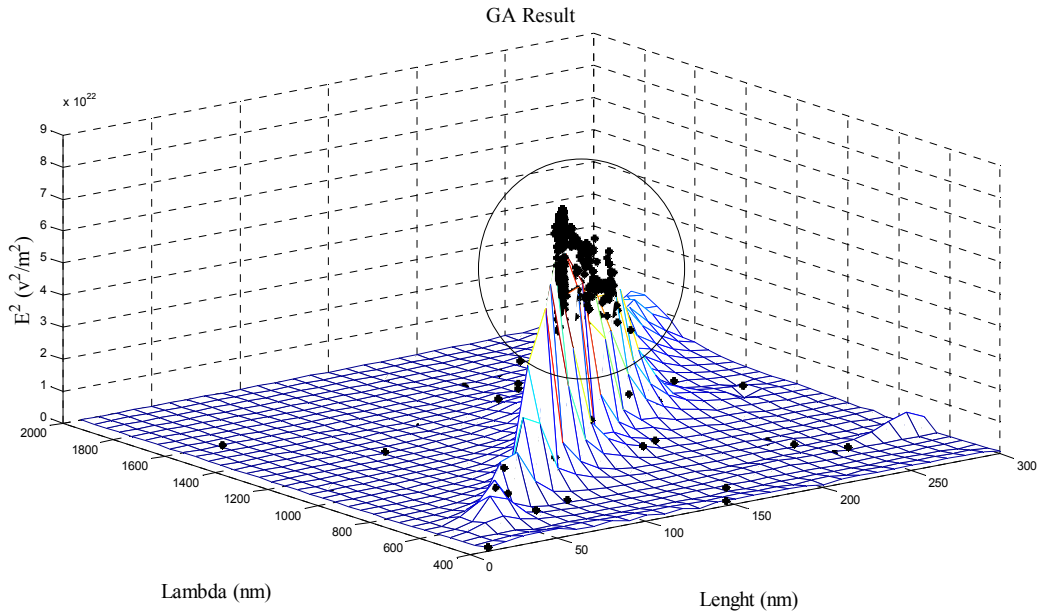
GA Result

Fig 107 GA Result – entire graph
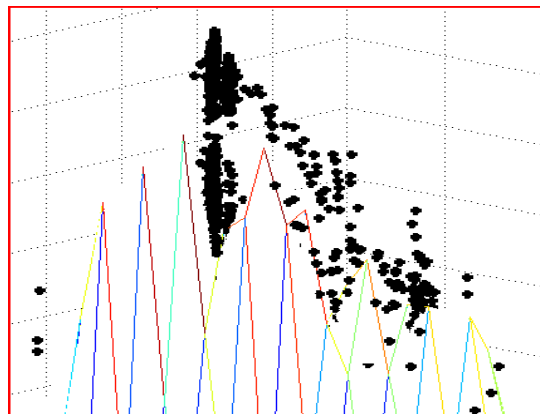
Fig 108 GA Result – zoomed area

3.5   Conclusions

In this chapter a design optimization framework was developed and applied to the design of nano-dipole antennas. Brute force simulations were carried out to obtain electric field intensity and power absorbtion dependencies on length and wavelength and compared to optimization results using SQP and GA for maximum field intensity requirements. In general there is an overall agreement even with the local optimizer for the oscillatory intensity field response for optimal lengths with brute force results at wavelengths close to bound

constraints. The differences between exact values are recognized to two main reasons: Inaccurate brute-force predictions of maximum field intensity of finite sampled wavelength and length data points and -as expected with gradient based optimization tools- SQP's dependency on the chosen initial design point in locating the optimum solution. The GA based optimization framework seems to overcome this issue in the expense of computational time. Initial results seem to be promising in providing the capability of exploring nano-structures with several design parameters. The future work includes expanding the framework to hybridize both optimization tools in combining the advantages of global and local optimization tools and to expand the framework to formal multi-objective design optimization problems.

4   CONCLUSIONS AND FUTURE WORK

4.1   Conclusions

The first part of the thesis focused on the detailed analysis of DPD process parameters to produce large substrates of monolithic spatially variable ceramics using commercial MCT powders. At the end, full densification of MCT20, MCT70 and Ni-based ferrite was covered with compatible shrinkage and cracks, warpages and undesired porosities were mostly eliminated. Optimum conditions of compression pressure, sintering time and temperature are determined with the help of dielectric constant and loss measurements, SEM images, TGA analysis and shrinkage studies. It is also shown that dielectric permittivity and permeability can be tuned by mixing existing dielectric and magnetic shades and allow for the realization of design optimization studies for variety of RF devices with enhanced performance.

The substrate layers of an earlier design UHF antenna are fabricated with the desired morphology after various trials. Despite its lengthy procedure, the main advantage of DPD over traditional assembly processes is that during dry powder pressing, the deformation is axial, so any transverse design can be preserved. Automation efforts could readily adapt DPD for conventional industrial practice, replacing the simple powder feed in an automated

compaction machine with an appropriate feed mechanism for each composition. The automation of DPD is likely to result in a versatile and effective 3D fabrication technique that will allow for the practical fabrication of exact designs in feasible time spans. It is expected to evolve as an ideal practical technique to produce multi-material novel material compositions of future antennas. Additional aspects related to the extension of the method with various magnetic and conductor inclusions to produce a complete antenna structure will allow the design and realization of these materials to provide previously unobtainable figures of merit and new capability for a wide range of operating frequencies.

The second part of the thesis focused on formal design optimization studies using a script based framework relying on the a full wave analysis simulator, HFSS and optimization tools in MATLAB relying on SQP and GA. The resulting optimization platform is applied to the design of an optical plasmonic nano-antenna. The results of the optimization framework are compared with those of the brute-force simulations. As summarized in the earlier chapters in general there is an agreement for optimized regions with SQP outperforming GA in terms of computational accuracy but the GA being more accurate overcoming numerical instability problems especially enhanced in gradient evaluations in the case of the SQP. Inaccurate brute-force predictions and non-smooth behavior of maximum field intensity of finite sampled length points is one of the performance difference reasons, with the second being of the difference of SQP's performance in locating the optimum solution depending on the chosen initial design point. In the expense of the computational time, GA based optimization framework seems to overcome this issue.

4.2 Future Work

The first part of the thesis can be expanded so that the DPD process can be effectively used for the realization of design optimization studies for variety of RF devices with enhanced performance.

- The UHF antenna can be constructed using the produced substrates with a possible void forming technique for the feed and the addition of a bottom layer made of K15.
- Additional shades of magnetic flakes can be introduced and conditions can be optimized for.

- Conductive type materials could be integrated to the DPD method itself to create radiating parts and feeds as integrated to the substrate itself.
- Automation of the DPD process.

The second part of the thesis focused on developing and initial design optimization framework that is modular and can address nano-antennas. Future work includes:

- Integration of the framework to the NBI method to investigate tradeoff between performance metrics of nano-antennas using Pareto Optimality.
- Investigation of the numerical instability of the HFSS analysis simulator and developments of possible remedies for smoothing output responses.
- Adaptation of framework to bow-tie antennas and antennas of more complicated topologies.
- Optimization of antenna with respect to Absorbed Power and a possible third performance metric such as heat dissipation.

5   APPENDIX 1

5.1   Dielectric Measurements via Agilent E4991A RF Impedance/Material Analyzer (at OSU)

Fig 109 Dielectric constant versus frequency of K70 ceramics under various sintering conditions

Fig 110 Dielectric constant versus frequency of K50 ceramics under various sintering conditions
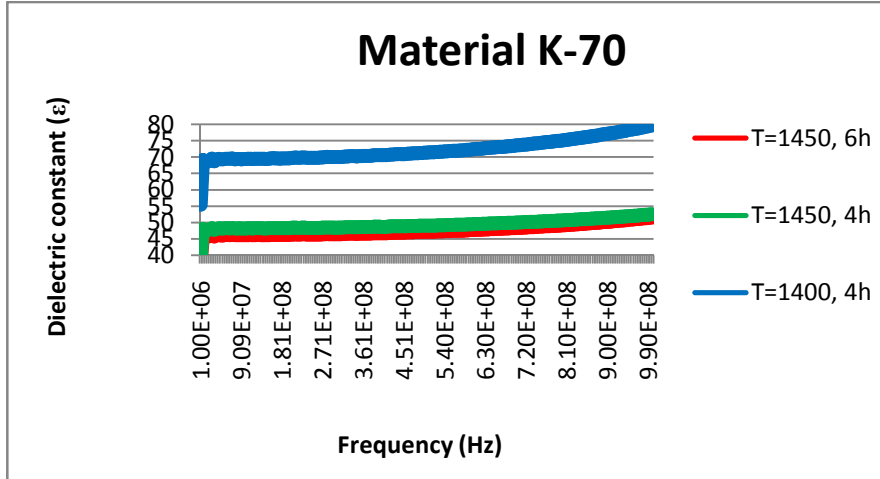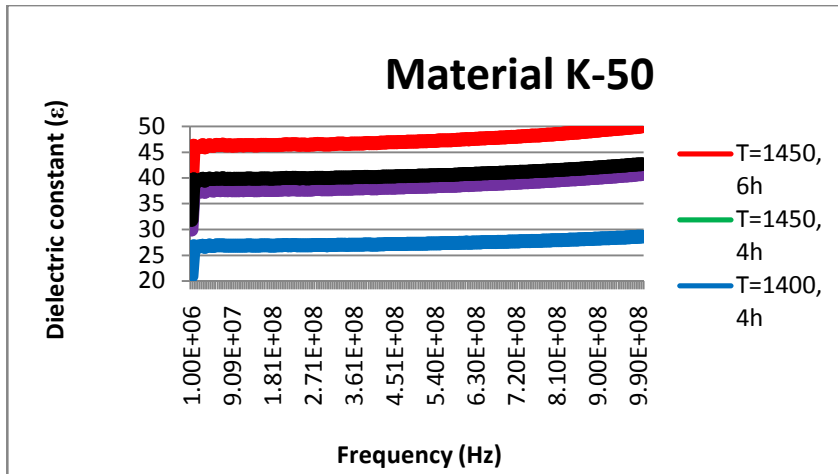
76

Fig 111 Dielectric constant versus frequency of K20 ceramics under various sintering conditions

Fig 112 Dielectric constant versus frequency of K15 ceramics under various sintering conditions

Fig 113 Dielectric constant versus frequency of K250 ceramics under various sintering conditions

Fig 114 Dielectric constant versus frequency of Magnetic material under various sintering conditions

Fig 115 Dielectric constant versus frequency of Magnetic toroid material under various sintering conditions

Fig 116 Dielectric loss versus frequency of K70 ceramics under various sintering conditions

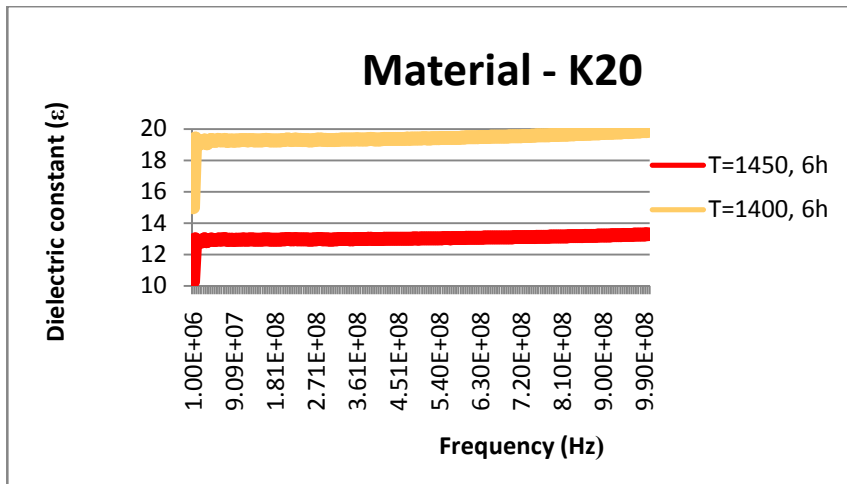Fig 117 Dielectric loss versus frequency of K50 ceramics under various sintering conditions

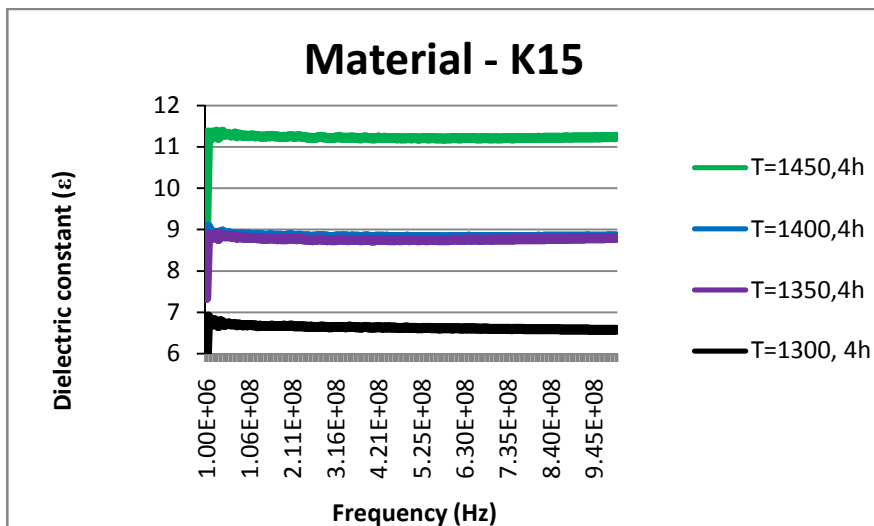Fig 118 Dielectric loss versus frequency of K20 ceramics under various sintering conditions

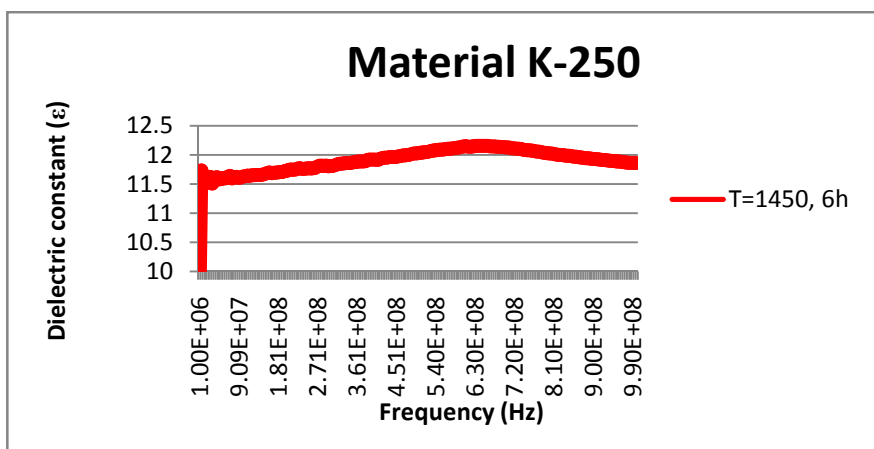Fig 119 Dielectric loss versus frequency of K15 ceramics under various sintering conditions

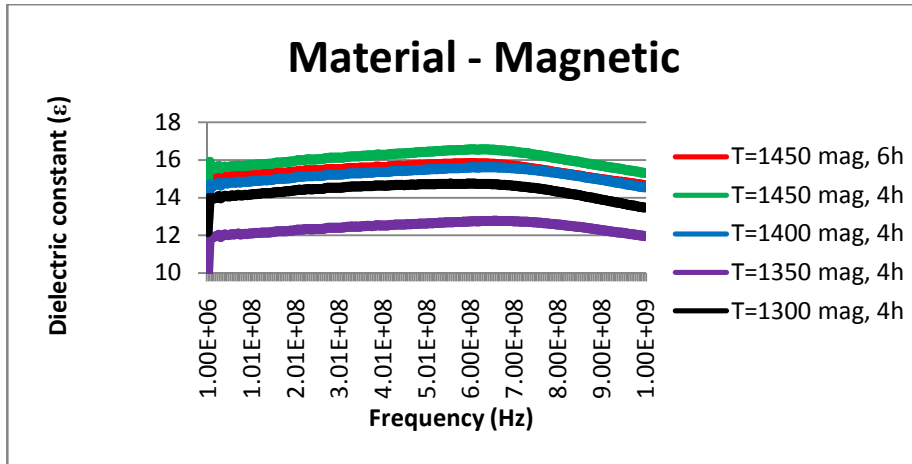Fig 120 Dielectric loss versus frequency of K250 ceramics under various sintering conditions

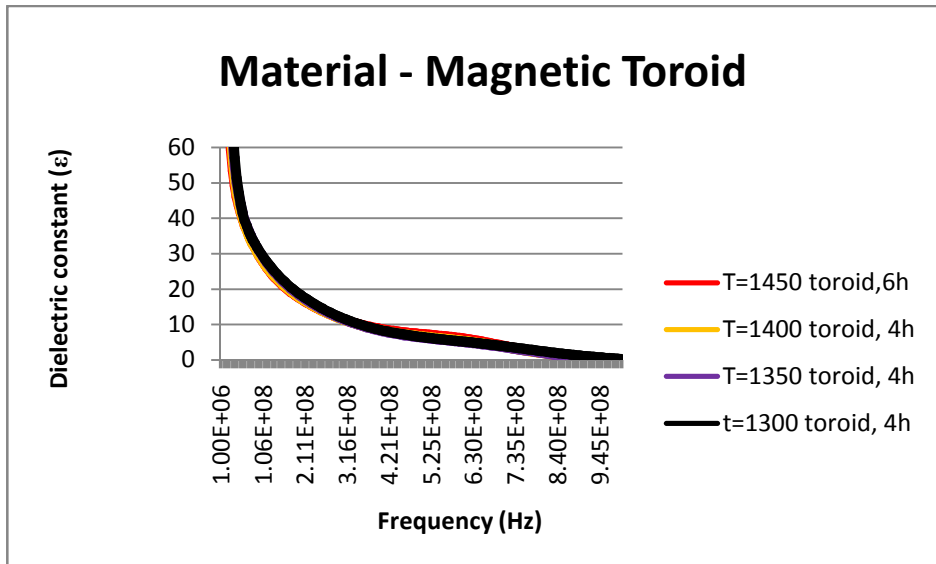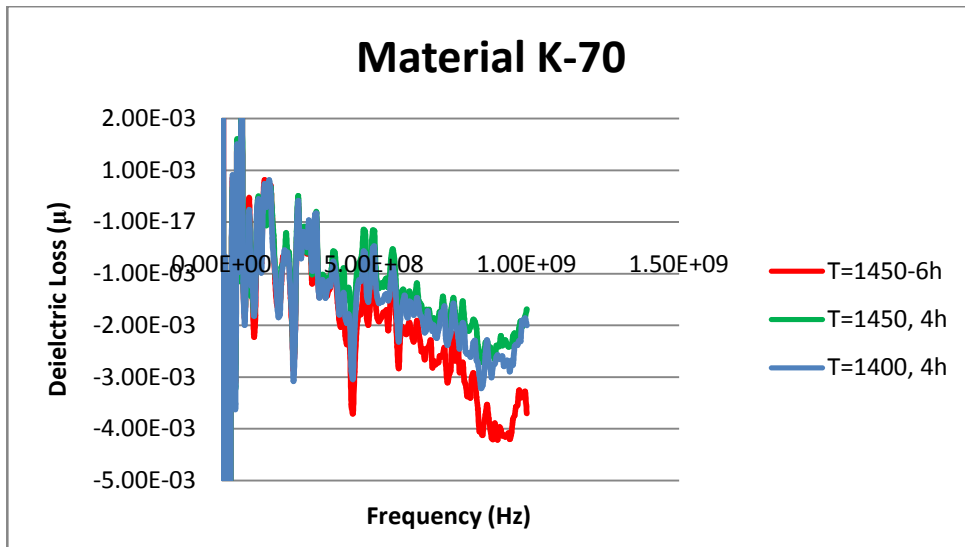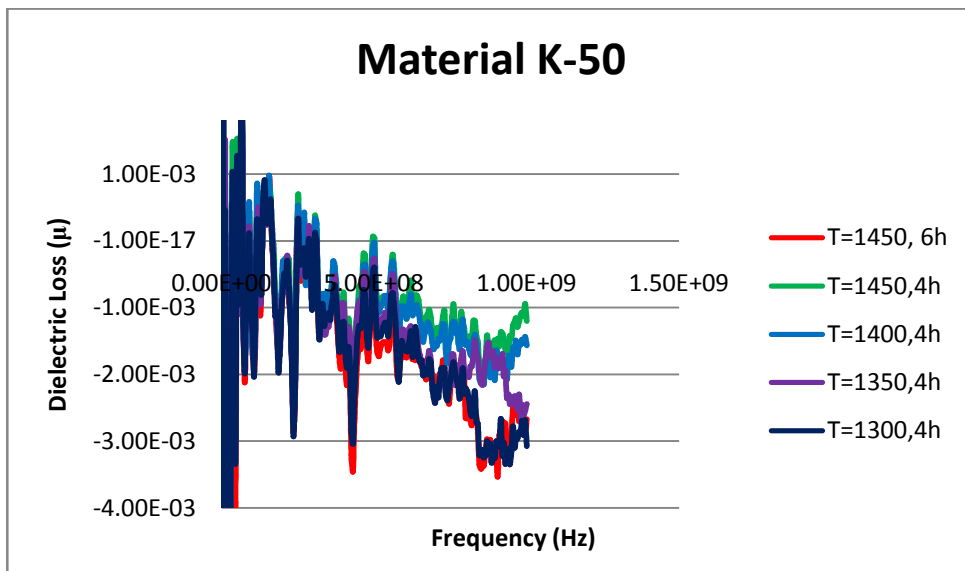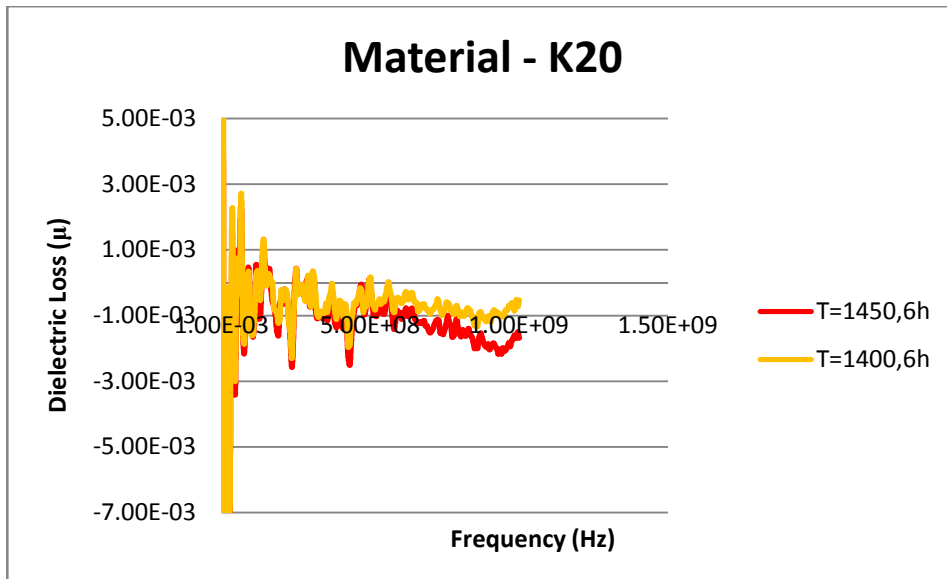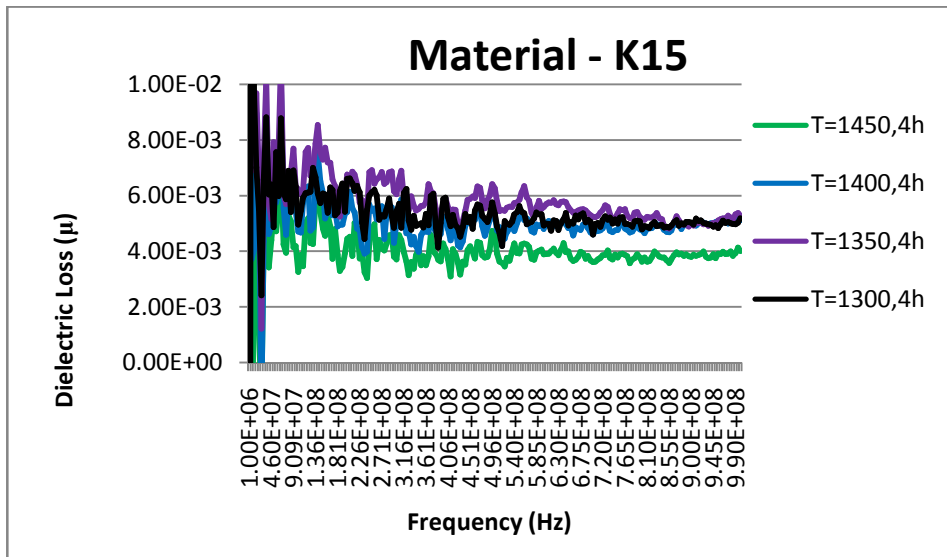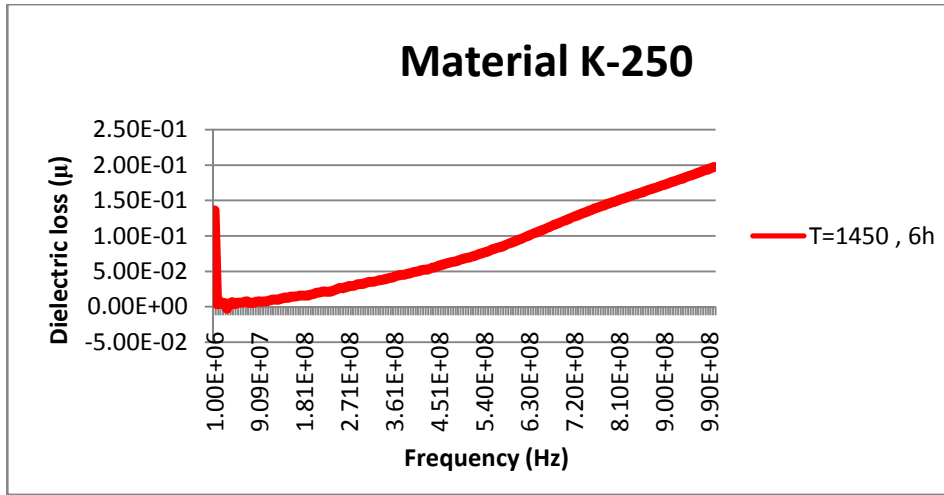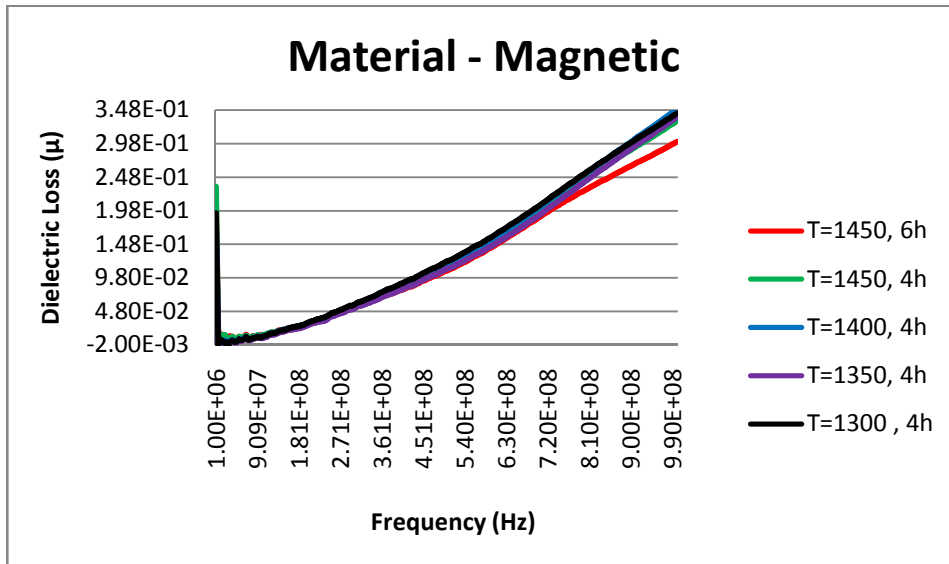Fig 121 Dielectric loss versus frequency of Magnetic materials under various sintering conditions
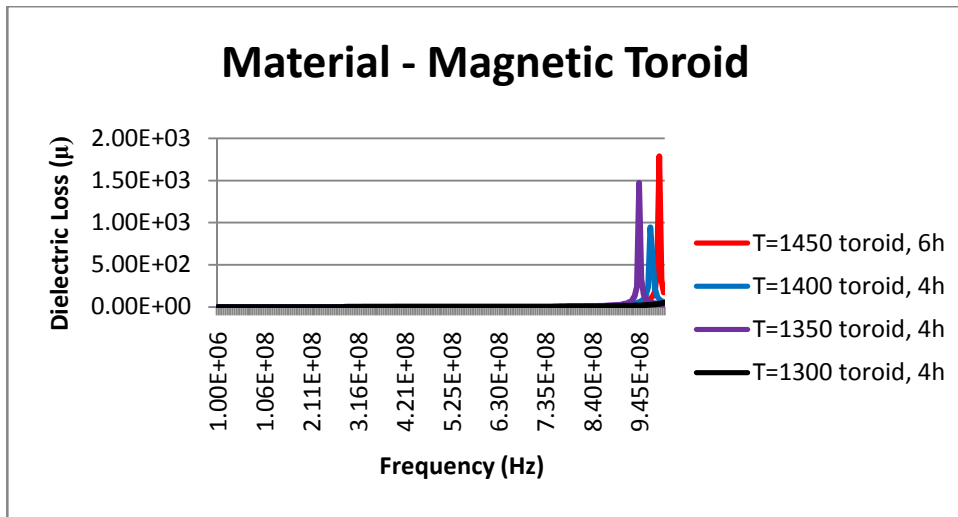
81

Fig 122 Dielectric loss versus frequency of Magnetic toroid materials under various sintering conditions

6   REFERENCES

1.   D. Psychoudakis, J.Volakis, Z. Wing, S. Pillai, and J. Halloran, *Enhancing UHF antenna functionality through dielectric inclusions and texturization.* IEEE Transactions on Antennas and Propagation, Feb. 2006. **54**: p. 317–329.

2.   G. Kiziltas, D. Psychoudakis, JL Volakis, *Topology design optimization of dielectric substrates for bandwidth improvement of a patch antenna.* IEEE Transactions on Antennas and Propagation, 2003. **51**(10): p. 2732-2743.

3.   G. Kiziltas, J.L. Volakis, and N. Kikuchi, *Design of a frequency selective structure with inhomogeneous substrates as a thermophotovoltaic filter.* IEEE Transactions on Antennas and Propagation, 2005. **53**(7): p. 2282-2289.

4.   Y.-H. Koh, J. Halloran, G. Kiziltas, D. Psychoudakis, and J. Volakis, *Thermoplastic green machining for textured dielectric substrate for broadband miniature antenna.* Journal of the American Ceramic Society, 2005. **88**(2): p. 297-302.

5.   C. Song, , Z. Xu, and J. Li, *Structure of in situ Al/Si functionally graded materials by electromagnetic separation method.* Materials & Design, 2007. **28**(3): p. 1012-1015.

6.   Z. N. Wing and J. W. Halloran, *Dry powder deposition and compaction for functionally graded ceramics.* Journal of the American Ceramic Society, 2006. **89**(11): p. 3406-3412.

7.   Z. N. Wing, J. W. Halloran, Q. Zhang, and P. J. McGinn, *Variable Dielectrics in the Calcium Magnesium Titanate System Characterized with Scanning Microwave Microscopy.* Journal of the American Ceramic Society, 2006. **89**(5): p. 1610-1614.

8.   Z. N. Wing, B. Wang, and J. W. Halloran, *Permittivity of porous titanate dielectrics.* Journal of the American Ceramic Society, 2006. **89**(12): p. 3696-3700.

9.   G. X, S. H. Wing, E. E. Hoppenjans, Z. N. Wing, G. R. Geyer, J. W. Halloran, W. J. Chappell, Tailored and anisotropic dielectric constants through porosity in ceramic components. IEEE Transactions on Microwave Theory and Techniques, 2005. **53**(11): p. 3638-3647.

10.   R. Mauczok, and V.T. Zaspalis, *Binder burnout-material-process interaction during sintering of MnZn-ferrites.* Journal of the European Ceramic Society, 2000. **20**(12): p. 2121-2127.

11.   Z.N. Wing, *Ph.D. Thesis, Fabrication and characterization of effective medium dielectrics meta-dielectrics.* 2006, The University of Michigan: Ann Arbor, MI, USA.

12.   Y.-H. Koh, A. Knapp, J. Halloran, H.W. Kim, and H.E. Kim, *Co-firing of spatially varying dielectric Ca–Mg–Silicate and Bi–Ba–Nd–Titanate composite.* Journal of the American Ceramic Society, 2005. **88**(10): p. 2690-2695.

13.   B.A Bender, and M.J. Pan, *The effect of processing on the giant dielectric properties of CaCu3Ti4O12.* Materials Science and Engineering B, 2005. **117**(3): p. 339-347.

14.   J. Fan and F.R. Sale, *The microstructures, magnetic properties and impedance analysis of Mn-Zn ferrites doped with B2O3.* Journal of the European Ceramic Society, 2000. **20**(16): p. 2743-2751.

15.   A. Verma and D. C. Dube, *Processing of nickel-zinc ferrites via the citrate precursor route for high-frequency applications.* Journal of the American Ceramic Society, 2005. **88**(3): p. 519-523.

16.   A. Hartschuh, E. J. Sa´nchez, X. S. Xie, and L. Novotny, *High-resolution near-field raman microscopy of single-walled carbon nanotubes.* Physical Review Letters, 2003. **90**(9): p. 095503.

17.   L. Novotny and B. Hecht, *Principles of Nano Optics*. 2006: Cambridge University Press.

18.   K. Şendur, O. Karabasoglu, E. A. Baran, and G. Kiziltas, *Optimization of plasmonic nano-antennas. MRS Conference Proceedings*. 2008. San Francisco, USA.

19.   L. Novotny, *Phys. Rev. Lett*. 98, 266802 (2007).

20.   W. Challener, I. Sendur, and C. Peng, *Scattered field formulation of finite difference time domain for a focused light beam in dense media with lossy materials*. Opt. Express, 2003. **11**(23): p. 3160-3170.

21.   H. Raether, *Physics of thin films*. Academic, New York, NY, 1977: p. 145-261.

22.   P. Muhlschlegel, H.-J. Eisler, O. J. F. Martin, B. Hecht, and D. W. Pohl, *Resonant Optical Antennas*. Science, 2005. **308**(5728): p. 1607-1609.

23.   F. Jackel, A.A.K., and W. E. Moerner, *Chem. Phys. Lett*, 2003. **446**: p. 339-343.

24.   I. Das and J.E. Dennis, *Normal boundary intersection: A new method for generating the pareto surface in nonlinear multicriteria optimization problems*. 1998, SIAM Journal on Optimization. **8**(3): p. 631-657.

25.   *EDO Corporation, Model DMC196-1-1*.

26.   R.A. Serway, *Physics: For scientists and engineers - Chapter 38*. 3rd Edition. 1992: Saunders College Publishing.

27.   D.M. Pozar, *Microwave engineering*. 1998: Wiley.

28.   G. Kiziltas, J.L.Volakis, Z. N. Wing, and J.W. Halloran. *Topology optimization of a compact UHF spiral array embedded in a textured dielectric*. in *AP-International Symposium and USNC/URSI National Radio Science Meeting*. 2005. Washington, D.C.

29.   L.J. Chu, *Physical limitations of omni-directional antennas*. Journal of Applied Physics, Dec. 1948. **19**: p. 1163-1175.

30.   D. Psychoudakis, S.K.C Pillai, J. W. Halloran, and J.L. Volakis, *Miniaturization of a bow-tie antenna with textured dielectric superstrates*. APS International Symposium, IEEE 2004. **vol 3**: p. 2572 - 2575

31.   *http://en.wikipedia.org/wiki/Nanophotonics*.

32.   L. Novotny, M. R. Beversluis, K.S. Youngworth, and T. G. Brown, *Longitudinal field modes probed by single molecules*. Physical Review Letters, 2001. **86**(23): p. 5251.

33.   *IEEE Transactions on Antennas and Propagation, Special Issue on Metamaterials*. Oct. 2003. **vol. 51**.

34.   G. Kiziltas, Z. Wing, J. L. Volakis, and J. Halloran. *Topology optimization of a compact UHF spiral array embedded in a textured dielectric*. in *6th World Congresses of Structural and Multidisciplinary Optimization*. 30 May - 03 June 2005. Rio de Janeiro, Brazil.

35.   B. Kieback, A. Neubrand, and H. Riedel, *Processing techniques for functionally graded materials*. Materials Science and Engineering A, 2003. **362**(1-2): p. 81-106.

36.   *Industrial Applications of FGM Solutions*. Materials Science Forum, V. 423-425 17-22, 2003.

37.   T.R. Jackson, H.L., N.M. Patrikalakis, E.M. Sachs, and M.J. Cima, *Modeling and designing functionally graded material components for fabrication with local composition control*. Materials and Design, 1999. **20**: p. 63-75.

38.   P. W. Alexander, D. Brei, W. Miao, J. W. Halloran, R. L. Gentilman, G. E. Schmidt, P. T. McGuire and J. R. Hollenbeck, *Fabrication and experimental characterization of d31 telescopic piezoelectric actuators*. Journal of Materials Science, 2001. **36**(17): p. 4231-4237.

39.   K. Takagi, J.F.L., R. Watanabe, A. Almajid, and M. Taya, *Development of piezoelectric actuators with graded porosity.* Materials Science Forum, 2003: p. 423-425, 405-410.

40.   A. Navarro, R.W.W., and J.R. Alcock, *Preparation of functionally graded PZT ceramics using tape casting.* Journal of Electroceramics, 2004: p. 13, 413–415.

41.   X. Zhu, and Z. Meng, *Operational principle, fabrication and displacement characteristics of a functionally gradient piezoelectric ceramic actuator.* Sensors and Actuators A: Physical, 1995. **48**(3): p. 169-176.

42.   X.H. Zhu, J.X., Z.Y. Meng, et al., *Micro displacement characteristics and microstructures of functionally graded piezoelectric ceramic actuator.* Materials & Design, Dec 2000. **6**: p. 561-566.

43.   X. Zhu, J.I.E. Xu, and Z. Meng, *Interdiffusion reaction in the PZT/PNN functionally gradient piezoelectric ceramic materials.* Journal of Materials Science, 1998. **33**(4): p. 1023-1030.

44.   V. Teixeira, *Numerical analysis of the influence of coating porosity and substrate elastic properties on the residual stresses in high temperature graded coatings.* Surface and Coatings Technology. **146-147**: p. 79-84.

45.   A. Portinha, V. Teixeira, J. Carneiro, J. Martins, *Characterization of thermal barrier coatings with a gradient in porosity.* Surface and Coatings Technology, 2005. **195**(2-3): p. 245-251.

46.   A. Portinha, V. Teixeira, J. Carneiro, and M.G. Beghi, *Residual stresses and elastic modulus of thermal barrier coatings graded in porosity.* Surface and Coatings Technology. **188-189**: p. 120-128.

47.   M.P. Bendsoe, *Optimal shape design as a material distribution problem.* Structural and Multidisciplinary Optimization, 1989. **1**(4): p. 193-202.

48.   S. Yang, and J.R.G. Evans, *Acoustic initiation of powder flow in capillaries.* Chemical Engineering Science, 2005. **60**(2): p. 413-421.

49.   S. Yang, and J.R.G. Evans, *A multi-component powder dispensing system for three dimensional functional gradients.* Materials Science and Engineering: A, 2004. **379**(1-2): p. 351-359.

50.   *http://www.kocaeli.abigem.org/teknopark/default.asp?page=hizli_prototipleme*.

51.   *http://www.home.agilent.com/agilent/product.jspx?pn=E4991A*.

52.   A. Sihvola, *Mixing rules with complex dielectric coefficients.* Subsurface Sensing Technologies and Applications, 2000. **1**(4): p. 393-415.

53.   *http://cp.literature.agilent.com/litweb/pdf/5980-2862EN.pdf*

54.   *Agilent 16451B - Users Manual. http://cp.literature.agilent.com/litweb/pdf/16451-90020.pdf*

55.   H.W. Kuhn and A.W. Tucker, *Nonlinear programming. Proceedings of 2nd Berkeley Symposium,* Berkeley: University of California Press 1951: p. 481-492.

56.   *Matlab Optimization Toolbox*.

57.   *HFSS Software Help Tool*

58.   *http://en.wikipedia.org/wiki/Multiobjective_optimization#cite_note-0*.